UNIVERSITY OF OKLAHOMA
GRADUATE COLLEGE

UNCOOLED HIGH-PERFORMANCE MICRO AND NANOSTRUCTURED LEAD SELENIDE-BASED MWIR PHOTODETECTORS

A DISSERTATION

SUBMITTED TO THE GRADUATE FACULTY

in partial fulfillment of the requirements for the

Degree of

DOCTOR OF PHILOSOPHY

By
MILAD RASTKAR MIRZAEI
Norman, Oklahoma
2025

Downloaded from SHAREOK. Persistent Handle URL: https://hdl.handle.net/11244/341801

UNCOOLED HIGH-PERFORMANCE MICRO AND NANOSTRUCTURED LEAD SELENIDE-BASED MWIR PHOTODETECTORS

A DISSERTATION APPROVED FOR THE
SCHOOL OF ELECTRICAL AND
COMPUTER ENGINEERING

BY THE COMMITTEE CONSISTING OF

Dr. Zhisheng Shi, Chair

Dr. Patrick McCann

Dr. Hjalti Sigmarsson

Dr. Bin Wang

Dr. Binbin Weng

© Copyright by Milad Rastkar Mirzaei 2025
All Rights Reserved.

Acknowledgments

I would like to express my deepest gratitude to my advisor, Dr. Zhisheng Shi, for his unwavering support, insightful guidance, and constant encouragement throughout my Ph.D. journey. His mentorship has been instrumental in shaping my research and academic development.

I am also grateful to the members of my dissertation committee—Dr. Patrick McCann, Dr. Hjalti Sigmarsson, Dr. Bin Wang, and Dr. Binbin Weng—for their valuable feedback and constructive suggestions that helped improve the quality of this dissertation.

I would like to thank my collaborators and co-authors, especially Dr. Zhisheng Shi, Dr. Lance McDowell, Dr, Binbin Weng, and Dr. J. Qui, for their significant contributions to the projects presented in this work. Your efforts and shared insights have enriched the research outcomes. Special thanks to my colleagues and lab mates in the Optoelectronic Lab and OU Microelectronic Cleanroom for the friendly and productive working environment.

I extend my heartfelt thanks to my loving wife, Masoum, for her endless love, patience, and unwavering support through all the ups and downs of my Ph.D. journey.

I am also deeply grateful to my father (Gholamreza), mother (Roghaieh), and brother (Mahdi) for their constant encouragement and support from the early stages of my life to this point; their love and belief in me have been a continual source of strength and motivation.

Preface

This dissertation is presented in a manuscript-based format and includes content that has been published or submitted for publication in peer-reviewed journals. Each manuscript-based chapter (3-5) is a self-contained unit with its own introduction, methodology, results, and discussion.

The dissertation begins in Chapter 1 with an overview of the background and motivation for this work, followed by a comprehensive review of the relevant literature to establish the scientific context of the research. Chapter 2 then describes the experimental methods, including material growth processes, characterization techniques, and the instrumentation used throughout the studies presented here. Chapters 3 through 5 contain the manuscript-style research chapters, each detailing a major component of the original work completed during my doctoral studies. Finally, Chapter 6 provides the overall conclusions of the dissertation and discusses potential directions for future research.

Several chapters are based on collaborative work with other researchers. I have contributed substantially to each of these projects in areas including experimental design, fabrication, data acquisition, analysis, and manuscript preparation. Authorship and contribution details are provided at each relevant chapter.

Portions of this dissertation have appeared in the following publications:

1. L. L. McDowell, J. Qiu, **M. Rastkar Mirzaei**, B. Weng, Z. Shi, "Integration of Epitaxial IV–VI Pb-Chalcogenide on Group IV Vicinal Ge Substrate to Form p–n Heterogeneous Structures", Crystal Growth & Design, 2021
2. L. L. McDowell, **M. Rastkar Mirzaei**, Z. Shi, "Integration of epitaxial n-PbSe Films on mismatched p-Ge substrates to form a pn heterogeneous structure", Infrared Technology and Applications XLVIII 12107, 121071W

3. L. L. McDowell †, **M. Rastkar Mirzaei** †, and Z. Shi, “Epitaxial CdSe/PbSe Heterojunction Growth and MWIR Photovoltaic Detector,” Materials, vol. 16, no. 5, p. 1866, Feb. 2023, doi: 10.3390/ma16051866.

4. L. L. McDowell, **M. Rastkar Mirzaei**, and Z. Shi "CdSe/PbSe high-temperature mid-infrared heterostructure photovoltaic photodetector", Proc. SPIE PC12420, Terahertz, RF, Millimeter, and Submillimeter-Wave Technology and Applications XVI, PC124200K (13 March 2023); https://doi.org/10.1117/12.2658801

5. **M. Rastkar Mirzaei**, and Z. Shi " Core-Shell Pbse/Cdse Quantum Dot Mid-Infrared Photoconductor", MIOMD - XVI (Aug, 6-10-2023).

6. **M. Rastkar Mirzaei**, and Z. Shi " Room-temperature Nano-structured PbSe/CdSe Mid-Infrared Photodetector: Annealing Effects ", Journal of Vacuum Science and Technology B (2024).

7. **M. Rastkar Mirzaei**, and Z. Shi " High-performance uncooled PbSe/CdSe nanostructured Mid-Infrared Photodetector with Tunable Cut-off Wavelength", Applied Physics Letters (2024).

Abstract

Uncooled High-performance Micro and Nanostructured Lead Selenide-Based MWIR Photodetectors

by
Milad Rastkar Mirzaei

Lead selenide (PbSe) is a highly promising semiconductor for mid-wavelength infrared (MWIR) photodetectors, offering a favorable combination of narrow bandgap energy, strong optical absorption, and compatibility with low-cost manufacturing processes. Despite challenges such as identifying suitable substrates for single-crystalline growth and mitigating defect-induced performance degradation, sensitized PbSe has emerged as a cost-effective, high-performance solution for uncooled sensing applications. This dissertation develops a comprehensive suite of PbSe-based heterostructure and nanostructured photodetectors, demonstrating significant advancements in device architecture, material quality, and photodetector performance.

As a foundational step, the integration of monocrystalline PbSe with vicinal germanium (Ge) substrates was realized, establishing a new pathway for forming high-quality heterogeneous interfaces despite the significant lattice constant and thermal expansion coefficient mismatch between PbSe and Ge. This was achieved through an in-situ surface treatment of the Ge substrate that enhanced adatom surface kinetics prior to PbSe deposition, resulting in crack-free, single-crystalline n-type PbSe films on p-type Ge (100) substrates. The resulting heterojunction exhibited strong diode-like rectifying behavior with a high rectification factor and low reverse-bias current density. X-ray diffraction (XRD) measurements revealed narrow full width at half maximum (FWHM), and strong photoluminescence (PL) confirmed the formation of high-quality PbSe (100) epitaxial films on industry-standard vicinal Ge substrates. This integration not only demonstrated

robust epitaxial alignment but also opened possibilities for dual-band detector architectures and other PbSe-based heterojunction devices.

Building on this foundation, a novel epitaxial CdSe-on-PbSe type-II heterojunction photovoltaic detector was demonstrated via molecular beam epitaxy (MBE). For the first time, high-quality, single-phase cubic CdSe was epitaxially grown on p-type single-crystalline PbSe films, as confirmed by in-situ reflection high-energy electron diffraction (RHEED). The resulting p–n junction exhibited rectifying behavior with a rectification factor exceeding 50 at room temperature. Under zero-bias photovoltaic operation, a 30 μm × 30 μm pixel achieved a responsivity of 0.06 A/W and a specific detectivity (D*) of 6.5×10^8 Jones at room temperature. Device performance improved significantly with thermoelectric cooling, reaching a responsivity of 0.441 A/W and a D* of 4.4×10^9 Jones at 230 K, underscoring the effectiveness of epitaxial interface engineering in enhancing carrier transport and suppressing recombination losses in PbSe-based MWIR detectors.

The research further advanced toward scalable, low-cost device architectures through the development of nanocrystalline PbSe/CdSe heterostructure photoconductors, fabricated via vapor phase deposition (VPD) on commercially available SiO_2/Si substrates. Optimization of post-deposition oxygen annealing improved film quality and defect passivation, resulting in a room-temperature D* of 8.57×10^8 Jones and a peak detectivity of 2.49×10^9 Jones, with an interband cutoff wavelength of 4 μm. Crucially, this approach demonstrated a clear pathway toward low-cost, large-area MWIR detection systems while maintaining compatibility with silicon-based readout integrated circuits (ROICs) for monolithic integration.

Further improvements were achieved by transitioning to PbSe/CdSe nanostructured photoconductors with small pixel dimensions, building directly upon insights gained from the

larger-area heterostructure devices. Aggressive pixel scaling and precise control of the annealing process enabled the formation of highly interconnected nanostructures that facilitated efficient photogenerated carrier transport and further defect suppression. The reduction in pixel size not only enhanced device performance but also revealed critical insights into the underlying gain mechanisms and the role of traps, which had been obscured in earlier large-area devices. These small-pixel devices, defined with active areas of $17.5 \times 20\ \mu m^2$ via reactive ion etching, exhibited tunable absorption edges at 3.75 μm and 4.0 μm, with room-temperature specific detectivities of 2.17×10^{10} Jones and 1.61×10^{10} Jones, respectively. External quantum efficiencies exceeding 100% confirmed strong photoconductive gain. Noise analysis indicated 1/f noise as the dominant mechanism, with behavior consistent with Hooge's empirical relation for homogeneous semiconductors, validating the high electronic quality achieved through process optimization.

Collectively, the advancements presented in this dissertation chart a progressive trajectory in PbSe-based MWIR photodetector development — from epitaxial, high-performance heterojunction diodes to scalable heterostructure photoconductors, and finally to optimized nanostructured small-pixel devices with record performance at room temperature. Through deliberate control of material growth, interface engineering, and device scaling, this work significantly advances the state of PbSe-based infrared detection. These developments establish a robust framework for future PbSe MWIR sensing technologies, offering a pathway toward compact, low-cost, high-performance detectors suitable for a wide range of commercial, industrial, and defense applications.

Table of Contents

CHAPTER 1 INTRODUCTION AND LITERATURE REVIEW 1

I. MWIR SPECTRUM AND ITS IMPORTANCE 1

II. PHOTON DETECTOR STRUCTURES 3

III. PHOTODETECTORS FIGURE OF MERITS 5

Dark Current 5

Photocurrent 5

On–off ratio 6

Response Time 6

Responsivity 7

Noise 7

Shot Noise 7

Johnson or Thermal Noise 7

Generation-Recombination Noise 8

1/f or Flicker Noise 8

Noise Equivalent Power, Detectivity, and NEDT 8

IV. BULK MWIR PHOTODETECTORS 9

Introduction to MWIR Photodetector Material systems 9

MCT Photodetectors 10

Foundational Properties of the HgCdTe Alloy 10

The Evolution to High Operating Temperature (HOT) MCT 11

State-of-the-Art Performance and Commercial Products 12

Type-II Superlattice Structure Photodetectors 14

The T2SL Paradigm: Bandgap Engineering for Superior Performance 14
Architectural Innovations Enabling HOT and RT Operation 16
Research Frontiers and State-of-the-Art Performance 18
Lead-salt Materials 20
Lead-salt Materials History 21
PbSe Anomalous Auger Coefficient and HOT Operation potential 21
Current Status of Lead-Salt Photodetectors 32
Lead Salt Market Position and Application 34
Core Comparative Performance Table 35
V. QUANTUM DOT MWIR PHOTODETECTORS 37
Quantum Effects and their Unique Properties 38
Engineering the Electronic Bandgap and Optical Properties 40
Density of States as a function of dimensionality 41
Electron Dispersion Relations (E-k Diagrams) 43
Carrier Relaxation Dynamics and the Phonon Bottleneck 45
Colloidal Quantum Dot Photodetectors 48
Photoconductive HgTe CQD-based devices 49
Photovoltaic HgTe CQD-based devices 50
Ag_2Se CQD-based devices 51
Lead-chalcogenide interband QDs 53
CHAPTER 2 EXPERIMENTAL METHODS 55
I. INTRODUCTION 55
II. MOLECULAR BEAM EPITAXY 56
Introduction to MBE System 56

Molecular Flux 57
Ultra-High Vacuum Pumps 60
Reflection High Energy Electron Diffraction (RHEED) 61
III. MICROSCOPY 62
Introduction to Microscopy 62
Scanning Electron Microscopy 63
Atomic Force Microscopy 65
IV. X-RAY DIFFRACTION 66
V. PHOTOLUMINESCENCE SPECTROSCOPY 67
VI. DEVICE FABRICATION 68
Introduction to Photolithography 68
Mask Design and Photoresist 69
Reactive Ion Etching 72
Metallization via thermal evaporation 73
VII. ELECTRICAL MEASUREMENT 74
VIII. RADIOMETRIC MEASUREMENT 75
CHAPTER 3 EPITAXIAL PBSE/GE AND CDSE/PBSE HETEROJUNCTION GROWTH AND MWIR PHOTOVOLTAIC DETECTOR 77
I. INTRODUCTION 77
N-PBSE/P-GE HETEROSTRUCTURE 78
II. EXPERIMENTAL METHODS N-PBSE/P-GE HETEROSTRUCTURE 84
III. RESULTS AND DISCUSSIONS - N-PBSE/P-GE HETEROSTRUCTURE 85
Crystallography In-Situ RHEED Analysis 85

Microscopy 87
Photoluminescence and X-Ray Diffraction 89
Current-Voltage Statistics 92
IV. CONCLUSION ON N-PBSE/P-GE HETEROSTRUCTURE 93
N-CDSE/P-PBSE HETEROSTRUCTURE 94
V. EXPERIMENTAL METHODS N-CDSE/P-PBSE HETEROSTRUCTURE 95
Epitaxial Heterojunction Growth 95
Device Fabrication 96
VI. RESULTS AND DISCUSSION N-CDSE/P-PBSE HETEROSTRUCTURE 97
Crystallography and Surface Morphology of Epitaxial CdSe films on PbSe 97
Current-Voltage and Radiometric Measurements 100
CHAPTER 4 ROOM-TEMPERATURE NANO-STRUCTURED PBSE/CDSE MID-INFRARED PHOTODETECTOR: ANNEALING EFFECTS 104
I. INTRODUCTION 104
II. EXPERIMENTAL DETAILS 107
Material and Device Structure 107
Material and Device Structure 108
III. EXPERIMENTAL DETAILS 109
Band structure and carrier transport mechanism 109
Surface morphology and absorption spectrum 110
Device Optimization Through Annealing Conditions 113
Device Radiometric Characteristics 116
IV. SUMMARY AND CONCLUSION 118

CHAPTER 5 HIGH-PERFORMANCE UNCOOLED PBSE/CDSE NANOSTRUCTURED MID-INFRARED PHOTODETECTOR WITH TUNABLE CUT-OFF WAVELENGTH 120

I. INTRODUCTION 120

II. EXPERIMENTAL DETAILS 122

XRD Analysis 123

SEM Analysis 125

Absorption, Photoluminescence, and Tauc Plot 126

Pixel Fabrication 128

III. RESULTS AND DISCUSSION 129

Electrical and Radiometric Measurement and Discussion 129

IV. SUMMARY AND CONCLUSION 137

CHAPTER 6 CONCLUSION, SUMMARY, AND FUTURE DIRECTIONS 139

I. SUMMARY AND CONCLUSION 139

II. FUTURE DIRECTIONS: 141

List of Tables

Table 1-1. Fundamental Properties of Lead Salt Detector Materials..... 21

Table 1-2 Typical Auger lifetime at room temperature for different doping concentrations. 30

Table 1-3 Comparative Performance of High-Temperature Infrared Detectors..... 36

Table 3-1 List of relevant substrate electrical and optical properties compared with PbSe. 81

Table 3-2 Comparison of measured and reported XRD FWHM values for PbSe films on foreign substrates. 90

Table 3-3 Measured and calculated values of interest. 93

Table 3-4 Material Properties of PbSe and CdSe 95

Table 5-1. As-grown and annealed Scherrer equation parameters and crystallite size 124

Table 5-2 The Hall measurement for annealed sample #1 and #2..... 132

List of Figures

Figure 1-1 Transmission of the atmosphere for a 6000 ft horizontal path at sea level [2]. 3

Figure 1-2 Schematic for a) photoconductor, and b) photovoltaic photodetectors. Reprinted from [16]. 4

Figure 1-3 Response time of photodetector. Reprinted from Ref. [21] 6

Figure 1-4 (a) Heterostructure band alignment types (b) The band alignment of the 6.1 Å family of semiconductors. Reprinted from Ref. [34]. 15

Figure 1-5 Schematic of the plasmonic IR quantum-engineered ultra-thin epitaxial detector. Reprinted from Ref. [40]..... 17

Figure 1-6. Schematic of GMR LWIR detector (left) and its upside-down epitaxial structure after GaSb substate removal (right). Reprinted from Ref. [41]. 18

Figure 1-7 Conceptual Band Structure Comparison for auger recombination for (a) GaAs and (b) PbSe. Figures reprinted from Ref. [65], [68]. 25

Figure 1-8 Schematic diagram of (a) direct and (b) indirect electron-electron-hole Auger recombination processes. (a) In the direct case, an electron in the conduction band (1) recombines with a hole in the valence band (3) while the excess energy and momentum is transferred to a second electron (2) that gets excited to a higher conduction-band state (4). (b) The indirect process is assisted by a carrier-scattering mechanism, such as electron-phonon coupling, which provides additional momentum and enables Auger transitions to a wider range of final conduction-band states throughout the first Brillouin zone. Reprinted from [69]..... 26

Figure 1-9 Calculated Auger coefficients as a function of carrier density at 300 K. (b) Calculated Auger coefficients as a function of temperature at a fixed carrier density of 10^{17} cm^{-3} [65]. 29

Figure 1-10 Auger Coefficient for different material systems. Reprinted from Ref. [72]..... 31

Figure 1-11 D* Comparison between best reported room-temperature MWIR photodetectors. Data gathered from [120], [121], [122], [123]. 37
Figure 1-12. The steady-state absorption spectrum reveals the 1st exciton 1S(h)→1S(e) and the 2nd exciton 2S(h)→1S(e) transitions within CdTe quantum dots. The inset energy band diagram illustrates these absorption transitions between the quantum-confined electron (e) and hole (h) energy states. Potential energy wells in the conduction band (CB) and valence band (VB) are represented by the black lines. For clarity, the energy levels are not depicted to scale, and higher energy levels have been excluded. Reprinted from Ref.[128]. 40
Figure 1-13 Density of States in different material structures. Reprinted from Ref. [129]. 42
Figure 1-14 Electron Dispersion (E-k) for a (a) Bulk (3D) Semiconductor. A standard E-k diagram for a direct-gap bulk semiconductor. The vertical axis is Energy (E) and the horizontal axis is momentum (k). It shows a continuous parabolic conduction band and a continuous parabolic valence band, both centered at k=0 (the Γ point). Reprinted from Ref. [130] (b) Electron Dispersion (E-k) for a Quantum Well (2D). The energy axis shows discrete levels. From each of these levels, a 2D parabolic sub-band extends, representing free motion in the unconfined plane. The overall structure looks like a series of stacked parabolas. Reprinted from Ref. [131](c) Electron Dispersion (E-k) for a Quantum Wire (1D). The dispersion relation for a quantum wire consists of a series of 1D parabolic sub-bands, where energy is continuous only for momentum along the axis of the wire. (d) Electron Dispersion (E-k) for a Quantum Dot (0D). The diagram shows a series of discrete, horizontal lines. The energy levels do not change with k, indicating they are localized states with no dispersion. 44
Figure 1-15 Phonon-assisted hot carrier relaxation in a) Bulk semiconductor. The continuous parabolic bands make the electron relaxation with acoustic and optical phonons very easy and

accessible. b) QD the discrete energy bands reduce probability of relaxation of electron or hole via acoustic phonons and make it difficult via optical phonon if the energy difference between sub bands are larger than the LO phonon energy. 48
Figure 2-1. Custom two chamber MBE for IV-VI deposition at OU. 57
Figure 2-2 A schematic diagram of MBE with 4 effusion cells. Reprinted from [163]. 59
Figure 2-3. RHEED Image Formation. Reprinted from [164]..... 62
Figure 2-4 Schematic of scanning electron microscopy. Reprinted from [165]. 64
Figure 2-5 AFM Operation Modes: a) c-mode AFM, b) nc-mode AFM, and c) inter-atomic force regimes respective to sample-cantilever separation distance [166]. 66
Figure 2-6. Fabrication Steps for Photoconductor Device..... 70
Figure 2-7. Mask Aligner Used to Expose the Pattern 71
Figure 2-8. Normarski interference-contrast microscope 72
Figure 2-9 Trion Technology MiniLock II reactor 73
Figure 2-10 Kurt J. Lesker Nano 36 thermal evaporator..... 74
Figure 3-1 Conduction and valence band edge alignment for PbSe and other relevant material systems. 82
Figure 3-2 Schematic drawing of: (a) n-PbSe/p-Ge band alignment and (b)carrier transport in n-PbSe/p-Ge heterojunction structure. 84
Figure 3-3 RHEED images of the: (a) cleaned vicinal germanium substrate with reconstruction, (b) substrate surface after Se treatment, (c) film surface during the first monolayers of PbSe growth (d) and the final 1μm thick PbSe film surface. 86

Figure 3-4 SEM image of PbSe on Ge: Surface image indicates a meandering growth mode of epitaxial PbSe films with no observable cracks over a large area, with the in-set cross-sectional image corroborating the RHEED observations of a bulk single crystalline PbSe film. 87
Figure 3-5 AFM image of step-meandering growth observed in PbSe films: (a) 2μm x 2μm NCM surface profile scan, (b) 1μm x 1μm NCM surface profile scan, (c) 3D surface view, and (d) height profile measurement..... 88
Figure 3-6 XRD pattern for the n-PbSe surface deposited on vicinal germanium substrate: (a) wide-angle scan and (b) rocking curve. 90
Figure 3-7 Room-Temperature CW PL spectra of PbSe films deposited on Ge and BaF2..... 91
Figure 3-8 Room Temperature J-V statistics. 93
Figure 3-9 (a) Configuration schematic of the n-CdSe/p-PbSe heterojunction mid-IR photodiode with backside illumination 1.2μm PbSe deposited on 2mm BaF2 substrate. Then 200nm CdSe film deposited on top. 300 nm thick gold was deposited on top of CdSe pixel and PbSe to create the contacts. (b) suggested energy band diagram of the n-CdSe/p-PbSe heterostructure (In the figure, E vac, EC, EF, EV, EEA, VBI, EG, ΔEV, δ stands for vacuum energy, conduction band energy, Fermi energy, valence band energy, electron affinity, built-in potential, energy band gap, valence band offset, and energy difference between Fermi energy and conduction band, or Fermi energy between valence band, respectively)..... 97
Figure 3-10 . In-Situ RHEED measurements of the characteristic [110] orientation for (a) 1μm thick PbSe film on BaF2, (b) 3ML nucleation of CdSe on PbSe, (c) 5nm of CdSe, and final 200nm bulk CdSe thin film. The nucleation on growth of CdSe suggest that the CdSe followed the PbSe crystal structure and orientation. 98

Figure 3-11. XRD measurement of the epitaxial n-CdSe/p-PbSe heterostructure on BaF2 (111) substrate. The inset shows a simulated overlapping peak of PbSe and CdSe..... 99
Figure 3-12. (a) Room-temperature J-V and (b) I-V characteristic of the epitaxial n-CdSe/p-PbSe heterojunction structure shows a strong room temperature p-n junction behavior..... 100
Figure 3-13. Temperature-dependent peak Responsivity and D* measurements from 300K down to 230K under zero bias photovoltaic mode. It shows almost an order of magnitude of higher signal when the device is cooled down to 230K. 102
Figure 4-1. (a) Schematic structure of the PbSe/CdSe NC photodetector (it should be noted that nanostructures are depicted in spherical shape only for simplicity of presentation). (b) band diagram of the PbSe/CdSe type-II heterostructure. 108
Figure 4-2. Cross-sectional SEM of as grown (a) and annealed (b) sample. (c) Tauc plot for annealed sample. The inset shows the absorption spectrum of the sample. 112
Figure 4-3. (a) Signal and noise, (b) resistivity, (c) D* and peak D* intensity of four different samples annealed at 425°C to 450°C. 116
Figure 4-4. (a) Bias-dependent signal and noise for sample #2. (b) 1/f noise spectrum. (c) Specific detectivity D* and peak D* VS. bias for sample #2. 118
Figure 5-1 FE-SEM and XRD images of as-grown and annealed sample #2: (a) Cross-sectional FE-SEM of as-grown sample #2 displaying a smooth film surface. (b) Cross-sectional FE-SEM of oxygen-annealed sample #2. (c) XRD patterns for both as-grown and annealed samples, with the dominant PbSe growth orientation observed along {100}. 125
Figure 5-2 EDS images of as-grown and annealed. (a) (b) EDS image of the as-grown sample #2 showing peaks of lead, selenium, and cadmium. (b) EDS image of the annealed sample #2

displaying oxygen peaks. SEM image and EDS region of (c)as-grown film (Spectrum 7) and (d) annealed film (Spectrum 21). 126

Figure 5-3 (a) Tauc plot for annealed PbSe/CdSe NC films revealing band edge absorption of 3.7μm and 4μm, respectively. (b), (c) Absorbance and photoluminescence of the annealed PbSe/CdSe NCs showing a photoluminescent peak of 3.35μm and 3.56μm for samples #1 and #2, respectively. (d) SEM topography of 17.5μm x 20μm pixel. 128

Figure 5-4 Schematic depicting the evolution and photoconduction mechanism of the material system: (a) As-grown PbSe/CdSe Core/Shell structure. (b) CdSe shell reorganization facilitating connections between PbSe cores and some oxide formation at boundaries. (c) Optimized structure with threaded PbSe cores enabling hole transportation, recombination, and injection of new holes while trapping minority electrons. (d) Over-annealed structure causing carrier blocking. Note: NC shapes may not be spherical. 132

Figure 5-5. Radiometric and noise measurement of the device. (a) The dark current-voltage characteristics of both samples. (b) The signal and noise current of the devices under different bias voltages. (c) Responsivity and EQE, (d) specific detectivity, and peak specific detectivity of devices vs. different bias voltages. 134

Figure 5-6 Spectral noise current (a), noise spectral density and analysis (b) of sample #2. 136

Figure 5-7 The D* and Peak D* versus modulation frequencies measured at 0.4V bias. 137

Chapter 1 Introduction and literature Review

I. MWIR spectrum and its importance

Human vision is among the most advanced senses, yet nature restricts it to a narrow range within the continuous electromagnetic radiation spectrum. The aim of the research field focused on infrared detection is to extend human vision beyond its inherent limitations [1]. The infrared spectrum encompasses all electromagnetic radiation with wavelengths longer than those in the visible spectrum but shorter than millimeter waves [2]. Detecting and sensing infrared (IR) radiation offers numerous advantages for various reasons. To begin with, IR radiation detection is highly advantageous due to the inherent emissions from objects in the IR spectrum, obviating the need for supplementary illumination. This principle is referred to as 'passive detection' and is especially valuable in applications like night vision or extreme conditions where ambient light sources are absent [1]. Secondly, IR radiation, particularly within the mid-wavelength IR (MWIR) range (3–5 μm), possesses the ability to travel through the atmosphere with minimal losses, owing to its significant transparency. This quality renders IR radiation suitable for diverse applications such as free space communications and astronomy. In military contexts, IR detection finds critical utility in enhancing soldier vision and tracking missiles [2], [3]. Thirdly, beyond its atmospheric transmission characteristics, IR radiation can traverse various media without substantial intensity reduction in certain atmospheric windows (Figure 1-1a). This attribute enables the use of non-contact, non-destructive inspection methods, widely applied in industries and routine activities [4], [5]. Fourthly, IR radiation, being emitted directly from thermal sources, carries intrinsic information about the source itself. For instance, the temperature of an object can be deduced from the received IR radiation intensity, facilitating non-contact and high-sensitivity temperature measurements. Additionally, the wavelength spectrum of detected IR radiation can provide

extensive information about the source or the absorbing medium. As many materials, particularly gases and organic compounds, exhibit resonant frequencies in the IR spectrum related to their bonding energies, detecting these resonances, known as IR spectroscopy, serves as a potent tool for analyzing chemical bonds in molecules and gas sensing (can be seen in Figure 1-1b). Therefore, the MWIR spectroscopy finds its application in medical diagnosis ranging from cancer detection to asthma [6], [7], [8], [9]. Furthermore, MWIR has a broad application in environmental sensing and planet discovery. The MWIR range presents exceptional diagnostic capabilities for assessing atmospheric composition because several crucial molecules necessary for investigating planetary conditions exhibit pronounced absorption bands within the MWIR spectrum. These absorption bands in the MWIR encompass key molecules such as ozone (O_3) and methane (CH_4). Additionally, nitrous oxide (N_2O), which serves as another potential biosignature within Earth's atmosphere, displays significant absorption bands in the MWIR, but, unlike methane, lacks comparably strong absorption bands in the optical or near-infrared (NIR) wavelengths [10]. Due to these distinctive properties, IR detection has consistently garnered significant interest in research endeavors.

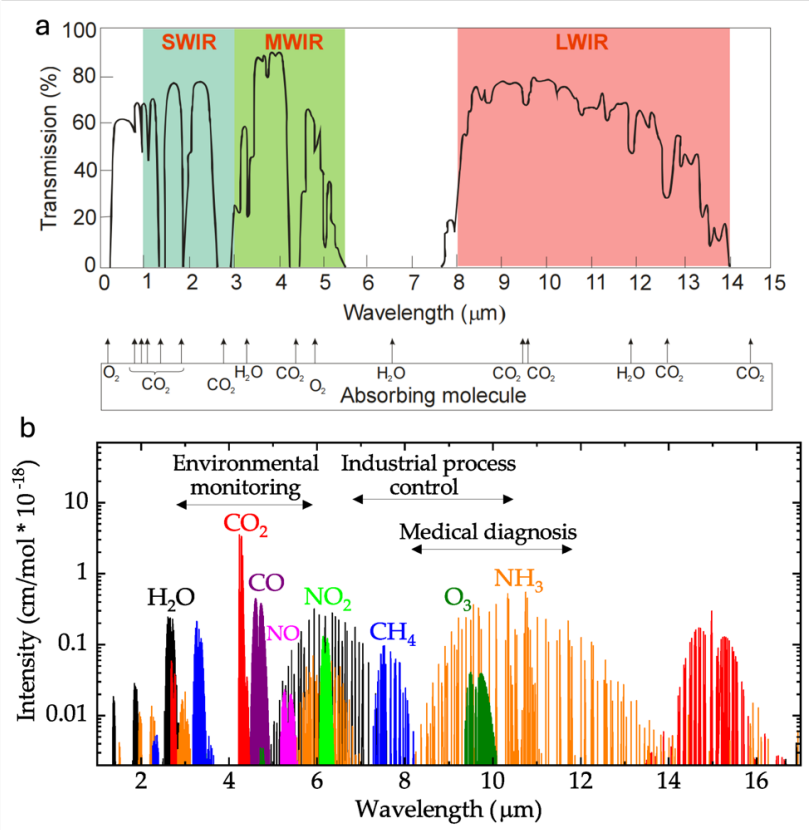


Figure 1-1 a) Transmission of the atmosphere for a 6000 ft horizontal path at sea level [2]. b) Characteristic gas absorption in infrared region. Reprinted from [11].

II. Photon detector structures

Semiconductor photon detectors in can be classified into photoconductors (Figure 1-2b) and photovoltaic detectors -or photodiodes- (Figure 1-2a). Both device structures follow a shared sequence of three fundamental operations. Initially, there's optical absorption, where the absorption of photons leads to the generation of electron-hole pairs (EHPs) inside the active area. The quantity of photogenerated EHPs relies on factors such as the film's thickness, the absorption cross-section of the constituent material, and refractive index difference between active material and air. The second step involves charge separation. Photogenerated EHPs remain in an excited state for a limited period and require spatial separation to prevent recombination (germinate recombination). In photoconductors, this separation is achieved with the assistance of applied bias,

while in photodiodes, a built-in electric field formed at the junction plays a pivotal role in separating charges. The final step encompasses charge collection. The separated electrons and holes must be transported and gathered at the respective electrodes to generate the photocurrent. In photoconductors, minimizing the gap between electrodes ensures that the time taken for photogenerated carriers to reach the electrode (transit time) is shorter than the carrier recombination (non-germinate recombination) lifetime. In photodiodes, ensuring the width of the quasi-neutral region is shorter than the carrier diffusion length is crucial for efficient charge extraction [12]. From an application perspective, photoconductors are often noted for harboring long-lived trapped charges. To maintain charge neutrality, opposite charges circulate through the device multiple times, resulting in a photoconductive gain. This characteristic renders them suitable for high-sensitivity sensor applications, particularly in environments where photon availability is limited [13], [14]. Conversely, photodiodes demonstrate a quicker response time and reduced dark current, meeting the requirements for compatibility with current ROIC operation. This enables their utilization in creating a 2D array for imaging at a high frame rate, eliminating issues such as motion blur or ghosting [15], [16].

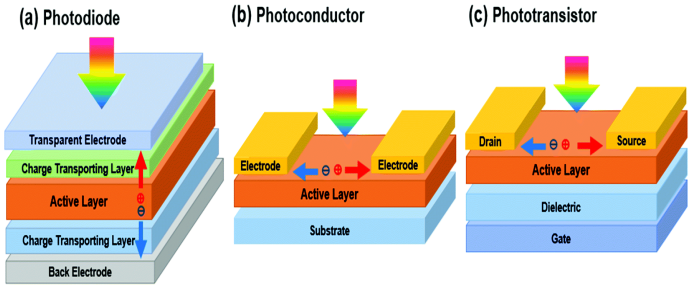


Figure 1-2 Schematic for a) photoconductor, and b) photovoltaic photodetectors. Reprinted from [17].

III. Photodetectors Figure of Merits

Various commercial applications come with specific demands for the features of photodetectors, making it of paramount importance to establish clear evaluation criteria. Today, there exists a wide range of photodetector types, and when assessing and contrasting their performance, it is essential to specify the methodology for deriving index parameters. Consequently, defining the fundamental parameters of photodetectors becomes a crucial step in assessing their appropriateness for various applications. Below, we provide a brief overview and summary of some conventional parameter metrics.

Dark Current

Dark current represents the current that flows within the photodetector in the absence of incident photons. Dark current holds significance in the characterization of photodetectors because it is intimately linked to detector noise, which ultimately dictates the lowest detectable signal level achievable by a photodetector. To ensure fair comparisons among photodetectors of varying sizes, it is more insightful to consider the dark current density, as this parameter normalizes the dark current concerning the device's area.

Photocurrent

The photocurrent represents the current produced by a photodetector when exposed to optical radiation. In the case of a weak radiation signal, the photocurrent exhibits a direct proportionality to the incoming radiation power:

$$I_{Ph} = q\eta A\Phi_e g \tag{1-1}$$

Where q is electron elementary charge, η quantum efficiency and it is a measure of number of charge carriers generated per incident photons. Φ_e is incident power (radiant flux), A is the active area of the device and g is the photoconductive gain. If the lifetime of photogenerated carriers is

larger than the transit time, and one type of carrier (electron or holes) has higher mobility, the device can have a high photoconductive gain because of a process known as photo-recycling [18].

On–off ratio

The on-off ratio (α) is determined as the ratio of the photocurrent (I_{Ph}), or photocurrent density (J_{Ph}), to the dark current (I_{dark}), or dark current density (J_{dark}), at a specific voltage, as represented by the following equation ([19]):

$$\alpha = \frac{I_{Ph}}{I_{dark}} = \frac{J_{Ph}}{J_{dark}} \tag{1-2}$$

Increasing the photocurrent or decreasing the dark current are two methods to increase the on-off ratio.

Response Time

Response time, τ, is usually employed to characterize the sensitivity and speed of the photodetector. In Figure 1-3, the rise time (τ_{rise}) or decay time (τ_{fall}) is the duration of the transient current density increase from 10% to 90% of the maximal current density, or decrease from 90% to 10% of the maximal current density. The response time is in close relation with the film quality, surface roughness, and traps [20], [21].

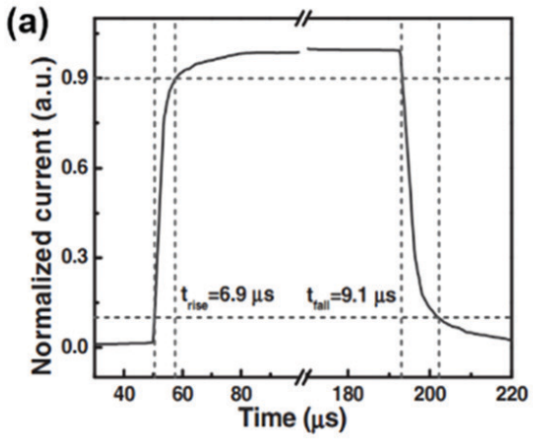


Figure 1-3 Response time of photodetector. Reprinted from Ref. [22].

Responsivity

The term "responsivity," represented as R, in the context of an infrared detector, signifies the relationship between the detector's electrical output signal and the power of the incoming radiation. The units for this responsivity can be expressed as A/W or V/W, and the choice between them depends on the type of photodetector in use, whether it's a photodiode or a photoconductor. The relation is shown below.

$$R = \frac{I_{ph}}{P_{in}} \tag{1-3}$$

Noise

Different noise sources contribute to the total noise of a photodetector, which are presented in the following paragraphs.

Shot Noise

Shot noise is related to the statistical fluctuation in both the dark current and the photocurrent. Δf is noise measurment bandwidth. It is typically chosen to be 1Hz. Also q is elemental electron charge.

$$i_{sh} = \sqrt{2q(I_{ph+}I_{dark})\Delta f} \tag{1-4}$$

$$v_{sh} = \sqrt{2q(I_{ph+}I_{dark})\Delta f} * R = \sqrt{2qV_{Bias+Signal}R\Delta f} \tag{1-5}$$

Johnson or Thermal Noise

The source of thermal noise (or Johnson noise) is related to photodetector resistance. This is because of the thermal generation of carriers. The magnitude of this noise current for photoconductive and photovoltaic photodetectors are

$$v_{th} = \sqrt{4KTR\Delta f} \tag{1-6}$$

$$i_{th} = \sqrt{\frac{4KT\Delta f}{R}} \tag{1-7}$$

Where R is the equalant resistance, K is boltzman constant, and T is the temperature of operation.

Generation-Recombination Noise

The photocurrent depends on average carrier density, which is related to carrier generation rate and lifetime. Thus, it stems from the random generation rate of carriers and the random lifetime of each carrier. In other words, each carrier has a random generation and recombination rate. This noise is similar to shot noise, but instead of the multiplier 2, we have 4 (both generation and recombination).

$$i_{gr} = \sqrt{4qIg\Delta f} \tag{1-8}$$

Where g is the gain of phototdector.

1/f or Flicker Noise

The 1/f noise, also known as flicker noise or pink noise, is a type of noise that is characterized by a spectral density inversely proportional to frequency. In photodetectors, 1/f noise refers to low-frequency noise that can affect the accuracy and sensitivity of the detected signal [23].

$$i_{1/f} = \sqrt{\frac{K_H I^2 \Delta f}{f}} \tag{1-9}$$

K_H is a proportionality constant that depends on the specific material and device characteristics. I is the current, and f is the specific frequency for the $i_{1/f}$ noise measurment.

Total RMS noise current from all contributing currents is defined by equation below:

$$i_n = \sqrt{{i_{sh}}^2 + {i_{th}}^2 + {i_{gr}}^2 + {i_{1/f}}^2} \tag{1-10}$$

Noise Equivalent Power, Detectivity, and NEDT

The NEP is the minimum detectable power of the detector. Combining the responsivity and the total detector noise i_n , the expression of NEP is as follows

$$NEP = i_n/R \tag{1-11}$$

To mitigate the impact of device size and signal bandwidth while concurrently acquiring a more refined measure of a device's detection capability, Jones introduced a specific detectivity (D*) to compare the performance of two detectors with varying sizes and testing bandwidths [24]. The D* is directly related to the signal-to-noise ratio as shown in the equation below. The D* is measured in units of cm.Hz$^{1/2}$/W or Jones.

$$D^* = \frac{\sqrt{A\Delta f}}{NEP} = \frac{I_{ph}}{i_n} * \frac{\sqrt{A*\Delta f}}{P_{in}} \tag{1-12}$$

Another important metric for MWIR photodetectors is Noise Equivalent Temperature Difference (NETD), which serves as a metric that defines the low-signal performance of thermal imaging systems and holds greater relevance in the context of Focal Plane Arrays (FPAs) of infrared detectors. It quantifies the temperature differential between a target and the background temperature required to generate a signal in the detector equivalent to the root mean square (RMS) detector noise. Another definition of NETD involves determining the temperature difference between two blackbodies that corresponds to a signal-to-noise ratio of unity [25].

$$NEDT = \frac{v_n}{v_s}(T_t - T_B) \tag{1-13}$$

Where v_n, v_s, T_t, and T_B are noise RMS voltage, signal RMS voltage, temperature of blackbody target, and background temperature, respectively.

IV. Bulk MWIR Photodetectors

Introduction to MWIR Photodetector Material systems

The development of high-performance mid-wavelength infrared (MWIR) photodetectors continues to be critical for defense, aerospace, environmental monitoring, and industrial sensing applications. The increasing demand for high-operating-temperature (HOT), low-cost, and high-

sensitivity solutions has directed focus toward three dominant material systems: mercury cadmium telluride (HgCdTe or MCT), Type-II superlattices (T2SL), and lead selenide (PbSe). The pursuit of HOT detectors is a technological battle against fundamental noise sources. Each of the technologies discussed in this report—MCT, T2SL, and PbSe—employs a distinct strategy to mitigate dark currents and enable operation at elevated temperatures. MCT technology focuses on perfecting a mature material and optimizing device architecture to minimize known noise sources. T2SL technology takes a more radical approach, using bandgap engineering to create an artificial material with inherently suppressed noise mechanisms. PbSe leverages the unique physics of its polycrystalline structure to achieve respectable room-temperature performance through a different, less understood mechanism. Understanding these distinct strategies is key to evaluating their respective strengths, weaknesses, and potential for future infrared systems.

MCT Photodetectors

Foundational Properties of the HgCdTe Alloy

Mercury Cadmium Telluride, chemically represented as $Hg_{1-x}Cd_xTe$ and commonly known as MCT, has been the preeminent material for high-performance infrared detectors for several decades [26]. Its dominance stems from a unique combination of fundamental properties that make it exceptionally well-suited for IR detection across a wide range of wavelengths. The most significant attribute of MCT is its tunable bandgap. By precisely controlling the molar fraction 'x' of cadmium (Cd) relative to mercury (Hg) in the alloy, the material's bandgap energy can be continuously adjusted [27]. This allows a single material system to be optimized for detection in all of the critical atmospheric windows: the short-wave infrared (SWIR, 1-3 μm), mid-wave infrared (MWIR, 3-5 μm), long-wave infrared (LWIR, 8-12 μm), and even the very-long-wave infrared (VLWIR, >12 μm). For example, an alloy with approximately 30% cadmium

(x=0.3) is used for the MWIR band, while an alloy with 20% cadmium (x=0.2) is used for the LWIR band. This unparalleled flexibility is a core reason for its widespread adoption in military, space, and scientific applications.

However, MCT is not without its challenges. The material is notoriously difficult to produce in large, highly uniform single-crystal wafers [28]. This is primarily due to the very high vapor pressure of mercury, which leads to compositional non-uniformities across the wafer during growth. These non-uniformities translate directly into variations in cut-off wavelength and performance, reducing the yield of high-quality detector arrays and increasing their cost. Furthermore, MCT is a mechanically soft material with low thermal conductivity, making it unsuitable for high-power devices and requiring careful handling during processing. Finally, the presence of mercury and cadmium, both heavy metals, raises environmental and regulatory concerns, with restrictions on their use increasing in some markets, such as Europe [29].

The Evolution to High Operating Temperature (HOT) MCT

The drive to overcome the limitations of cryogenic cooling has spurred significant innovation in MCT device architecture. The development of HOT MCT detectors is not based on a new material but on a sophisticated evolution of the device design aimed squarely at suppressing the dark current mechanisms that dominate at elevated temperatures [28]. The most critical advancement has been the transition from the traditional n-on-p photodiode architecture to a p-on-n structure. In a standard n-on-p device, the infrared radiation is absorbed in a relatively thick, lightly n-doped layer grown on a p-type substrate. However, analysis of dark current sources revealed that the dominant noise mechanism at higher temperatures is the Auger-1 recombination process, which is particularly strong in p-type MCT [27]. The strategic shift to a p-on-n architecture involves using a lightly p-doped absorbing layer grown on an n-type substrate [30].

In this configuration, the dominant recombination mechanism in the absorbing region becomes the Auger-7 process, which is significantly weaker than the Auger-1 process. This architectural inversion directly attacks the primary source of thermal noise, enabling a substantial reduction in dark current for a given operating temperature. This allows for the same dark current performance at an operating temperature approximately 20 K higher than previous n-on-p technologies. This architectural shift was enabled by parallel advancements in material doping. Historically, p-type doping in MCT was achieved by creating mercury vacancies in the crystal lattice, which act as acceptors. However, this method can lead to unstable doping levels and higher defect concentrations. The modern approach utilizes extrinsic doping, where foreign atoms are intentionally introduced into the lattice. Elements like gold (Au) or arsenic (As) are now commonly used to create stable, well-controlled p-type regions. AIM INFRAROT-MODULE GmbH (AIM), a leading manufacturer, reported that transitioning from vacancy doping to extrinsic gold doping allowed them to suppress dark current considerably, enabling MWIR detectors to operate at ~140 K with good performance, a significant increase from the ~120 K limit of their standard technology [30].

State-of-the-Art Performance and Commercial Products

These architectural and material advancements have translated into commercially available MCT detectors with impressive HOT performance, particularly in the MWIR band. AIM has demonstrated high-resolution (1024 x 768) MWIR detectors with a small 10 μm pixel pitch that exhibit excellent performance at an operating temperature of 160 K. Their detectors with a larger 20 μm pitch can achieve NETD of less than 30 mK at operating temperatures up to 170 K [30]. This level of performance at such elevated temperatures allows for the use of smaller, lighter, and more reliable cryocoolers, directly addressing the SWaP+C requirements of modern systems.

Commercial manufacturers also offer uncooled or thermoelectrically cooled MCT products for applications where the ultimate sensitivity is not required. VIGO Photonics provides a wide range of such devices. Their uncooled photovoltaic MCT detectors, like the PVM-10.6, are optimized for LWIR applications such as CO_2 laser detection and offer a peak D* of $\geq 2.0\times10^7$ Jones at room temperature with a cut-off near 12 μm [31]. When thermoelectric cooling is applied, performance increases dramatically. A VIGO two-stage TEC-cooled MCT detector with a cut-off around 7 μm can achieve a D* of 8.0×10^{10} Jones [31]. Teledyne Judson also offers room-temperature photovoltaic MCT detectors, primarily for the SWIR/MWIR boundary. Their J19 series, with a 2.8 μm cut-off, achieves a typical D* of 3.5×10^{10} Jones at room temperature (295 K), demonstrating decent performance for an uncooled photon detector in this spectral range [32].

The development of HOT MCT is a clear example of evolutionary technological refinement. It builds upon decades of investment and accumulated manufacturing expertise. This gives it a significant advantage in terms of technology readiness, reliability, and supply chain maturity compared to newer, more revolutionary technologies [29]. However, the fundamental physics of Auger recombination in the bulk MCT material presents a formidable barrier to achieving high performance at or near room temperature, particularly in the LWIR band. The best uncooled LWIR MCT detectors have D* values in the 10^7-10^8 Jones range, which is several orders of magnitude below their cryogenically cooled counterparts [31]. This performance ceiling creates a strategic opportunity for alternative technologies that are fundamentally designed to overcome this limitation.

Type-II Superlattice Structure Photodetectors

The T2SL Paradigm: Bandgap Engineering for Superior Performance

Type-II Superlattices (T2SLs) represent a fundamentally different approach to infrared detection. Instead of relying on a bulk alloy like MCT, a T2SL is an artificial semiconductor material constructed by growing a repeating stack of ultrathin layers of two different semiconductor materials using techniques like Molecular Beam Epitaxy (MBE) [33]. The most common T2SL systems for infrared detection are based on III-V materials, such as alternating layers of Indium Arsenide (InAs) and Gallium Antimonide (GaSb), or InAs and Indium Arsenide Antimonide (InAsSb) [34].

The defining characteristic of these structures is their "Type-II" band alignment. In this configuration, the conduction band minimum of one material (e.g., InAs) is lower in energy than the valence band maximum of the other material (e.g., GaSb) [35]. This staggered alignment creates quantum wells for electrons and holes in different spatial layers (Figure 1-4). The result is an effective bandgap for the superlattice that is not determined by the bulk properties of the constituent materials, but rather by the quantum confinement effect, which is controlled by the thickness of the individual layers. This gives T2SLs immense design flexibility, allowing their cut-off wavelength to be precisely engineered anywhere from the MWIR to the VLWIR (3-30 μm) simply by adjusting the layer thicknesses during growth [36].

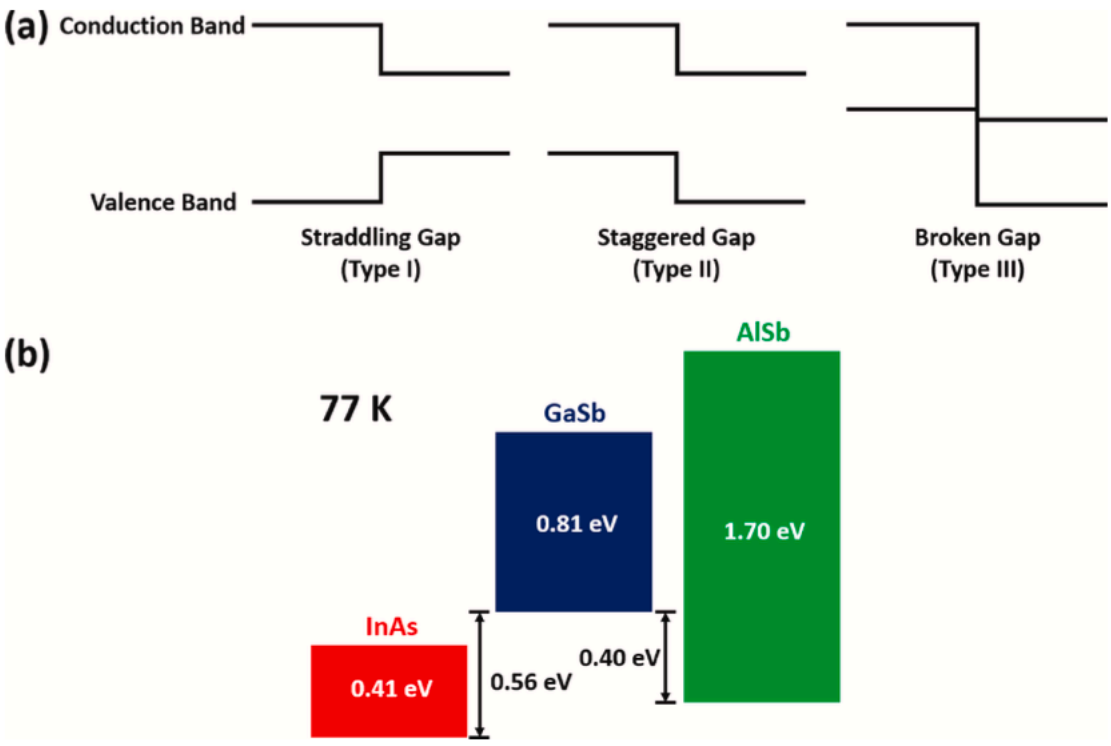


Figure 1-4 (a) Heterostructure band alignment types (b) The band alignment of the 6.1 Å family of semiconductors. Reprinted from Ref. [35].

This bandgap engineering is not just for wavelength tuning; it is the key to the core theoretical advantage of T2SLs: the suppression of Auger recombination. The engineered band structure can be designed to increase the energy thresholds required for the Auger processes that plague narrow-gap bulk semiconductors. By manipulating the energy bands, it is possible to create a structure where Auger recombination is significantly less probable than in MCT with a comparable bandgap [35]. This theoretical prediction of lower Auger rates translates directly into a prediction of lower intrinsic dark currents, which should enable T2SL detectors to operate at significantly higher temperatures than their MCT counterparts [37].

Despite this profound theoretical promise, the practical realization of high-performance T2SL detectors has faced significant hurdles. A primary challenge is a lower optical absorption coefficient compared to MCT [28]. The spatial separation of the electron and hole wavefunctions

in the Type-II structure reduces the probability of optical absorption, necessitating thicker absorber layers to achieve high quantum efficiency [38]. However, a thicker absorber layer means a larger volume for thermal generation of dark current, which can counteract the benefits of Auger suppression. Another major issue has been the material quality itself. The interfaces between the superlattice layers are critical, and defects at these interfaces or within the layers can act as Shockley-Read-Hall (SRH) recombination centers, creating a G-R dark current that can overwhelm the low diffusion current [33]. Finally, carrier transport in a superlattice is anisotropic; transport parallel to the layers is typically much better than transport perpendicular to them. This poor vertical mobility can hinder the efficient collection of photo-generated carriers, reducing the detector's overall responsivity [33].

Architectural Innovations Enabling HOT and RT Operation

The success of modern T2SL detectors is a story of overcoming these practical challenges through clever device engineering. The theoretical promise of the material was unlocked by a series of architectural innovations designed to specifically target its weaknesses.

Arguably the most important of these is the development of the unipolar barrier detector architecture, commonly known by names such as nBn ("n-type contact, Barrier, n-type absorber") or XB-n, where X is a contact layer [39]. In a traditional p-n photodiode, the high electric field exists across the junction, which is where defect-mediated G-R current is generated. In a barrier detector, a thin, wide-bandgap semiconductor layer is inserted between the absorber layer and the contact layer. This barrier is designed to block the flow of majority carriers (the primary source of dark current) but allow the unimpeded flow of minority carriers (including the photo-generated signal) [38]. This architecture effectively eliminates the depletion region from the narrow-gap absorber, thereby suppressing the G-R current component. This leaves only the much smaller

diffusion current from the absorber as the dominant noise source, allowing the intrinsic advantage of the T2SL's low Auger rate to be realized [35].

With the dark current problem addressed by barrier structures, the focus shifted to the low absorption coefficient. To achieve high quantum efficiency without using a thick, noisy absorber, researchers developed light-trapping structures that confine photons within a very thin detector [40]. This has been achieved through two primary methods:

1. Plasmonic Detectors: In this approach, the T2SL barrier detector is integrated with a metallic grating or nanostructure on its surface (Figure 1-5). This structure supports surface plasmon polaritons—collective oscillations of electrons coupled to light—which can trap and concentrate the incident infrared radiation into the very thin absorber layer (e.g., less than 400 nm thick) [37]. This results in a dramatic enhancement of absorption and quantum efficiency at specific resonant wavelengths, enabling high performance in an ultra-thin device.

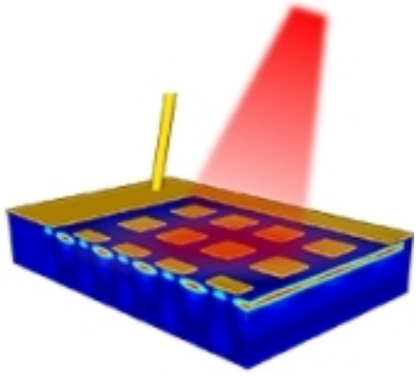


Figure 1-5 Schematic of the plasmonic IR quantum-engineered ultra-thin epitaxial detector. Reprinted from Ref. [41].

2. Guided-Mode Resonance (GMR) Detectors: This is an all-semiconductor approach to light trapping. A diffraction grating is etched into the top of the detector structure, which sits on an epitaxial waveguide layer. At specific wavelengths and angles, the grating couples incident light into a guided mode that propagates laterally within the waveguide and thin absorber [42]. This

resonance traps the light, greatly increasing its interaction path length with the absorber and boosting quantum efficiency. The resonant wavelength is tunable by changing the grating period, allowing for spectrally selective detectors with high polarization sensitivity.

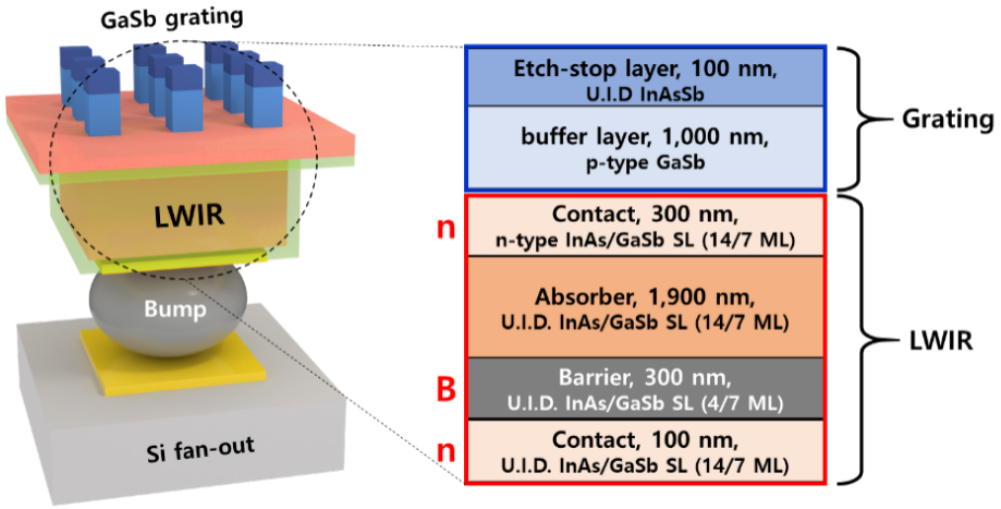


Figure 1-6. Schematic of GMR LWIR detector (left) and its upside-down epitaxial structure after GaSb substate removal (right). Reprinted from Ref. [42].

Research Frontiers and State-of-the-Art Performance

The combination of advanced material growth and innovative device architectures has led to a series of breakthrough results for T2SL detectors, particularly in the realm of high-temperature and room-temperature operation. In the MWIR band, T2SLs have demonstrated true room-temperature, high-performance photon detection. A landmark result was reported for a GMR-based T2SL detector that achieved a room-temperature (296 K) peak specific detectivity (D*) of approximately 1.2×10^{10} Jones at a wavelength of 4.4 μm [43]. This level of sensitivity from an uncooled photon detector is exceptional and rivals that of many thermoelectrically cooled detectors. On the commercial front, Teledyne Judson has developed discrete HOT MWIR T2SL

photodetectors capable of operating at 295 K. These devices show a peak D* of 1.9×10^9 Jones and a responsivity of 2.47 A/W with a cut-off wavelength of approximately 5.5 μm [44].

In the more demanding LWIR band, T2SLs are also pushing the boundaries of high-temperature performance. A plasmonic T2SL detector was shown to operate at 230 K—a temperature readily achievable with a two-stage TEC—while maintaining a peak D* of 2.29×10^9 Jones at 9.6 μm [37]. This performance is nearly an order of magnitude higher than commercially available MCT detectors operating at the same elevated temperature, showcasing the tangible benefits of the T2SL approach for SWaP-constrained LWIR systems.

Crucially, T2SL technology is rapidly transitioning from laboratory research to industrial production. Major defense contractors like L3Harris are now in volume production, having delivered over 3,000 T2SL FPAs for various programs [45], [46]. They are scaling their MBE growth to larger wafer sizes (>125mm), which is essential for reducing costs and increasing the production of large-format arrays. This maturation was accelerated by government-funded programs like the Vital Infrared Sensor Technology Acceleration (VISTA) program [45], [46]. Similarly, European institutions like Fraunhofer IAF report that T2SL technology has reached market maturity and is beginning to replace MCT in some applications [47]. This demonstrates that T2SL is no longer just a promising challenger but a viable and producible technology. This progress is creating a new and highly valuable performance tier in the infrared market, positioned between low-cost, low-performance uncooled thermal detectors (microbolometers) and high-cost, high-performance cryogenic photon detectors. This "HOT" tier, offering a compelling balance of performance and SWaP-C, is set to disrupt the market by enabling a new generation of advanced infrared systems.

Lead-salt Materials

Lead chalcogenides, specifically lead sulfide (PbS), lead selenide (PbSe), lead telluride (PbTe), and the ternary alloy lead-tin telluride (PbSnTe), represent a historically significant and still highly relevant class of semiconductor materials for infrared detection in the MWIR and LWIR regions. The prominence of PbSe and PbS detectors largely stems from their excellent alignment with SWaP+C (size, weight, power, and cost) considerations [8]. These lead-salt detectors exhibit substantial sensitivity and can operate effectively at room temperature or near-room temperature conditions, particularly within the MWIR spectral range, thus substantially reducing system complexity and operational power demands [49], [50]. Moreover, the inherent cost-effectiveness of PbSe and PbS detectors, especially for single-element configurations, distinguishes them from more complex cooled detectors such as MCT [51], [52].

The performance and applicability of lead salt detectors are intrinsically linked to their fundamental material properties. These IV-VI narrow-gap semiconductors share a common rocksalt crystal structure and a direct bandgap located at the L-point of the Brillouin zone [53], [54], [55]. A distinctive feature is their anomalous positive temperature coefficient of the bandgap ($dEg/dT > 0$), meaning their bandgap increases and thus the cutoff wavelength shifts to shorter wavelengths with increasing temperature, which has significant implications for the temperature stability of uncooled or thermo-electrically stabilized detectors[56], [57]. Another common characteristic is their very high static dielectric constant, contributing to high carrier mobilities but also resulting in high device capacitance, historically limiting high-frequency operation [58], [59], [60]. Table 1-1 provides a comparative summary of these properties.

Table 1-1. Fundamental Properties of Lead Salt Detector Materials

Property	PbS	PbSe	PbTe	PbSnTe
Typical Spectral Range(μm)	1-3.3	1-5.2	1.5-5.5	8-14
Crystal Structure	Rocksalt	Rocksalt	Rocksalt	Rocksalt
Bandgap at 300K (eV)	0.41	0.278	0.31	Tunable
Electron Mobility at 300K ($cm^2V^{-1}s^{-1}$)	~600-800	~1000-1020	~6000	Varies with Sn
Hole Mobility at 300K ($cm^2V^{-1}s^{-1}$)	~700-900	~900-1000	~4000	Varies with Sn
Static Dielectric Constant at 300K	~170-175	~200-280	~400	-
High-Freq. Dielectric Constant	~17-18	~23-25	~33-38	-

Lead-salt Materials History

The journey of lead salt detectors began with early 20th-century scientific efforts, significantly accelerating during and after World War II due to military requirements, including Kutzscher's 1933 discovery of PbS photoconductivity [61] and Cashman's subsequent work on PbS, PbSe, and PbTe [62]. Early applications were predominantly military, such as in missile seekers [63]. As technology matured, a gradual shift towards commercial and industrial applications occurred, driven by improving cost-performance ratios [64]. This transition underscored the increasing need for cost reduction, enhanced long-term stability, improved reproducibility, and more rigorously defined performance metrics, which remain key drivers for contemporary research.

PbSe Anomalous Auger Coefficient and HOT Operation potential

The principal obstacle to achieving high performance at room temperature lies in the fundamental physics of the narrow-bandgap semiconductors required for MWIR detection. However, this narrow bandgap also makes them highly susceptible to the thermal generation of

electron-hole pairs. At 300 K, the thermal energy ($k_BT \approx 26$ meV) is a significant fraction of the bandgap energy, leading to a large intrinsic carrier concentration and, consequently, high dark currents that obscure the desired photogenerated signal. While various noise mechanisms contribute to this dark current, including Johnson-Nyquist noise, shot noise, and 1/f noise, the performance of an intrinsically high-quality material is ultimately limited by the rates of thermal generation-recombination (G-R) processes. Among the intrinsic G-R mechanisms—Shockley-Read-Hall (SRH), radiative, and Auger recombination—it is the Auger process that represents the most formidable performance bottleneck for narrow-gap semiconductors at elevated temperatures [65]. Auger recombination is a non-radiative, three-carrier process in which the energy and momentum released from the recombination of an electron-hole pair are transferred to a third carrier (either an electron or a hole), exciting it to a higher energy state. As a third-order process, its rate scales strongly with carrier concentration (e.g., as n^3 in the intrinsic case). Consequently, in the high-carrier-concentration environment of a room-temperature narrow-gap semiconductor, Auger recombination becomes the dominant lifetime-limiting mechanism, generating a significant thermal dark current that dictates the ultimate noise floor of the detector and its D*. The incumbent material for high-performance IR detection, HgCdTe, exemplifies this challenge. Its performance at or near room temperature is severely constrained by a strong Auger recombination rate, which necessitates deep cryogenic cooling to suppress this intrinsic noise source and achieve high sensitivity.

PbSe presents a compelling and fundamentally superior alternative for the development of HOT MWIR photodetectors. This advantage stems not from complex device engineering but from the intrinsic material properties of PbSe, which give rise to an anomalous and profound suppression of Auger recombination. Recent first-principles investigations have revealed that the

Auger processes in PbSe deviate significantly from the behavior observed in conventional narrow-gap semiconductors. Understanding the physics behind this anomaly is critical to unlocking the full potential of PbSe as a next-generation HOT detector material. Recent advancements in first-principles computational materials science have elucidated the unique nature of Auger recombination in PbSe, revealing three distinct anomalies that collectively explain its suitability for high-temperature operation. These findings, detailed by Zhang, Shen, and Van de Walle, challenge long-held assumptions about carrier recombination in narrow-gap semiconductors and provide a robust theoretical foundation for PbSe's intrinsic advantages [66].

Anomaly 1: Profound Suppression of Direct Auger Recombination

The most striking anomaly in PbSe is the extreme inefficiency of the direct Auger process. This process, mediated solely by the Coulomb interaction between carriers, is conventionally believed to be the dominant recombination channel in narrow-gap materials. However, first-principles calculations demonstrate that the direct Auger coefficient in PbSe at 300 K is approximately 1.9×10^{-30} cm^6s^{-1}. This value is a staggering four orders of magnitude lower than that of other semiconductors with similar bandgaps [66]. For instance, MWIR HgCdTe exhibits Auger coefficients typically greater than 10^{-27} cm^6s^{-1} [67]. This is not a minor deviation but a fundamental divergence in material behavior, pointing to a unique underlying physical mechanism.

The origin of this profound suppression lies in the distinctive electronic band structure of PbSe. In its rock-salt crystal structure, the conduction band minimum (CBM) and valence band maximum (VBM) are located at the L-points of the Brillouin zone. The bands in this region are highly dispersive and exhibit a near-mirror-image symmetry with respect to the center of the bandgap [66]. This symmetry and dispersion impose severe constraints on the simultaneous conservation of energy and momentum required for a direct Auger event. For a three-particle

collision to occur, the initial and final states of the carriers must satisfy both conservation laws. In PbSe's band structure, the high dispersion means that a large change in carrier energy (e.g., excitation by an amount equal to the bandgap) necessitates a correspondingly large change in momentum. Finding a set of four carrier states (two initial, two final) that simultaneously satisfies these stringent conditions is statistically improbable, leading to a very low transition rate.

The most critical element of PbSe's band structure responsible for this suppression is the location of its heavy-hole (hh) band. In stark contrast to conventional zincblende semiconductors like GaAs or HgCdTe, where the heavy-hole and light-hole bands are degenerate at the Γ-point band edge, the heavy-hole band in PbSe is situated approximately 1.7 eV below the VBM [66]. This deep-lying heavy-hole band is therefore inaccessible to Auger processes occurring near the band edge. In materials like HgCdTe, the dominant Auger-1 (or CCCH) process involves the recombination of a conduction electron with a heavy hole, transferring the energy to another conduction electron. The presence of a flat, high-density-of-states heavy-hole band at the band edge provides a crucial "momentum reservoir." It allows for a wide range of momentum-conserving transitions without a significant energy penalty, making the Auger process highly efficient [68]. By lacking this accessible heavy-hole band, PbSe effectively closes the most efficient channel for direct Auger recombination, resulting in its anomalously low coefficient. A conceptual depiction of this is shown in Figure 1-7, which contrasts the band structure of PbSe with that of a typical zincblende semiconductor, highlighting the crucial absence of a near-VBM heavy-hole band in PbSe.

A schematic comparing the band structure of PbSe near the L-point is shown in (Figure 1-7 b) with a typical zincblende semiconductor like GaAs near the Γ-point (Figure 1-7 a). The PbSe bandstructure show highly dispersive, symmetric conduction and valence bands, and the

heavy-hole band located ~1.7 eV below the VBM. The GaAs diagram shows the degenerate heavy-hole and light-hole bands at the VBM, illustrating the availability of the heavy-hole states for efficient Auger recombination.

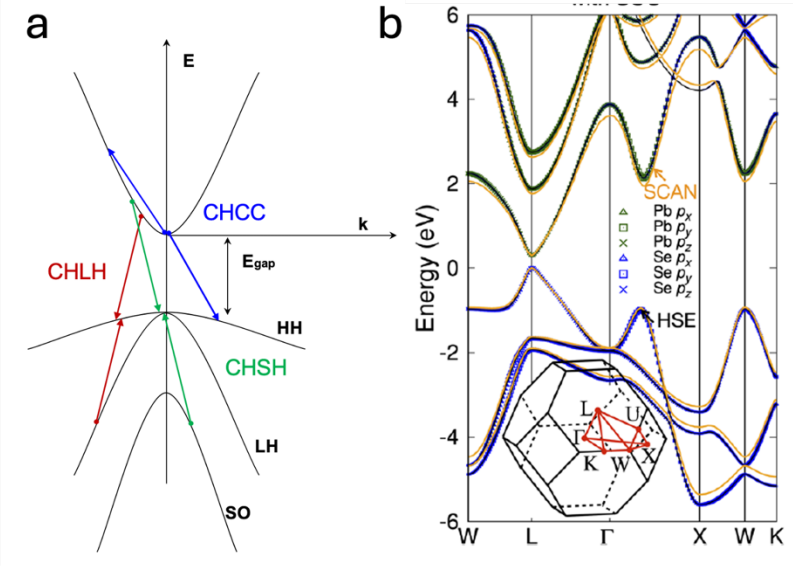


Figure 1-7 (a) Conceptual Band Structure Comparison for different auger recombination for GaAs and (b) PbSe band structure shoeing location of hh band and mirror-like CB and VB at L point. Figures reprinted from Ref. [66], [69].

Anomaly 2: The Ascendancy of the Indirect, Phonon-Assisted Pathway

The extreme suppression of the direct Auger channel in PbSe creates an environment where a higher-order, and typically much weaker, process can become dominant. This second anomaly is the finding that phonon-assisted indirect Auger recombination prevails in PbSe, a conclusion that upends the conventional wisdom for narrow-gap semiconductors [66].

The indirect Auger process involves the participation of a lattice vibration, or phonon, in addition to the three interacting charge carriers. The phonon can be either emitted or absorbed during the event, contributing its momentum, q, to the overall conservation equation. This relaxes the strict momentum conservation constraint that cripples the direct process. The condition becomes k1+k3=k2+k4±q, where the ki are the carrier wavevectors. This relaxation of momentum

conservation dramatically increases the available phase space for final states, opening up a vast number of transitions that were previously forbidden. Consequently, even though it is a higher-order process, the sheer number of available pathways allows the indirect mechanism to have a higher overall rate than the severely constrained direct one. This is conceptually illustrated in Figure 1-8 (A schematic E-k diagram illustrating the mechanics of (a) a direct Auger process, where the vector sum of initial and final carrier momenta must be zero, and (b) a phonon-assisted indirect Auger process, where the inclusion of a phonon momentum vector q allows for a much broader range of momentum-conserving transitions).

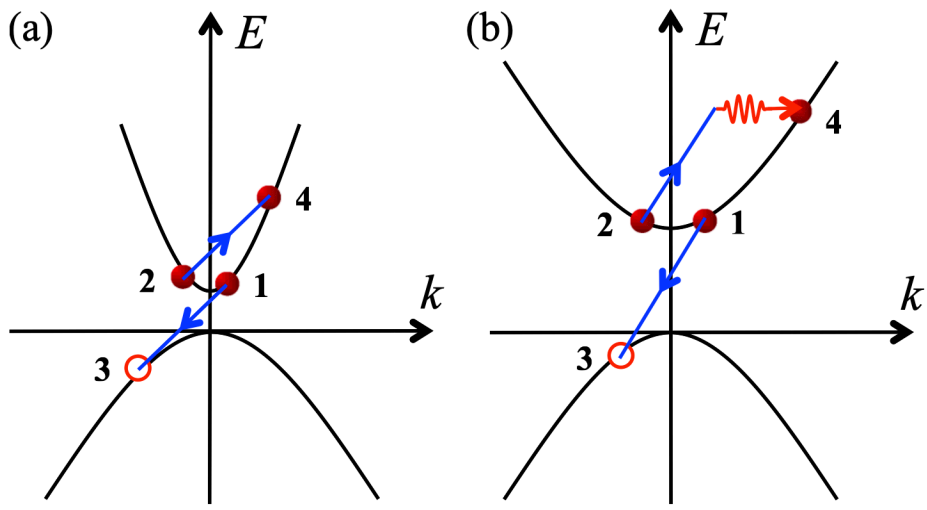


Figure 1-8 Schematic diagram of (a) direct and (b) indirect electron-electron-hole Auger recombination processes. (a) In the direct case, an electron in the conduction band (1) recombines with a hole in the valence band (3) while the excess energy and momentum is transferred to a second electron (2) that gets excited to a higher conduction-band state (4). (b) The indirect process is assisted by a carrier-scattering mechanism, such as electron-phonon coupling, which provides additional momentum and enables Auger transitions to a wider range of final conduction-band states throughout the first Brillouin zone. Reprinted from [70].

This theoretical prediction is strongly supported by quantitative analysis. First-principles calculations yield a room-temperature indirect Auger coefficient for PbSe of approximately

1.1×10^{-28} cm^6s^{-1} [66]. This value is not only more than an order of magnitude larger than the calculated direct coefficient (1.9×10^{-30} cm^6s^{-1} but also falls squarely within the range of experimentally measured values for PbSe, which have been reported as 1.1×10^{-28} cm^6s^{-1} and 0.8×10^{-27} cm^6s^{-1} [66]. The strong agreement between the calculated indirect coefficient and experimental data provides compelling evidence that it is this phonon-assisted mechanism, not the direct one, that governs the total Auger rate in PbSe.

Anomaly 3: A Consequence of Indirect Dominance: Weak Temperature Dependence

The third anomaly, which has been an experimental puzzle for decades, is the remarkably weak temperature dependence of the Auger coefficient in PbSe. This behavior stands in sharp contrast to materials like HgCdTe, where the Auger rate exhibits a strong exponential dependence on temperature, a direct consequence of the thermal energy required to promote carriers to the threshold energy for the direct process [66]. The dominance of the indirect Auger pathway in PbSe provides a clear and direct physical explanation for this observation.

The key lies in the nature of the phonon interaction. The scattering processes that mediate indirect Auger recombination are dominated by phonon emission. Phonon emission is a spontaneous process that can occur at any temperature, as it does not require a pre-existing thermal population of phonons to proceed. This means the indirect recombination channel remains open and efficient even as the temperature is lowered. While phonon absorption also contributes to the indirect rate, this process is temperature-dependent (requiring thermal phonons) and its contribution is secondary to the dominant emission pathway [66]. The overall result is an Auger coefficient that is only weakly dependent on temperature.

This new understanding refutes the long-standing hypothesis that attributed PbSe's weak temperature dependence to its anomalous positive temperature coefficient of the bandgap (i.e., Eg

decreases as temperature decreases). While accounting for the temperature-dependent bandgap does lessen the precipitous drop of the direct Auger coefficient at low temperatures, this is only a "secondary effect." Calculations show that even with this correction, the direct coefficient still drops by many orders of magnitude between 300 K and 50 K. It is only the temperature-insensitive nature of the dominant indirect, phonon-emission-assisted process that can fully explain the experimentally observed trend [66]. This is visualized in Figure 1-9b, which compares the theoretical temperature dependencies of the different processes with experimental data. A semi-log plot showing the Auger coefficient as a function of temperature, Figure 1-9b, feature two distinct curves: (1) the calculated direct Auger coefficient for PbSe, showing a dramatic decrease of over 10 orders of magnitude from 300 K to 50 K; (2) the calculated indirect Auger coefficient for PbSe, showing a nearly flat, weak dependence over the same range, as well as, experimental data points for PbSe overlaid, demonstrating their excellent agreement with the calculated indirect curve.

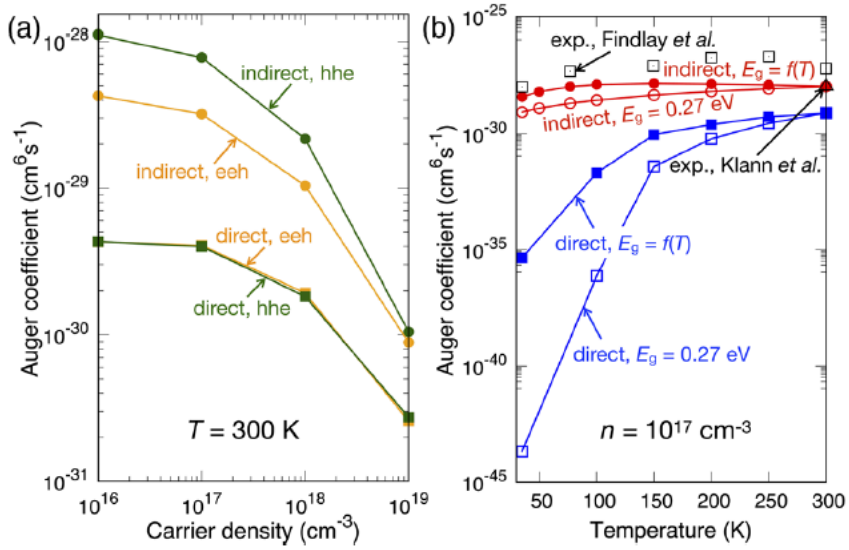


Figure 1-9 Calculated Auger coefficients as a function of carrier density at 300 K. (b) Calculated Auger coefficients as a function of temperature at a fixed carrier density of 10^{17} cm^{-3} [66].

A Fundamental Advantage over HgCdTe and Sb-based T2SL

A direct comparison of intrinsic recombination rates reveals the significant edge held by PbSe. At room temperature, the performance of narrow-gap detectors is overwhelmingly dictated by the Auger-limited carrier lifetime.

Comparison with HgCdTe (MCT): The primary advantage of PbSe over MCT for HOT applications is its intrinsically lower Auger rate. In MWIR MCT (e.g., $Hg_{0.7}Cd_{0.3}Te$), the Auger coefficient at 300 K is typically in the range of 10^{-27} to 10^{-26} cm^6s^{-1}, a rate dominated by the highly efficient direct Auger-1 (CCCH) process enabled by its band structure. This rate is at least one to two orders of magnitude higher than the dominant indirect rate in PbSe (1.1×10^{-28} cm^6s^{-1}) [66]. This fundamental difference implies that, for a given intrinsic carrier concentration, the Auger-limited carrier lifetime in PbSe is significantly longer. A longer lifetime corresponds directly to a lower thermal generation rate, and thus a much lower theoretical dark current. This is precisely

why MCT detectors must be cooled to cryogenic temperatures—to suppress this powerful intrinsic noise source and achieve usable sensitivity.

Table 1-2 Typical Auger lifetime at room temperature for different doping concentrations.

Material	Doping Concentration (cm^{-3})	Auger Lifetime @300K (s)	Bandgap (eV)
PbSe	10^{17}	10^{-7}	0.27
	10^{18}	10^{-8}	
T2SL	10^{17}	$3x10^{-8}$	0-1.6
	10^{18}	$3x10^{-9}$	
MCT	10^{17}	10^{-9}	0.17-1.425
	10^{18}	10^{-10}	

Comparison with Sb-based T2SLs: Antimonide-based Type-II Superlattices (T2SLs) represent a sophisticated, engineered approach to solving the Auger problem. These are complex heterostructures, typically composed of alternating layers of materials like InAs and GaSb or InAsSb, that are meticulously designed to suppress Auger recombination by spatially separating electron and hole wavefunctions and tailoring the band structure to eliminate resonant final states for Auger transitions. While this "band structure engineering" has proven successful, with reported Auger coefficients in the MWIR and LWIR ranges (10^{-27} to 10^{-26} cm^6s^{-1}) that are competitive with or better than MCT, this suppression is an extrinsic property of an artificial, complex structure [71].

In contrast, PbSe's Auger suppression is an intrinsic property of a simple, bulk, binary compound. It is a "naturally optimized" solution provided by its rock-salt crystal structure and inherent electronic properties. This distinction is not merely academic; it has profound implications

for material growth and device manufacturability. While T2SLs demonstrate the power of quantum engineering, their complexity—involving hundreds of ultra-thin layers and hetero-interfaces—makes them highly susceptible to growth-related defects. These defects often introduce mid-gap states that open up efficient Shockley-Read-Hall (SRH) recombination pathways, which can become the dominant noise source, preventing the devices from ever reaching their theoretical Auger-limited performance [72]. The engineering challenge for PbSe is conceptually simpler: improve the crystalline quality of a single material to reduce SRH defects, rather than managing the intricate growth of a multi-layer superlattice. This suggests a potentially more robust and scalable path to achieving Auger-limited performance. Below is comparison for Auger Coefficient foe different material systems.

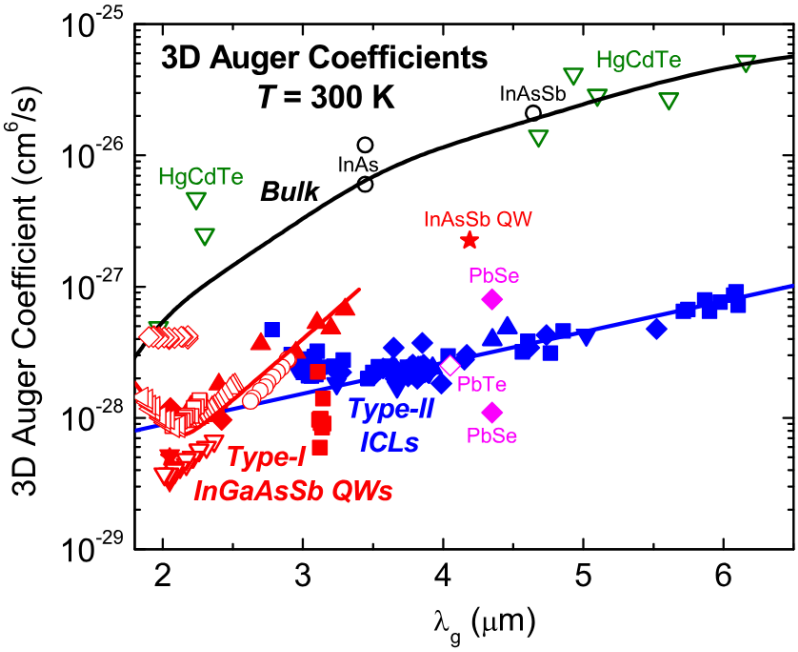


Figure 1-10 Auger Coefficient for different material systems. Reprinted from Ref. [73]

Current Status of Lead-Salt Photodetectors

Although MCT and Type-II superlattice structures exhibit superior performance at cryogenic temperatures, their near-room-temperature operation still lags behind that of PbSe photoconductors. The Auger recombination coefficient in IV–VI semiconductors such as PbSe is approximately an order of magnitude lower than that of Sb-based T2SLs, which themselves exhibit significantly reduced Auger recombination compared to other III–V and II–VI semiconductors, including MCT, for equivalent bandgap energies [74], [75], [76], [77], [78], [79], [80]. There is a demand for high-performance uncooled MWIR photodetectors with low SWaP+C. Need for cryogenic cooling hinders lowering SWaP+C. Single-element lead salt detectors predominantly operate based on the photoconductive effect, where the electrical conductivity of a polycrystalline semiconductor film changes upon illumination. A critical aspect is the sensitization process, as as-grown films exhibit very low photoresponse. To activate infrared sensitivity, a thermal treatment in specific atmospheres, usually involving oxygen and/or iodine, is required [81]. This complex process involves chemical and structural modifications, leading to the formation of various lead oxides, oxysulfides, or oxyselenides such as $PbSeO_3$ at grain surfaces and boundaries[82], [83]. For PbSe detectors, iodine exposure is often critical, potentially acting as an n-type dopant, forming compounds like PbI_2, or serving as an oxidation enhancer that facilitates recrystallization [84], [85], [86], [87]. To date, there is ongoing debate about the dominant operation mechanism. Proposed models include barrier mechanisms, where illumination modulates grain boundary potential barriers changing carrier mobility [88]; charge-separation mechanisms, particularly for PbSe, where sensitization may form p-n junctions at crystallite surfaces creating an n-type shell around a p-type core to spatially separate photogenerated carriers, reduce recombination, and enhance lifetime and responsivity, with oxygen passivating defects or facilitating separation[52],

[89], [90], [91]; and trap-assisted conduction mechanisms, where some researchers suggest oxygen-related traps are central, with iodine acting as an oxidation enhancer[84], [92], [93].

Chemical Bath Deposition (CBD) has been a widely adopted, relatively low-cost, solution-based method for depositing lead salt thin films, particularly for photoconductive devices, and can be adapted for large-area deposition [94]. However, CBD faces challenges in reproducibility and achieving highly uniform films, with properties sensitive to substrate conditions [95], [96], though its simplicity and the high performance of resulting detectors maintain its appeal. Alternatively, Vapor Phase Deposition (VPD) techniques, including thermal evaporation and sputtering, generally provide better control over film uniformity and reproducibility and are more readily compatible with standard semiconductor manufacturing processes [97]. While potentially more expensive for small-scale single-element production, VPD can be more cost-effective for mass production.

The performance of single-element lead salt detectors is characterized by metrics including D*, R, NEP, and response time. For PbS At room temperature (295K), D* values typically range from 10^9 to 10^{11} Jones. Uncooled detectors can achieve D* around 10^{10} Jones, and cooling improves it beyond 10^{11} Jones. For example, Laser Components' uncooled PB25 series offers typical D* values of 3.5×10^{10} Jones at 90 Hz, increasing to 1.1×10^{11} Jones at 650 Hz with responsivity of 8×10^5 V/W [98]; time constants are typically in the hundreds of microseconds to milliseconds range [99]. The PbSe are typically faster than PbS with time constant of less than 10 µs [100]. Laser Components lists a typical D* of 1.8×10^{10} Jones at 1 KHz for uncooled CBD-grown PbSe photodetectors, which cooling it to -50 °C improves it to 3.6×10^{10} Jones [100]. The highest reported detectivity for a CBD-grown PbSe detector, incorporating an antireflection layer, is 4.2×10^{10} Jones [101]. Although CBD-grown PbSe detectors are low-cost and high-

performance, challenges with uniformity and reproducibility have led researchers to explore alternatives like VPD, which offers uniform films and with monolithic integration with silicon readout circuits capability [102], [103]. New Infrared Technologies (NIT) LEPTON series (VPD PbSe) quotes typical uncooled Peak D* of 2×10^9 Jones, and 1×10^{10} Jones for cooled versions [104].

Few papers published in PbTe photodetectors when compared to more popular PbSe and PbS materials. Resonant cavity enhanced (RCE) PbTe detectors have shown D* 0.72×10^{10} Jones for a 3.5 μm RCE device [105]. For PbSnTe operating in the LWIR, D* values around 10^{10} Jones are typically achieved at 77K [63], [106]. A D* of 5.8×10^{10} Jones at 85K has been shown for MBE-grown PbSnSe detector on CaF_2-BaF_2 on silicon substrate with 10.2 μm cutoff wavelength. While PbS and PbSe perform well near room temperature for MWIR, PbTe and PbSnTe require cryogenic cooling for competitive LWIR D*, reducing their SWaP+C advantages over alternatives like microbolometers.

Lead Salt Market Position and Application

Single-element lead salt detectors, particularly PbS and PbSe, are widely used in non-military applications due to their cost-effectiveness and reliable MWIR performance. Major applications include non-dispersive infrared (NDIR) gas sensing for gases such as CO_2, CO, and CH_4 [107], [108], [109]. Their fast response times also make them ideal for flame and spark detection in industrial safety systems [110], [111]. In pyrometry, they enable non-contact temperature measurements [112]. Additional uses span industrial process monitoring, medical diagnostics, and environmental monitoring [113], [114], [115], [116], all benefiting from MWIR spectral sensitivity for selective measurements without the complexity or cost of cryogenic systems.

Core Comparative Performance Table

A direct comparison of key performance metrics is essential for understanding the relative strengths and weaknesses of MCT, T2SL, and PbSe detector technologies. The following table consolidates data from academic research and commercial product datasheets, organized by operating temperature to facilitate a clear, evidence-based assessment. This table quantifies the trade-offs between operating temperature, spectral range, and sensitivity.

Table 1-3 Comparative Performance of High-Temperature Infrared Detectors

Technology	Sub-Type / Model	Operating Temp. (K)	Cut-off Wavelength (μm)	Peak Specific Detectivity (Jones)	Peak Responsivity (A/W)	Reference
T2SL	GMR (Academic)	296	4.8	1.2×10^{10}	N/A	[43]
T2SL	Teledyne	295	5.4	1.29×10^{9}	1.8	[44]
T2SL	Hamamatsu	77K	14.5	1.6×10^{10}	2.6	[117]
InAsSb	Hamamatsu	293K	5.3	1×10^{9}	0.08	
InAs	Vigo System	293	3.5	7.0×10^{9}	1.1	[119]
MCT	Teledyne	183	5	6.8×10^{10}	2.2	[120]
MCT	Vigo Systems	293	5.4	2.5×10^{10}	1.3 A/W	[31]
PbSe	Laser Components	296	~4.7	1.8×10^{10}	42,000 V/W	[100]
PbSe	Uncooled with AR (Academic)	298	~4.7	4.2×10^{10}	-	[101]

Some of the Best reported D* for room-temperature photodetectors for lead-salts as well as competing material systems are depicted in Figure 1-11.

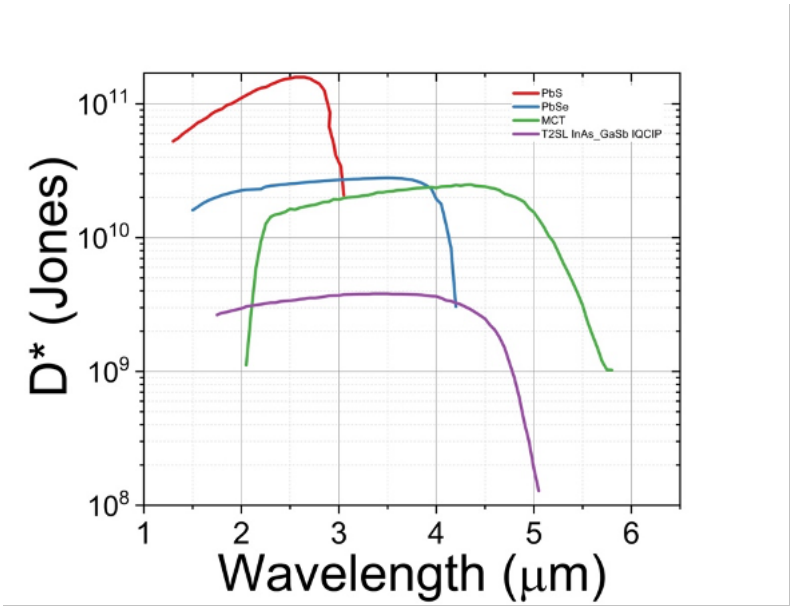


Figure 1-11 D* Comparison between best reported room-temperature MWIR photodetectors. Data gathered from [121], [122], [123], [124].

V. Quantum Dot MWIR photodetectors

QD-based photodetectors have gained significant attention for mid-wave infrared (MWIR) applications due to the unique advantages introduced by quantum confinement. By controlling the size and composition of QDs, their bandgap and cutoff wavelength can be precisely tuned, enabling detectors tailored for specific spectral regions required in gas sensing, thermal imaging, and other MWIR applications. QDs also provide strong and broadband absorption relative to their volume, offering high responsivity and enhanced performance at targeted wavelengths of interest. Additionally, the discrete energy levels in quantum-confined structures can introduce a phonon bottleneck, slowing carrier relaxation and offering the potential for improved high-temperature operation compared to conventional bulk materials. These capabilities position QD-based MWIR detectors as a versatile and powerful platform for next-generation infrared sensing technologies. In the next section the focus is on discussing these properties as well as reviewing the MWIR QD-based photodetectors.

Quantum Effects and their Unique Properties

In a bulk crystal, absorbing a photon create an excited electron in the conduction band and a positively charged "hole" in the valence band. The electron and hole are electrostatically attracted to one another, forming a quasi-particle known as an exciton. This exciton has a characteristic average separation between the electron and hole, termed the exciton Bohr radius. Traditionally, the Bohr exciton radius is defined as [125]:

$$a_B = \frac{4\pi\varepsilon_r \hbar^2}{\mu q^2} \tag{1-14}$$

Where, where ε_r is the relative dielectric constant for the material, q is the electronic charge, ħ is the reduced Plank's constant, and μ is the reduced mass of the electron-hole bound state. Where it can be calculated from

$$\mu = \frac{m_e^* m_h^*}{m_e^* + m_h^*} \tag{1-15}$$

where m_e^* and m_h^* are the effective mass of electrons and holes, respectively. This radius represents the intrinsic length scale of the electron-hole pair in the material. The quantum confinement regime is entered when the physical dimensions of the semiconductor crystal become smaller than the exciton Bohr radius. In this scenario, the electron and hole are no longer free to adopt their natural separation; their motion is spatially restricted by the physical boundaries of the nanocrystal. This spatial enclosure fundamentally alters the energy spectrum of the charge carriers, moving the system from the classical domain of bulk properties into a quantum mechanical domain where size and shape dictate behavior [126].

In a quantum well, such as a thin film of GaAs sandwiched between layers of AlGaAs, carriers are confined in only one dimension (e.g., the growth direction, z). Their energy associated with motion in this direction becomes quantized into a set of discrete levels (E_n). However, they

remain free to move in the other two dimensions (the x-y plane). The total energy of a carrier is thus the sum of a quantized component and a continuous component: $E_{Total} = E_n + \frac{\hbar^2(k_x^2+k_y^2)}{(m^*)^2}$. This results in the formation of a series of two-dimensional "sub-bands.

When confinement is applied in two dimensions, carriers are only free to move along the length of the wire. This results in the formation of one-dimensional sub-bands, where the energy along the wire are determined by the quantization in the two confined directions.

Quantum dots (QDs) are semiconductor nanocrystals with zero dimensions, characterized by their sizes that are either smaller than or similar to the exciton Bohr radius of the semiconductor material. The small dimensions of the QDs lead to quantum confinement effects, including the vanishing of band energies in favor of discretely quantized energy states. This results in narrower photoluminescence peaks, adjustable bandgap, and cutoff wavelength, and enhanced material quality in each QD [127], [128]. If the size of QDs becomes smaller than the Bohr radius in a specific semiconductor material, the conduction and valence bands change to discrete energy levels, instead of a continuous band structure. The discrete energy levels in the band structure can be seen in the absorption spectra of CdTe QDs in Figure 1-12. The first absorption peak can be ascribed to the 1S(h) to 1S(e), and 2S(h) to 1S(e) excitonic transition.

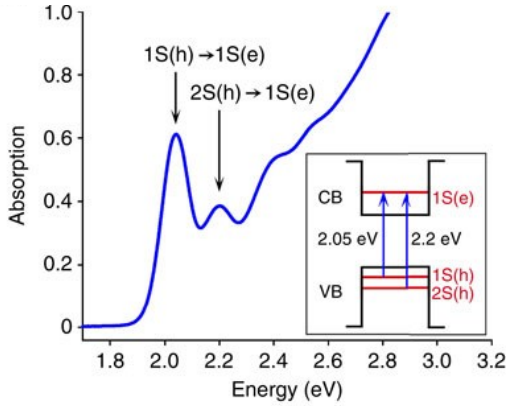


Figure 1-12. The steady-state absorption spectrum reveals the 1st exciton 1S(h)→1S(e) and the 2nd exciton 2S(h)→1S(e) transitions within CdTe quantum dots. The inset energy band diagram illustrates these absorption transitions between the quantum-confined electron (e) and hole (h) energy states. Potential energy wells in the conduction band (CB) and valence band (VB) are represented by the black lines. For clarity, the energy levels are not depicted to scale, and higher energy levels have been excluded. Reprinted from Ref. [129].

Engineering the Electronic Bandgap and Optical Properties

The quantization of the energy spectrum provides a powerful toolkit for engineering the optoelectronic properties of semiconductor materials. In bulk semiconductors, properties like the bandgap are intrinsic and fixed. In the quantum confinement regime, these properties become extrinsic, designable parameters.

The most prominent and technologically significant consequence of quantum confinement is the size-dependent tunability of the effective bandgap. The total energy of the lowest-energy electron-hole pair (the exciton) in a QD is the sum of the bulk material's bandgap energy and the confinement energies of the electron and hole. The confinement energy term is inversely related to the size of the dot. Therefore, as the size of the quantum dot decreases, the confinement energy increases, leading to a larger effective bandgap and a corresponding blue-shift in the onset of optical absorption and the peak of photoluminescent emission. This principle is famously demonstrated in materials like Cadmium Selenide (CdSe), where simply by varying the

nanocrystal diameter during synthesis, the emission color can be tuned across the entire visible spectrum, from red for larger dots to blue for smaller dots [126].

Furthermore, quantum confinement directly enhances the efficiency of light emission. The radiative recombination rate—the probability that an electron-hole pair will recombine and emit a photon—is proportional to the square of the overlap integral of the electron and hole wavefunctions. In a QD, both carriers are forced into the same small volume, leading to a very strong spatial overlap and a high probability of radiative recombination. In contrast, an exciton in a bulk semiconductor is not spatially confined and can dissociate more readily, allowing the electron and hole to diffuse apart and encounter defects or other non-radiative recombination centers. This intrinsic enhancement of radiative efficiency is a key reason why QDs are highly promising for applications like displays and lighting. The composition can be engineered by creating core/shell heterostructures. Using a shell material with a specific band alignment relative to the core can be used to spatially separate the electron and hole (a "Type-II" alignment), which can be used to tune recombination lifetimes and suppress non-radiative processes like Auger recombination.

Density of States as a function of dimensionality

The influence of quantum confinement in quantum dots can be understood through the density of states (DOS) function. DOS characterizes the number of states per unit of energy within a system and holds significance in determining the carrier concentration and energy density in a semiconductor. In larger, bulk semiconductors, the DOS function within a single band is continuous, signifying that carriers (electrons and holes) aren't physically confined in any direction. In a bulk semiconductor, electrons are free to move in all three dimensions. The number of available states in momentum space (k-space) up to a certain energy is proportional to the

volume of a sphere. This leads to a DOS that is continuous and increases with the square root of energy above the band edge.

When one dimension is confined, the energy is quantized into a series of sub-bands. Within each sub-band, the electrons behave as a 2D gas. The DOS for a 2D system is constant with respect to energy for each sub-band. The total DOS is therefore a step-like function, with a new step appearing at the onset of each successive sub-band.

With confinement in two dimensions, the DOS becomes even more sharply peaked. The function exhibits singularities at the bottom of each 1D sub-band. These sharp peaks signify a high concentration of states at the band edges.

In a quantum dot, with confinement in all three dimensions, the concept of a continuous band of states vanishes entirely. States exist only at discrete, quantized energy levels. The DOS, therefore, becomes a series of Dirac delta functions. In a real ensemble of dots, inhomogeneous broadening due to size variations will smear these delta functions into a series of Gaussian-like peaks. Figure 1-13 shows the density of states for different material structures.

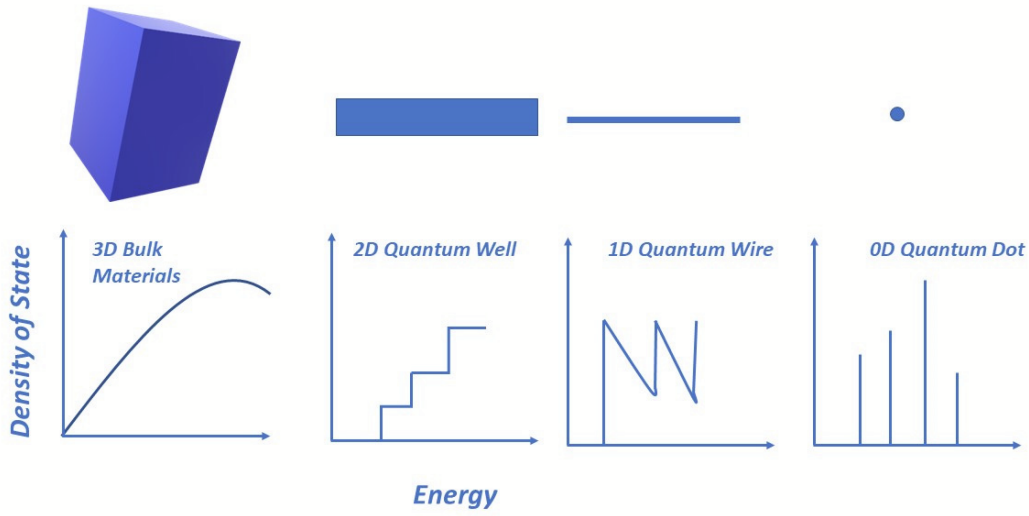


Figure 1-13 Density of States in different material structures. Reprinted from Ref. [130].

Electron Dispersion Relations (E-k Diagrams)

The E-k diagram, which plots electron energy versus crystal momentum, provides a complementary and equally crucial perspective. It can be viewed as the "road map" for electron motion and interactions within the crystal. Any process that changes an electron's energy and momentum, such as scattering, must begin and end at valid points on this map.

3D (Bulk): For a typical direct-gap semiconductor, the E-k diagram near the center of the Brillouin zone consists of continuous, parabolic bands for both the conduction and valence bands. The energy is a quadratic function of the momentum, $E(K) = E_c + \frac{\hbar^2(k^2)}{(m^*)^2}$. This continuous relationship means that for any given energy change, there is a continuum of final momentum states available for a scattering event. The E-k diagram, which plots electron energy versus crystal momentum (wavevector k), provides a complementary and equally crucial perspective (Figure 1-14 a). It can be viewed as the "road map" for electron motion and interactions within the crystal. Any process that changes an electron's energy and momentum, such as scattering, must begin and end at valid points on this map.

2D (Quantum Well): The E-k diagram for a quantum well reflects its hybrid nature. The energy axis shows the discrete quantization levels from confinement in the z-direction. From each of these discrete levels, a continuous parabolic sub-band extends in the k_x-k_y plane, representing the free motion of carriers parallel to the well (Figure 1-14 b).

1D (Quantum Wire): The dispersion relation for a quantum wire consists of a series of 1D parabolic sub-bands, where energy is continuous only for momentum along the axis of the wire (Figure 1-14 c).

0D (Quantum Dot): For a quantum dot, the concept of a dispersion relation breaks down. Since the electron is confined in all directions, it cannot be described by a propagating wave with

a well-defined crystal momentum k. The E-k diagram collapses into a series of discrete, horizontal lines at the quantized energy levels. The energy levels are "flat" with respect to k (Figure 1-14 d).

The transformation of the E-k diagram from continuous parabolas to discrete flat bands is the graphical representation of the localization of the electron wavefunction. This localization has profound consequences for any process that requires momentum conservation, most notably electron-phonon scattering. The absence of a continuum of final states in the QD E-k diagram is the fundamental origin of the phonon bottleneck.

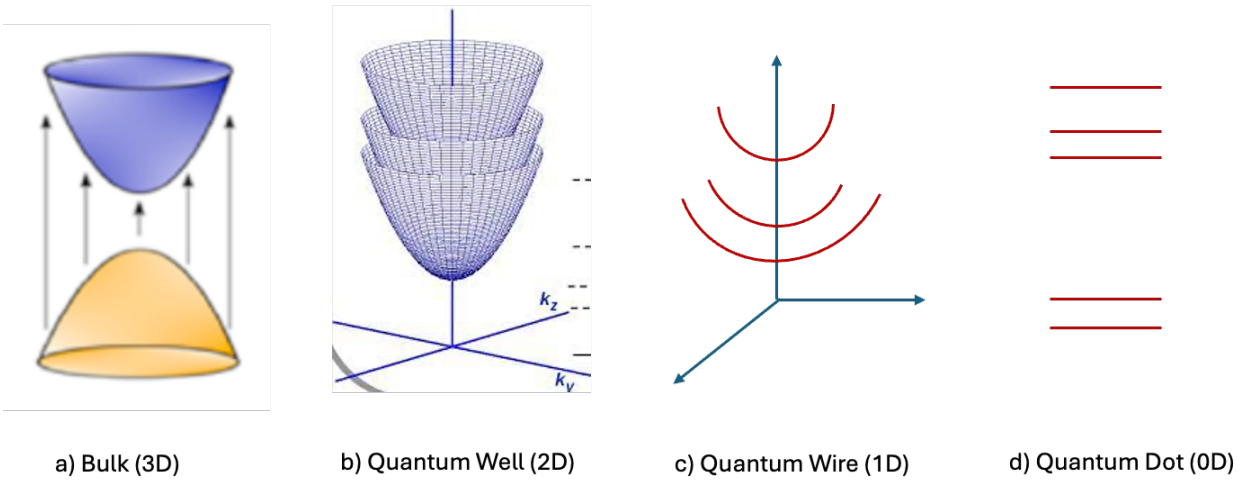


Figure 1-14 Electron Dispersion (E-k) for a (a) Bulk (3D) Semiconductor. A standard E-k diagram for a direct-gap bulk semiconductor. The vertical axis is Energy (E) and the horizontal axis is momentum (k). It shows a continuous parabolic conduction band and a continuous parabolic valence band, both centered at k=0 (the Γ point). Reprinted from Ref. [131] (b) Electron Dispersion (E-k) for a Quantum Well (2D). The energy axis shows discrete levels. From each of these levels, a 2D parabolic sub-band extends, representing free motion in the unconfined plane. The overall structure looks like a series of stacked parabolas. Reprinted from Ref. [132](c) Electron Dispersion (E-k) for a Quantum Wire (1D). The dispersion relation for a quantum wire consists of a series of 1D parabolic sub-bands, where energy is continuous only for momentum along the axis of the wire. (d) Electron Dispersion (E-k) for a Quantum Dot (0D). The diagram shows a series of discrete, horizontal lines. The energy levels do not change with k, indicating they are localized states with no dispersion.

Carrier Relaxation Dynamics and the Phonon Bottleneck

Charge carriers that are optically or electrically injected into a semiconductor are typically created with excess kinetic energy, so-called "hot carriers." For most optoelectronic devices to function efficiently, these hot carriers must rapidly relax, or "cool," to the bottom of the conduction band (for electrons) or the top of the valence band (for holes) before they can recombine radiatively. This cooling process is overwhelmingly mediated by the interaction of carriers with the crystal lattice vibrations, or phonons. The unique electronic structure of quantum dots, as detailed in the previous section, dramatically alters these relaxation dynamics, leading to a phenomenon known as the phonon bottleneck.

Phonons are the quantized modes of vibration in a periodic, elastic arrangement of atoms, such as a crystal lattice. They are the quasiparticles of sound and heat. In semiconductors, two main types of phonons are relevant for carrier relaxation:

Acoustic Phonons: These correspond to long-wavelength vibrations where adjacent atoms move in phase, analogous to sound waves. They have a linear dispersion relation near the Brillouin zone center and possess a continuous spectrum of low energies. Scattering with acoustic phonons is a quasi-elastic process, meaning it changes the carrier's momentum significantly but its energy only by a small amount [133]. This type of scattering is primarily responsible for limiting carrier mobility at moderate temperatures.

Optical Phonons: These involve out-of-phase motion of adjacent atoms in the crystal's unit cell. They have a much flatter dispersion relation and a relatively large, discrete energy, typically in the range of tens of meV (e.g., ~36 meV for longitudinal optical (LO) phonons in GaAs) [134]. In polar semiconductors (like most III-V), the oscillation of oppositely charged ions in an LO phonon mode creates a macroscopic electric field. This field couples very strongly with

charge carriers via the Fröhlich interaction, making LO-phonon emission the most efficient mechanism for hot carrier cooling. A hot electron can lose a large quantum of energy in a single, rapid (~100 fs to 1 ps) scattering event by emitting an LO phonon[135].

When carriers are confined in one dimension (quantum-well, 2D) the electronic spectrum becomes a set of discrete subbands (Figure 1-14 b) in the confinement direction but remains continuous in the in-plane k-space. This partial quantization reduces the available phase space for vertical (out-of-plane) transitions and can narrow the set of final states that satisfy $\Delta E = \hbar\omega_{LO}$; as a result LO-mediated cooling can be slow relative to bulk in specific transitions (for example between subbands), but—because in-plane momentum is still continuous—complete suppression of single-phonon relaxation is rare. The QW case therefore occupies an intermediate regime: confinement reduces but does not eliminate LO pathways, as other effects control the actual relaxation rate [136].

Full zero-dimensional confinement (quantum dots) produces discrete electronic levels and is where the idealized phonon bottleneck argument originates: if the interlevel spacing ΔE is not equal (within the phonon linewidth) to an integer multiple of available optical-phonon quanta, single-phonon transitions are energetically forbidden (Figure 1-15). With the primary relaxation pathway blocked, the carrier must resort to much slower, higher-order processes to lose energy:

Multi-phonon Emission: The electron could simultaneously emit multiple phonons (e.g., several LO phonons or a combination of LO and acoustic phonons) whose total energy sums to ΔE. Such multi-particle processes have a much lower probability and are therefore significantly slower.

Acoustic Phonon Emission: Relaxation via acoustic phonons is possible, but since each acoustic phonon carries away only a very small amount of energy, a vast number of such scattering

events would be required to bridge a large energy gap, making the process extremely inefficient [137].

Despite the compelling theoretical prediction of a phonon bottleneck, its experimental observation has proven to be exceptionally challenging. Most time-resolved spectroscopic studies on QDs have revealed hot-carrier relaxation times on the picosecond scale, nearly as fast as in bulk materials, and often showing that relaxation rates increase as the dot size decreases (and the energy spacing increases) [138]. This discrepancy points to the existence of alternative, efficient relaxation pathways that circumvent, or "break," the phonon bottleneck.

Several key mechanisms have been identified that can provide these fast, alternative relaxation channels [138]:

- **Auger-type Processes:** This is one of the most significant bottleneck-breaking mechanisms. In this process, the excess energy of the hot electron is not transferred to the lattice as phonons, but is instead transferred via Coulomb interaction to another charge carrier, typically a hole. The hole is excited deep into the valence band. If for examplebb the valence band states are much more closely spaced than the conduction band states, the hole can then rapidly relax back to the band edge by emitting a cascade of phonons. This electron-to-hole energy transfer provides a very efficient bypass of the electron's phonon bottleneck [138].
- **Surface and Defect States:** Real-world QDs are not perfect crystalline structures. The surface of the dot, often coated with organic ligands, can host a variety of electronic states. Similarly, crystalline defects can introduce energy levels within the bandgap. If these extrinsic states have energies that lie between the QD's intrinsic excited and ground states, they can act as intermediate steps, mediating rapid, sequential relaxation and effectively short-circuiting the bottleneck [138].

The existence of these competing pathways explains why the phonon bottleneck is observed only under very specific conditions, such as in highly perfect core/shell structures designed to minimize surface defects and spatially separate electrons and holes to reduce Auger-type interactions.

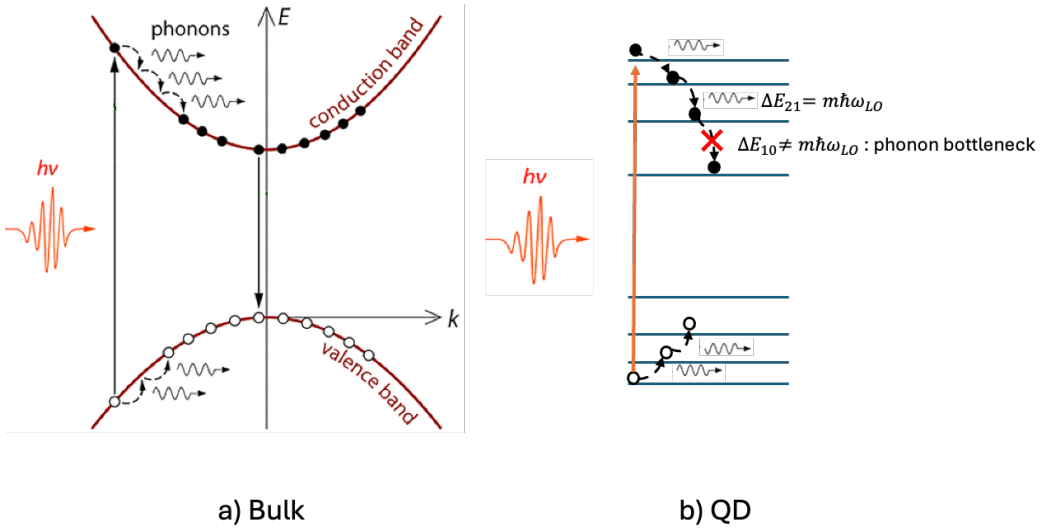


Figure 1-15 Phonon-assisted hot carrier relaxation in a) Bulk semiconductor. The continuous parabolic bands make the electron relaxation with acoustic and optical phonons very easy and accessible. b) QD the discrete energy bands reduce probability of relaxation of electron or hole via acoustic phonons and make it difficult via optical phonon if the energy difference between sub bands are larger than the LO phonon energy.

Colloidal Quantum Dot Photodetectors

CQD synthesis involves a chemical approach to produce nanoscale semiconductor particles suspended in a solution, known as colloids. This process typically utilizes precursors—such as metal salts and coordinating organic molecules—that are thermally decomposed or reacted under controlled conditions, leading to the nucleation and growth of nanocrystals. The synthesis can occur in organic solvents or aqueous solutions and is often conducted in the presence of stabilizing ligands or surfactants to control particle size, and shape, and prevent aggregation [139]. Precise

control over reaction parameters, including temperature, precursor concentrations, and reaction duration, plays a crucial role in determining the size, composition, and optical properties of the resulting colloidal QDs. The versatility and tunability of these synthetic methodologies enable the production of QDs with tailored characteristics, making them valuable for a wide range of applications [140]. Different material systems with interband and intraband absorption can be used to synthesize MWIR-sensitive QDs, which will be discussed below.

Photoconductive HgTe CQD-based devices

The leading material for MWIR CQDs is HgTe [141]. It is considered a semimetal or zero-bandgap with an inverted band structure [142]. Therefore, with quantum confinement, it can cover MWIR. The first demonstration of MWIR HgTe CQD photoconductors in 2011 established the foundation for this field [143]. Simple deposition techniques, such as drop-casting CQD films onto interdigitated electrodes, yielded devices with room-temperature responsivity exceeding 100 mA/W at a 6 μm cutoff wavelength [144]. Detectivity reached 2×10^9 Jones at 130 K, with response times as fast as 100 ns, making them suitable for imaging applications. However, these early devices were limited by substantial 1/f noise, high dark current, and environmental instability [144].

Subsequent work introduced inorganic ligands like As_2S_3 to enhance carrier mobility and air stability, while reducing noise. This approach improved detectivity by 30 times, reaching 10^{10} Jones at 230 K for CQDs with a 3.5 μm absorption peak [142], [145]. Additionally, the transparency of As_2S_3 in the MWIR region helped maintain optical performance, whereas organic ligands introduced parasitic vibrational absorption [12].

Efforts to expand the spectral versatility of HgTe CQDs enabled multicolor imaging through the fabrication of 2×2 multicolor pixel arrays on flexible substrates, employing four

distinct CQD sizes to cover cutoffs from 2.3 to 4.3 μm [146]. Room-temperature detectivities ranged from 6×10^8 to 8×10^9 Jones, depending on the pixel's targeted wavelength [146], indicating the potential of HgTe CQDs for multispectral imaging platforms.

However, scale-up to full focal plane arrays (FPAs) revealed processing challenges. The first MWIR CQD-based FPA (320×256 pixels, 30 μm pitch) suffered from non-uniform CQD layers due to drop-casting, leading to high variability in dark current and responsivity across the array [147]. While under-optimized, the array still achieved an average detectivity of ~1.46×10^9 Jones at 95 K, with an NEDT of 2.3 K, demonstrating feasibility despite material and process limitations [148].

Photovoltaic HgTe CQD-based devices

To mitigate the 1/f noise inherent in photoconductors, researchers transitioned to photovoltaic architectures, operating under zero-bias conditions to suppress dark current. Schottky diode devices utilizing ethanedithiol/HCl ligand-exchanged CQD films, with Ag top contacts, exhibited responsivities of ~80 mA/W, and detectivity improved to 10^{10} Jones at 140 K [98]. Integration of an Ag_2Te CQD interlayer between the HgTe layer and metal contact further improved junction quality, raising detectivity to 4×10^{10} Jones at 90 K and extending spectral response up to 5.25 μm [149].

Next-generation photovoltaic devices introduced ITO bottom contacts for improved band alignment with the CQD conduction band and incorporated $HgCl_2$-treated Ag_2Te CQD interlayers for stable junction formation. These advanced designs achieved detectivities exceeding 10^{11} Jones below 100 K, with ~10^9 Jones at 230 K, outperforming conventional microbolometers and moving closer to cooled semiconductor detector performance [150]. When combined with interference-

based optical enhancement structures, the devices further demonstrated thermal imaging with an NEDT of 56 mK at 90 K [150].

Recent breakthroughs have integrated plasmonic nanostructures with interference-enhanced device architectures to maximize optical absorption and responsivity. By optimizing CQD layer thickness, metal contact geometries, and plasmonic resonance conditions, responsivities as high as 1.46 A/W at 4.5 μm have been reported, with detectivities of ~10^{10} Jones at 220 K. These devices achieved exceptional thermal imaging performance, recording an NEDT of 14 mK, competitive with high-end cooled detectors [151].

The highest performing MWIR HgTe CQD device to date employs a gradient-doped p-i-n homojunction architecture with tailored doping profiles across the CQD layers, optimized for carrier extraction and reduced recombination [152]. This design maintained a high detectivity of >10^{11} Jones below 200 K, and ~7.6×10^{9} Jones at 300 K, with a cut-off wavelength of 3.5 μm [152]. Importantly, the external quantum efficiency (EQE) reached 77% at 80 K, approaching that of epitaxial MCT photodetectors [152]. The introduction of gradient doping notably increased open-circuit voltage and photocurrent, while extending the background-limited infrared photodetection (BLIP) temperature from 120 K to 200 K, a significant milestone for CQD technologies [152].

Ag2Se CQD-based devices

The pursuit of alternative colloidal quantum dot (CQD) materials for mid-wavelength infrared (MWIR) detection has intensified, motivated by the toxicity concerns associated with mercury-based compounds such as HgTe and HgSe. Among the potential candidates, silver chalcogenides, particularly Ag_2Se CQDs, have emerged as promising materials. While initial expectations focused on leveraging interband transitions for MWIR detection, the unique

electronic properties of Ag_2Se CQDs have shifted attention toward intraband transitions, offering distinct pathways to achieve tunable MWIR response. Bulk Ag_2Se possesses a narrow bandgap of 0.05–0.18 eV [153], theoretically suggesting suitability for interband absorption in the MWIR range through quantum confinement. However, practical studies revealed that Ag_2Se CQDs predominantly exhibit near-infrared interband absorption features, as the expected interband MWIR peak is effectively bleached under operating conditions [154]. This unexpected spectral behavior is attributed to the intrinsic silver-rich stoichiometry of Ag_2Se CQDs, which results in an excess of free electrons within the quantum dots. These surplus carriers facilitate prominent intraband transitions, whose absorption peaks can be finely tuned by controlling CQD size.

The first photoconductive devices fabricated from Ag_2Se CQDs, utilizing ethanedithiol (EDT) ligand-exchange techniques, displayed limited performance with responsivity on the order of just a few μA/W—several orders of magnitude lower than the performance of comparable HgSe CQDs [155]. These early results highlighted the challenges in achieving effective carrier extraction and electronic coupling in Ag_2Se CQD solids and underscored the need for improved device architectures.

Recognizing the limitations of standalone Ag_2Se CQDs, Hafiz et al. proposed an innovative strategy by integrating Ag_2Se with PbS CQDs to form a binary CQD system, specifically designed to suppress free carrier densities and enhance photodetector performance [156]. The approach leverages the immobility of ground state carriers in both materials to achieve a significant increase in dark resistivity—from 1×10^3 Ω·cm in pure Ag_2Se CQD films to 2×10^5 Ω·cm in the binary composite [156]. This dramatic improvement mitigates dark current and enhances detector sensitivity. Device fabrication involved constructing a layered architecture starting with Cr/Au bottom electrodes, followed by a 15 nm MoO_x interlayer to improve hole injection into the PbS

QD layer. A 200 nm-thick binary film of PbS/Ag_2Se CQDs was deposited through iterative spin-coating and EDT ligand exchange, ensuring good electronic coupling. Subsequently, an 80 nm ZnO nanoparticle layer was added to form the n-side of the p–n junction, topped by an Al electrode with finger openings to define a 200 × 200 μm^2 active area. The energy band alignment in this heterojunction design facilitates effective separation of photoexcited carriers: upon infrared illumination, electrons generated in the Ag_2Se CQDs are efficiently transported toward the Al cathode, functioning analogously to epitaxial quantum dot infrared photodetectors (QDIPs). The device demonstrated strong rectifying behavior, with a rectification factor of 6000 at 5 V bias, confirming effective junction formation [156]. Performance metrics of this heterojunction photodiode were notably improved compared to initial photoconductive devices. The reported peak responsivity reached 19 mA/W, and the specific detectivity achieved 7.6×10^6 Jones at 300 K, with an absorption cut-off at 6 μm [156]. While these values are modest relative to state-of-the-art HgTe CQD devices, they represent a substantial step forward for mercury-free CQD MWIR photodetectors operating at room temperature.

Lead-chalcogenide interband QDs

One of the most studied QD systems for infrared optoelectronics is the lead-chalcogenide CQDs. Lead-chalcogenide materials with a direct band gap of 0.41 for PbS [157], 0.36 for PbTe [158], and 0.28 for PbSe, [158] have been widely used in bulk MWIR photodetectors[89], [95], [159], [160]. Therefore, photodetectors of lead-chalcogenide QD can be fabricated with great tunability. Lead-chalcogenide CQD photodetectors demonstrate considerable potential in responsivity; however, their exploration has predominantly focused on NWIR [161], [162] and SWIR ranges. This narrowed scope is primarily due to constraints in synthesizing sizable CQDs. Challenges include low air stability and difficulties associated with cation exchange, particularly

for growing shell cadmium-chalcogenides [147]. The air stability limitation concerning larger-size PbSe CQDs stems from ineffective surface defect passivation. These larger PbSe CQDs often develop in the (100) orientation, characterized by a precise balance between lead and selenium atoms, leaving minimal available dangling bonds essential for efficient ligand binding. Consequently, these larger PbSe CQDs exhibit elevated levels of surface defects, significantly hindering their overall performance [24].

In 2019 our group demonstrated the creation of MWIR uncooled PbSe-QDs/CdS p–n heterojunction photodiode through wet-chemical synthesis. After annealing at 673 K for 0.5 hours, the ligand-free PbSe-QDs/CdS photodiode showcased an MWIR spectral photoresponse with a 4.2μm cutoff at room temperature. A 300nm CdS film was deposited onto thermally grown CdSe on a silicon substrate with the CBD method. Later, 1.2μm lead-salt QD films were deposited directly in ambient atmosphere conditions, which is one of the advantages of CBD-grown PbSe QDs. Later 200×200 μm^2 pixels are created by etching the film and gold contact deposition on top. Additionally, indium-doped cadmium selenide (CdSe:In) films exhibited promising qualities for MWIR transparent conductive electrodes due to their low sheet resistance, high optical transmission, and excellent chemical stability. A maximum room-temperature peak responsivity and specific detectivity of 0.36 ± 0.04 A/W and $(8.5 \pm 1) \times 10^8$ Jones, respectively, is achieved for this device. Higher annealing temperatures not only increased QD size but also improved crystallinity and reduced interface defect density between PbSe-QDs and CdS, significantly enhancing device performance [163].

Chapter 2 Experimental Methods

I. Introduction

Advancing mid-wave infrared (MWIR) PbSe-based optoelectronics requires a multidisciplinary toolkit that spans thin-film growth, materials analysis, and device fabrication. This chapter surveys the key equipment and procedures that underpin those activities, framing each technique in terms of the fundamental principles most relevant to the research presented in our work. Rather than reproducing the full theoretical formalisms or exhaustive derivations that govern every process, the discussion distills the concepts, operating modes, and practical considerations that enable reliable experimentation. Two physical-vapor deposition platforms—molecular beam epitaxy (MBE) and vapor-phase deposition (VPD)—anchor the section on thin-film growth. Their inclusion reflects both their central role in achieving the crystal quality, stoichiometric control, and interface engineering demanded by single-element lead-salt photodetectors operating near 4 μm, and their complementarity to more conventional sputtering or evaporation approaches used elsewhere in the field. Subsequent sections outline the characterization methods that translate raw films into quantified materials knowledge. Structural probes (e.g., X-ray diffraction, AFM), and optical and electronic spectroscopies (e.g., FTIR, photoluminescence, Hall, and time-resolved measurements) are introduced with schematic visual aids to clarify data-generation mechanisms and typical interpretation pathways. The presentation then follows the process flow from lithography and metallization through dicing, mounting, and wire-bonding. By integrating these growth, characterization, and fabrication perspectives, the chapter aims to furnish readers—and especially the next cohort of students at the University of Oklahoma—with a concise yet functional roadmap for developing thin-film lead-salt materials,

heterostructures, and MWIR devices. The intent is to lower the activation barrier for future investigations, accelerate iterative design cycles, and ultimately catalyze further contributions to the OU Electrical and Computer Engineering program.

II. Molecular Beam Epitaxy

Introduction to MBE System

MBE is an ultra-high-vacuum (UHV) deposition technique that delivers atomic-scale control over flux, stoichiometry, and interface abruptness—capabilities that are essential for engineering single-element lead-salt photodetectors operating in the mid-wave infrared MWIR. By supplying thermally evaporated elemental beams into a background pressure below 1×10^{-9} Torr, MBE enables in-situ monitoring of surface reconstructions, adatom nucleation kinetics, and layer-by-layer growth through reflection high-energy electron diffraction (RHEED) and quartz-crystal microbalance (QCM) feedback. Such precision has moved the technique beyond its traditional role in basic research; commercial foundries now employ MBE for infrared focal-plane arrays, III–V lasers, and quantum cascade structures whose compositional accuracy is unattainable with sputtering or metal-organic chemical vapor deposition (MOCVD).

The custom IV–VI MBE platform used in our laboratory (Figure 2-1) consists of two UHV chambers joined by a buffer module and serviced by an independent load-lock. The primary growth chamber houses seven effusion cells—dedicated to n-type and p-type PbSe, Se, CdSe, PbI_2, SnSe, and Bi_2Se_3—and an electron cyclotron-resonance (ECR) oxygen plasma source for controlled oxidation studies. A secondary chamber is optimized for substrate thermal desorption and for depositing CaF_2 buffer layers that mitigate lattice mismatch on silicon wafers. This dual-chamber architecture is critical for IV–VI growth: volatile species such as Se can readily

back-stream and poison neighboring sources, whereas segregating CaF_2 growth averts cross-contamination without breaking vacuum.

Despite the system's versatility, prolonged operation revealed a damaged knife-edge on the beam-flux housing that compromised base pressure and shutter integrity. Consequently, all PbSe and PbSe/CdSe heterostructures reported after the second year of our Ph.D. work were synthesized in a mini-MBE vapor-phase-deposition (VPD) system. Although the VPD chamber lacks the full effusion-cell complement, its smaller volume and simplified pumping architecture restored UHV conditions ($<5 \times 10^{-5}$ Pa) and ensured reproducible flux stability for subsequent experiments. The transition underscores the contingency planning required for complex vacuum hardware and highlights the modular approach adopted throughout this dissertation: whenever hardware constraints arise, growth protocols are migrated to alternate platforms while preserving the stringent interface and stoichiometric control demanded by MWIR device fabrication.



Figure 2-1. Custom two chamber MBE for IV-VI deposition at OU.

Molecular Flux

Unlike precursor-driven chemical-vapor-deposition (CVD) methods, molecular-beam epitaxy operates through a solid-vapor-solid pathway in which the only species introduced to the

chamber are those intentionally incorporated into the crystalline film. Elemental or compound source materials are thermally evaporated from effusion cells under ultra-high-vacuum conditions, forming low-energy molecular beams that impinge directly onto a heated substrate. Aside from auxiliaries such as a selenium cracker used prior to co-deposition, MBE growth therefore avoids parasitic gas-phase reactions and permits atomically abrupt doping and heterointerface control that are difficult to achieve with metal-organic or halide chemistries.

Because adatoms arrive in an essentially collision-free environment, film stoichiometry is dictated by the ratio of molecular fluxes rather than by complex gas-phase kinetics. A classic illustration is GaAs, where the arsenic vapor pressure far exceeds that of gallium; achieving a stoichiometric film typically requires an As:Ga beam-equivalent-pressure ratio well above 5 : 1. Under these conditions the growth rate becomes limited by the arrival rate of gallium adatoms, while excess arsenic re-evaporates. Although only a fraction of the impinging species are ultimately incorporated, every evaporated atom interacts with the surface—adsorbing, migrating, desorbing, or nucleating—so systematic variation of source temperatures, substrate temperature, and background pressure provides researchers with a finely tunable parameter space for optimizing film quality.

Figure 2-2 schematically depicts an effusion cell: the solid source rests in an ultra-pure graphite or pyrolytic-boron-nitride crucible surrounded by a resistive heater.

Precise temperature control (to ±0.1 °C) determines the vapor pressure and thus the molecular flux. For compound semiconductors this first control point is already non-trivial: heating a PbSe charge, for example, can yield a beam composed of Pb, Se, PbSe, Se_2, Pb_2Se_3, and related species. Preferential evaporation of selenium drives the remaining melt progressively

Pb-rich, which in turn promotes Pb droplet formation on the growing film and introduces Se vacancies—both deleterious to carrier transport.

To circumvent these issues, our PbSe layers are grown by co-evaporating a stoichiometric PbSe source and an independent Se cell. The additional selenium flux compensates for Se-rich species lost to re-evaporation, maintains near-ideal Pb : Se incorporation, and suppresses metallic lead agglomeration. This co-flux strategy exemplifies the central theme of MBE process engineering: by isolating each elemental supply and manipulating its flux in real time, one can tailor defect chemistry, interface abruptness, and film morphology with a level of precision unmatched by any other thin-film deposition technique.

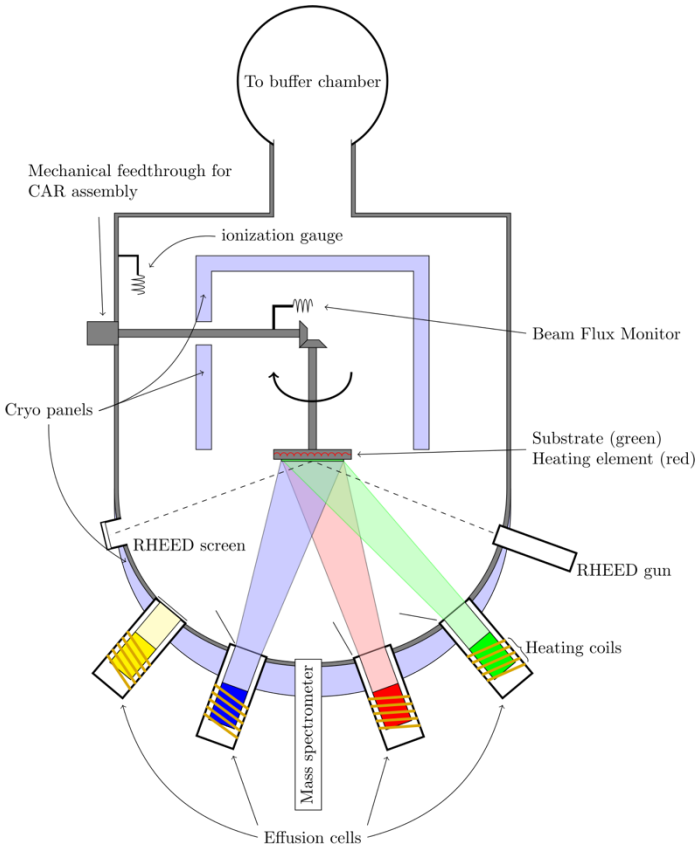


Figure 2-2 A schematic diagram of MBE with 4 effusion cells. Reprinted from [164].

Ultra-High Vacuum Pumps

Maintaining the ultra-high-vacuum (UHV) environment required for molecular-beam epitaxy hinges on a sequential, three-stage pumping architecture that incrementally reduces the chamber pressure from atmosphere to the 10^{-10} Torr regime. The rough-pumping stage employs an Edwards XDS 35i dry scroll pump, selected for its hydrocarbon-free compression and rapid throughput, to evacuate the load-lock and growth chambers from ambient pressure to approximately 10^{-3} Torr. Once this threshold is reached, the system transitions to high-vacuum pumping: a magnetically levitated Shimadzu turbomolecular pump, backed by the scroll pump, drives the pressure down a further four orders of magnitude to the 10^{-7} Torr range. The absence of mechanical bearings in the mag-lev design minimizes particulate generation and vibration, both of which are critical for preserving effusion-cell alignment and RHEED beam stability during subsequent bakeouts.

To achieve and sustain true UHV conditions, the final stage relies on a 400 L s^{-1} Gamma Vacuum Titan ion pump directly flanged to the growth chamber. Operating by ionizing residual gas molecules and burying them in titanium cathodes, the ion pump excels at removing chemically active species that would otherwise compromise chalcogenide film stoichiometry. Under steady-state operation the base pressure routinely falls below 1×10^{-10} Torr, affording mean free paths well in excess of the source-to-substrate distance and ensuring ballistic transport of molecular beams.

Initial pump-downs from atmosphere necessitate aggressive chamber degassing to eliminate adsorbed moisture and volatile organics. The entire vacuum envelope is wrapped with heating trapps and over-layered with aluminum foil to homogenize the thermal profile and mitigate differential expansion at welded joints or view-ports. Bakeouts are conducted at 150–170 °C for

24-to-72 hours, during which the combined action of elevated temperature and continuous pumping accelerates desorption kinetics by several orders of magnitude. This protocol not only expedites the attainment of UHV but also stabilizes the base pressure between growth campaigns, thereby minimizing flux drift and extending effusion-cell lifetime throughout the experimental program documented in this dissertation.

Reflection High Energy Electron Diffraction (RHEED)

Real-time reflection high-energy electron diffraction RHEED provides the most immediate feedback on crystalline quality during molecular-beam epitaxy in this dissertation. A 14 kV electron beam enters the growth chamber at a glancing incidence of $< 10°$, strikes the film surface, and diffracts into a pattern recorded on a phosphor screen. Because the electrons travel almost parallel to the substrate, the diffraction condition is governed by the intersection of surface-sensitive reciprocal-lattice rods with the Ewald sphere (radius = $1 / \lambda$). Rods that intersect the sphere and satisfy Bragg's law scatter strongly, generating the streaks or spots that make up a RHEED image. Consequently, every frame captured on the screen is a two-dimensional map of the topmost atomic layers, revealing surface reconstructions, in-plane lattice spacing, crystal orientation, and even monolayer-scale roughness (Figure 2-3).

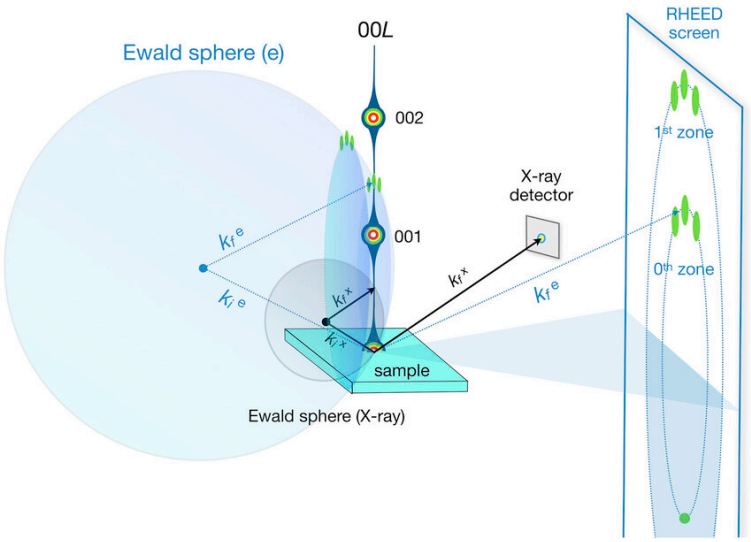


Figure 2-3. RHEED Image Formation. Reprinted from [165].

Monitoring the temporal evolution of these patterns establishes a closed feedback loop for growth optimization. Sharp, continuous streaks correspond to atomically flat terraces and two-dimensional, Frank–van der Merwe (layer-by-layer) growth. By contrast, spotty or ring-like patterns signify three-dimensional Volmer–Weber islanding, while mixed streak-plus-spot motifs mark the Stranski–Krastanov transition from nucleation-limited islands to smoother overgrowth.

III. Microscopy

Introduction to Microscopy

Correlating growth conditions with device performance requires a direct, nanoscale view of the materials we fabricate. Microscopy—specifically electron microscopy (EM) and scanning-probe microscopy (SPM)—provides that view by translating surface topography, crystal structure, and compositional variations into quantitative, image-based data sets.

Electron microscopy (SEM and TEM) exploits the wave nature of high-energy electrons: a 10 kV beam has a de Broglie wavelength orders of magnitude smaller than visible or even ultraviolet light, enabling sub-nanometer spatial resolution. Magnetic lenses, rather than refractive optics, focus the beam, while a high-vacuum column suppresses scattering and prevents

electrostatic charging of dust or residual gases. Secondary-electron and back-scattered-electron contrasts reveal surface roughness, grain size, and orientation distributions, whereas bright-field, dark-field, and high-resolution TEM images expose lattice defects, interfaces, and heterostructure abruptness across individual atomic planes.

Scanning-probe microscopy (exemplified by atomic-force microscopy) approaches the sample from the opposite angle—literally. A nanometer-sharp tip raster-scans the surface, and deflections caused by tip-sample forces are converted into a three-dimensional height map. Because AFM monitors mechanical interactions rather than scattered photons or electrons, it bypasses diffraction limits and operates under ambient, liquid, or controlled-gas environments without the vacuum constraints of EM. Various AFM modes—tapping, contact, phase, and conductive—extend its reach to mechanical modulus mapping, adhesion quantification, and spatially resolved electronic transport.

Together, EM and SPM furnish complementary insights: EM links crystal quality to processing history, while AFM quantifies surface roughness and local electronic behavior that directly influence carrier mobility and noise in MWIR PbSe detectors. The following section details the instrumentation, operating modes, and data-analysis protocols used throughout this dissertation to translate raw micrographs into the material parameters that guide our growth and device-fabrication strategies.

Scanning Electron Microscopy

Scanning electron microscopy is the primary electron-beam technique used in this dissertation to visualize PbSe thin films at nanometer length scales. A finely focused, high-energy electron probe (typically 1–10 kV) grazes across a pre-selected area, and the resulting electron–sample interactions generate signals that are converted into grayscale contrast. The spatial

resolution—well below that of optical microscopy—derives from the sub-angstrom de Broglie wavelength of the incident electrons, while high-vacuum operation (<10^{-5} Torr) prevents beam scattering and surface charging by airborne contaminants.

Inelastic collisions between the primary beam and the uppermost 5–10 nm of the sample eject low-energy (≈ 30–70 eV) secondary electrons (SE). An Everhart-Thornley detector biased positively collects these electrons and translates their local yield into image intensity. Because SE yield is highly sensitive to surface curvature and edge effects, SE mode excels at revealing topography: grain-boundary ridges, voids, and surface roughness are all rendered with sub-10 nm clarity (Figure 2-4).

Elastic scattering events return a fraction of the primary electrons to the surface with much higher energies. A segmented solid-state BSE detector positioned above the sample records these electrons, producing contrast that scales with the local atomic number (Z).

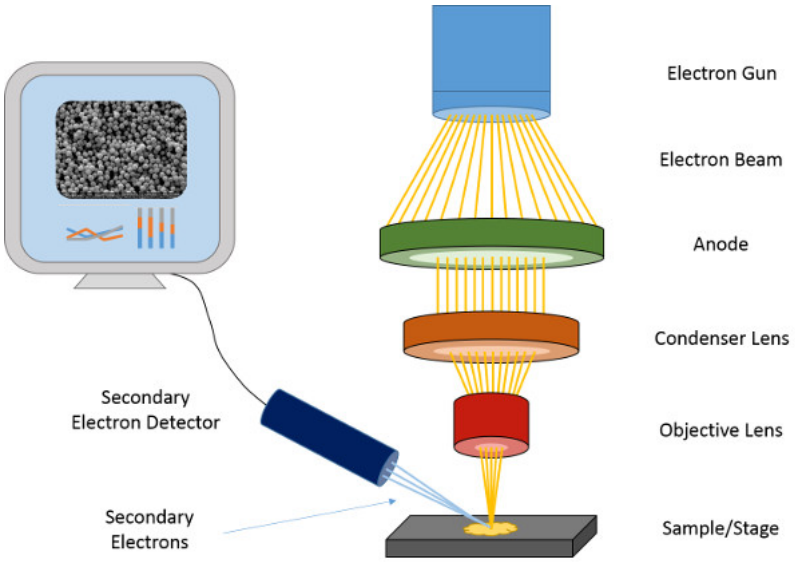


Figure 2-4 Schematic of scanning electron microscopy. Reprinted from [166].

Atomic Force Microscopy

Atomic-force microscopy extends the scanning-probe family by translating nanoscale tip–surface interactions into quantitative three-dimensional maps of thin-film topography and related properties. In our measurements a silicon cantilever, terminated by a sub-10 nm radius tip, raster-scans the PbSe surface while a laser–photodiode system records its deflection. Two principal operating modes are relevant:

The tip remains in continuous contact with the sample in contact AFM (c-AFM), and a feedback loop adjusts the vertical piezo stage to maintain a constant normal force. The z-motion required to uphold that force recreates the surface profile, yielding sub-nanometer height resolution and enabling roughness metrics such as R_q and R_a. Because lateral tip–sample interaction can distort soft chalcogenide films, c-AFM is reserved for robust substrates or for simultaneous current mapping when conductive coatings are present.

In non-contact AFM (nc-AFM) (Figure 2-5) the cantilever oscillates at, or slightly below, its resonant frequency (≈ 100–300 kHz) while hovering a few angstroms to nanometers above the surface. Attractive van-der-Waals forces dampen the oscillation amplitude; the control electronics restore the set-point amplitude by adjusting the tip–sample separation, thereby tracing the surface without mechanical deformation. This mode is deployed in dissertation to preserve as-grown PbSe morphology and to capture terrace structure, grain-boundary topography, and local roughness.

Coupled with SEM, AFM completes the morphological dataset: SEM provides rapid, wide-area context; and nc-AFM quantifies the angstrom-level roughness that governs interface recombination and dark current in MWIR lead-salt photodetectors.

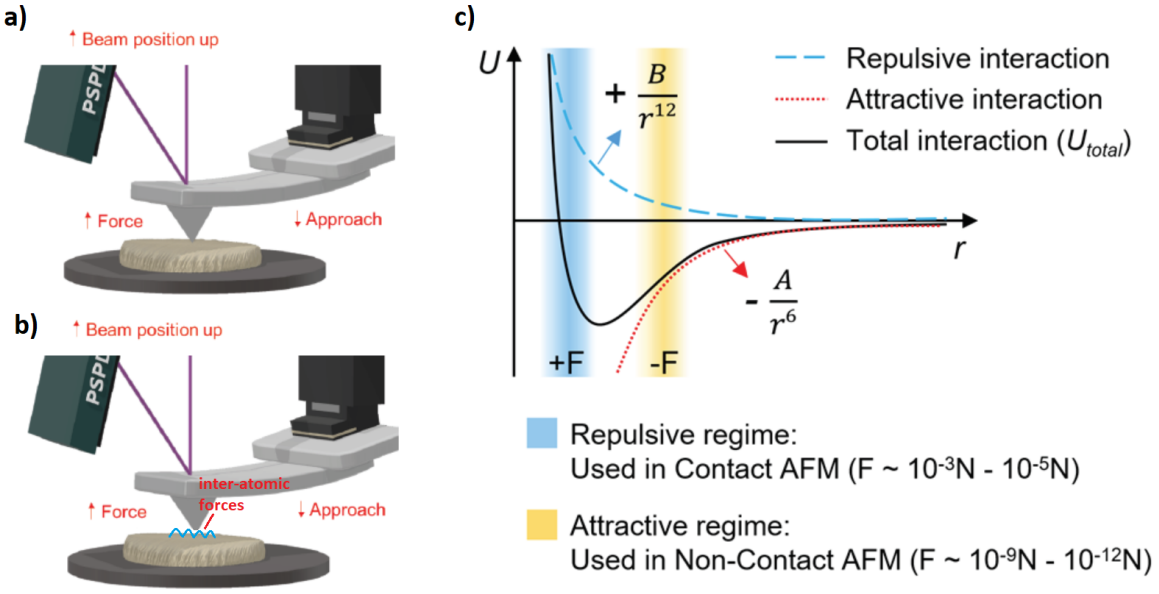


Figure 2-5 AFM Operation Modes: a) c-mode AFM, b) nc-mode AFM, and c) inter-atomic force regimes respective to sample-cantilever separation distance [167].

IV. X-Ray Diffraction

X-ray diffraction is the workhorse crystallographic probe in this dissertation because it demands virtually no sample preparation yet returns a wealth of structural information—lattice parameters, preferred orientation, micro-strain, defect density, alloy composition, and even vicinal tilt. In a typical lab system, a high-energy electron beam strikes a copper anode, generating characteristic Cu Kα radiation ($\lambda = 1.5406$ Å). A monochromator and collimator stack purify and shape this beam before it impinges on the film at a controllable incident angle; a scintillation or pixel-array detector then records the diffracted intensity as the source–sample–detector geometry is swept.

The key interaction is elastic scattering from the periodic atomic planes of the crystal lattice. When the path-length difference between reflected waves satisfies Bragg's law ($n\lambda = 2d \sin\theta$), constructive interference produces a diffraction peak. For poly-PbSe films,

multiple (hkl) planes meet this condition at distinct 2θ angles, so a conventional θ–2θ scan yields a fingerprint of phase purity and grain texture. Peak positions reveal out-of-plane lattice constants; full-width-at-half-maximum (FWHM) values quantify mosaic spread and strain; and integrated intensities gauge relative orientation fractions. Reality, of course, diverges from this ideal. The crystal departs from perfection: point defects, dislocations, micro-strain, and grain-boundary tilt all perturb the periodic spacing d and force Bragg's condition to be met over a finite angular range. Because modern optics suppress most instrumental broadening, the measured full width at half maximum of a diffraction peak now serves as a sensitive fingerprint of crystalline quality.

Because these metrics are derived from the same Cu Kα wavelength used worldwide, data sets acquired here can be compared directly with literature values and with complementary techniques, AFM for surface relief linked to strain relaxation, and SEM for correlating grain size with peak broadening. Throughout the ensuing chapters, XRD thus serves as the quantitative backbone for evaluating how MBE and VPD growth parameters translate into crystalline quality and, ultimately, MWIR detector performance.

V. Photoluminescence spectroscopy

Photoluminescence spectroscopy complements the electrical and radiometric tests by probing the radiative recombination pathways that ultimately limit detector quantum efficiency. Emission spectra were acquired on a Bruker Invenio-R Fourier-transform infrared spectrometer configured for mid-infrared operation at a spectral resolution of 16 cm^{-1}. An InSb high-gain detector, immersion-cooled in liquid nitrogen, provided the necessary sensitivity in the 2–5 μm band and held its dark-current floor low enough to resolve sub-picowatt signals. Because PbSe films emit only weakly at room temperature, the FTIR's internal photoluminescence (PL) accessory was routed through an external Stanford Research Systems SR830 lock-in amplifier.

Lock-in detection referenced to the excitation source suppresses the broadband thermal background that would otherwise swamp the MWIR emission and raises the signal-to-noise ratio by more than an order of magnitude.

Excitation was supplied by a diode-pumped solid-state laser at 980 nm operating in quasi-continuous mode: 1 ms pulses at 700 Hz with a 70 % duty cycle. The wavelength sits well above the PbSe band gap, ensuring efficient carrier generation while avoiding excessive free-carrier absorption that can complicate interpretation of the emission tail.

Each scan accumulated 256 interferograms to average out pulse-to-pulse fluctuations; the resulting spectra were phase-correlated by the SR830 at the 700 Hz chopping frequency and exported to OPUS for analysis. Peak wavelength and full width at half maximum served as proxies for band-gap energy and compositional uniformity, while integrated intensity normalized to pump power tracked relative quantum efficiency across growth recipes. By comparing these PL metrics with Hall mobility and detectivity data, the study establishes direct links between microscopic radiative processes and macroscopic detector performance, completing the multidimensional characterization framework for the PbSe MWIR devices presented in this dissertation.

VI. Device Fabrication

Introduction to Photolithography

Photolithography bridges the gap between film growth and electrical testing by translating a continuous semiconductor layer into a fully patterned device structure. The process begins with spin-coating a thin film of photoresist, a light-sensitive polymer whose solubility changes when it is exposed to ultraviolet radiation. A chrome-on-glass mask defines where that radiation reaches the resist: transparent windows admit light and induce a chemical transformation, whereas opaque

regions shield selected areas. After exposure and development, the wafer carries a sharply defined resist pattern that serves as a temporary stencil.

Depending on the subsequent step, that stencil can play one of two roles. In an etch sequence the resist protects underlying regions while reactive ions or wet chemicals remove the exposed film, sculpting mesas, pixels, or access vias with micrometer accuracy. In a lift-off sequence metal, dielectric, or passivation layers are deposited across the entire surface; when the resist is finally lifts-off, the overlying material stays, where there was no photoresist.

Mask Design and Photoresist

Photoresist chemistry lies at the heart of successful pattern transfer, and its behavior under ultraviolet exposure dictates both the image polarity and the final side-wall profile. A positive resist such as AZ 5214 E becomes more soluble in the developer wherever it is illuminated, so the pattern that remains on the wafer reproduces the mask openings. A negative resist like AZ nLof 2020 behaves in the opposite manner: light exposure cross-links the polymer, making the irradiated zones insoluble and leaving an inverted replica of the mask after development. Negative resists develop with a slight under-cut that act as a built-in shadow mask, allowing metal or dielectric films deposited afterward to break cleanly at the resist boundary; the lift-off step therefore proceeds without the bridging or encapsulation problems that often plague positive-resist processes. Positive resists, by contrast, yield nearly vertical side walls that are preferable when the patterned resist must withstand aggressive etch.

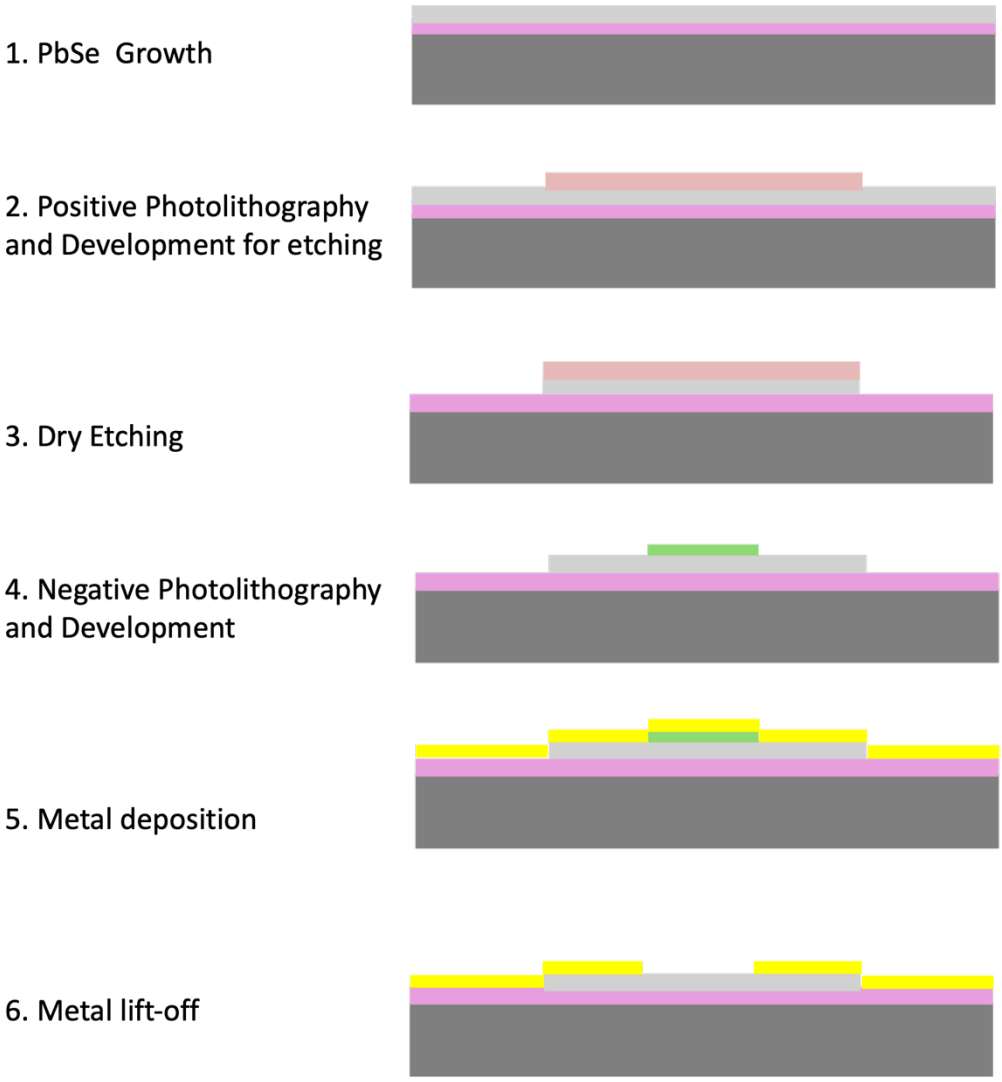


Figure 2-6. Fabrication Steps for Photoconductor Device

Because the polarity determines how every subsequent layer aligns, mask layout must be planned with the full lithographic sequence in mind. Figure 2-6 depicts schematic fabrication process for photoconductor device. Each device in this dissertation was drafted in K-Layout and Layout Editor, incorporating alignment keys that repeat at every level so that successive patterns register to within a micron across the entire wafer. The finished designs were written onto chrome-quartz plates with a Heidelberg uPG-101 laser writer. Before coating, wafers were solvent-cleaned, rinsed, and prebaked at 95 °C for at least five minutes to expel

moisture. Spin-coating followed: positive resist at 4000 rpm with a 95 °C soft-bake for one-minute, negative resist at the same speed but with a 110 °C soft-bake to drive off residual solvent. After mask alignment the positive resist received a four to ten-second exposure (Figure 2-7), whereas the negative resist required one-minute post-exposure bake at 110 °C to complete cross-linking.

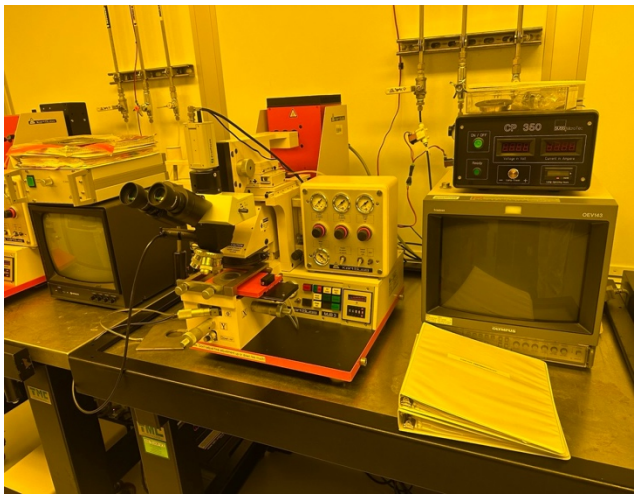


Figure 2-7. Mask Aligner Used to Expose the Pattern

Development proceeded for 30–60 seconds in AZ 300-MIF or AZ 726-MIF, respectively, and every wafer was inspected under a Normarski interference-contrast microscope (Figure 2-8) to verify pattern integrity before moving on to etching, deposition, or lift-off. By matching resist tone and side-wall profile to the demands of each fabrication step, the lithographic flow produced clean mesas, well-isolated metal contacts, and precisely aligned multilayer structures essential for reproducible PbSe detector performance.

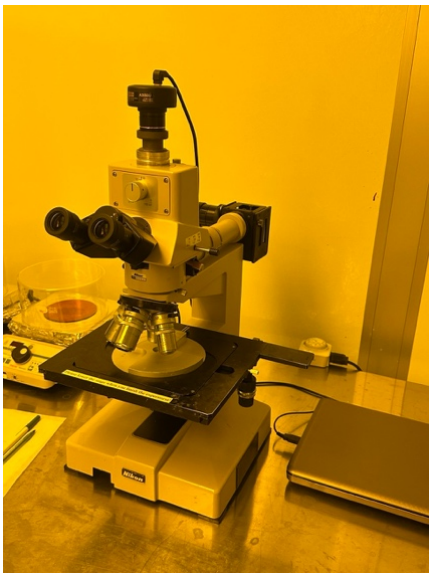


Figure 2-8. Normarski interference-contrast microscope

Reactive Ion Etching

Reactive ion etching completes the pattern-transfer sequence by sculpting the exposed PbSe into well-defined mesas without attacking the surrounding photoresist stencil. Dry etching was carried out in a Trion Technology MiniLock II reactor (Figure 2-9), whose inductively coupled plasma delivers high ion density while the capacitive bias at the chuck accelerates ions normal to the wafer surface, ensuring vertical side walls. For the chalcogenide chemistry used here, a mixed $Ar/CH_4/H_2$ plasma was chosen at a flow-rate ratio of 5 : 10 : 10 SCCM. Argon provides physical sputtering to initiate surface activation, methane contributes reactive carbon radicals that form volatile Pb- and Se-containing organometallics, and hydrogen assists in breaking Pb–Se bonds, together producing a synergistic etch that is faster and cleaner than any single-gas recipe.

Typical process conditions were 150 W RF power and 35 mTorr chamber pressure. Under these settings the etch rate averaged 50 nm min^{-1}. The low operating pressure suppressed side-wall scattering, while the hydrogen fraction reduced polymer deposition that otherwise roughens the etched profile. This RIE step thus produces the clean, high-aspect-ratio geometries required for

isolating individual detector pixels and for maintaining uniform current flow across the active area of the MWIR PbSe devices.



Figure 2-9 Trion Technology MiniLock II reactor

Metallization via thermal evaporation

Metallization of the patterned PbSe detectors was carried out in a Kurt J. Lesker Nano 36 thermal evaporator (Figure 2-10), a compact system equipped with dual resistive sources, a motorized shutter, and a quartz-crystal microbalance for closed-loop rate control. After lithographic definition, samples were loaded through the Nano 36 load-lock and pumped to a base pressure below 9×10^{-6} Torr, a level low enough to suppress oxide formation on the chalcogenide surface before metal arrival. Gold's high work function and chemical inertness yield a low-resistance ohmic interface to p-type PbSe while preserving surface stoichiometry.

To save cost and have good ohmic contact with CdSe, Indium was evaporated at 1.5 Å s^{-1} to a thickness of 400 nm. Throughout both depositions the planetary rotation stage maintained uniform thickness, and the negative-resist under-cut produced earlier in the lithography step

guaranteed a clean lift-off: immersion in warm acetone for ten minutes released the unwanted metal over the resist without tearing the fine-line features anchored to the wafer. Post-lift-off inspection by SEM confirmed sharply delineated edges and step-free coverage over the etched mesas, completing the contact fabrication sequence and readying the devices for electrical probing and mid-wave infrared responsivity measurements.

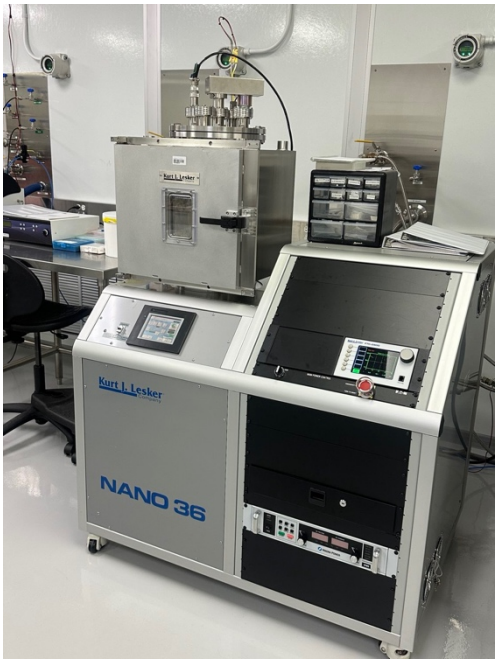


Figure 2-10 Kurt J. Lesker Nano 36 thermal evaporator

VII. Electrical measurement

Electrical characterization links the structural quality of the PbSe films to their optoelectronic performance. Current–voltage (I–V) data were collected with a Keithley 2400 SourceMeter configured for automatic source-sweep and measure mode. Each sample was contacted in a shielded probe station; for photovoltaic (PV) devices both bias polarities were scanned from –0.5 V to +0.5 V in 2 mV increments, whereas photoconductor were swept across a

broader –1 V to +1 V range. The Keithley's embedded buffer stored the full I–V trace and transferred it via GPIB to a dedicated computer, where custom MATLAB scripts converted the raw current into current density by normalizing to the mesa area measured previously by optical profilometry.

Subsequent analysis extracted the key diode and detector figures of merit. The zero-bias dynamic resistance–area product (R_0A) was obtained from the inverse slope at $V = 0$ V; the parallel-plate model then yielded the shunt resistance R_sh. A high-bias linear fit isolated the series resistance R_s, while the semi-log forward-bias region was fitted to the Shockley equation to determine the ideality factor n. For photoconductive devices the dark current density J_dark at the intended operating field furnished a baseline for noise calculations and detectivity estimates presented in Chapter 1.

Free-carrier properties were measured independently with a four-probe Hall technique on unpatterned films using an Ecopia HEM-2000 Hall Measurement System. Van der Pauw geometries were cleaved to 8 mm × 8 mm squares, indium contacts were ultrasonically soldered at the corners, and the samples were loaded into the HEM-2000's 0.55 T electromagnet stage. The instrument alternated current direction and magnetic-field polarity to cancel thermoelectric and offset voltages, yielding sheet resistance, carrier concentration, and Hall mobility. These room-temperature mobility and carrier-density values complete the electrical dataset, enabling correlation of growth parameters with charge-transport mechanisms.

VIII. Radiometric measurement

Optical testing closes the loop between growth, device processing, and ultimate detector performance by converting the mid-wave infrared (MWIR) flux of a calibrated source into electrical figures of merit. Illumination is provided by an Infrared Systems Development Corp.

collimated black-body that operates at 823 K, a temperature chosen because Planck's law places its spectral peak squarely inside the 3–5 μm atmospheric window that our PbSe devices target. A Thorlabs MC1F10 mechanical chopper modulates the beam at 750 Hz, producing a reference wave that the subsequent electronics can lock onto.

During the measurement each pixel is biased sequentially through the Keithley 2400, as described in the previous section. The photocurrent passes through a voltage divider that contains a load resistor matched to the nominal dark resistance of the device, converting the current into a small-signal voltage that is fed into the differential input of a Stanford Research Systems SR830 digital lock-in amplifier. The SR830 references the 750 Hz chopping frequency, averages over a 1 Hz detection bandwidth, and simultaneously outputs the in-phase signal amplitude and the root-mean-square noise voltage for every bias point. All measurements are performed at room temperature (298 K); the detector substrate sits on a temperature-stabilized stage to eliminate thermal drift that could masquerade as responsivity changes.

With the signal, noise, bias voltage, and the calibrated black-body flux in hand, standard radiometric parameters follow directly. Responsivity is obtained by dividing the lock-in voltage by the incident optical power, corrected for the black-body aperture and the detector area. The NEP is calculated by normalizing the measured noise to the responsivity, and the D* then emerges by scaling the NEP with the square root of the active area, removing size as a variable so that devices fabricated under different conditions can be compared on equal footing. In this way the radiometric experiment provides a quantitative bridge from growth chemistry and device architecture to functional metrics—responsivity, NEP, and D*—that define the competitiveness of the PbSe MWIR technology developed in this dissertation.

Chapter 3 Epitaxial PbSe/Ge and CdSe/PbSe Heterojunction Growth and MWIR Photovoltaic Detector [1]

I. Introduction

Lead selenide has a long history in MWIR optoelectronic development, with more recent attention focused on the fabrication of MWIR detectors pushing beyond the cryogenic barrier. A room-temperature high-detectivity D* MWIR PbSe PC has been demonstrated [168], [169], [170]. To date, low-cost PbSe MWIR photoconductors operating at uncooled or Thermoelectric (TE)-cooled temperatures remain the choice for many sensing and imaging applications [171]. Such high performance is attributed to its low Auger recombination rate at high temperatures. The Auger coefficient in IV-VI semiconductors such as PbSe is roughly an order of magnitude lower than those in Sb-based type-II QWs, which are in turn significantly suppressed relative to other III-V and II-VI semiconductors such as MCT with the same energy gaps [74], [75], [76], [77], [78], [79], [80]. Although very promising performance has been demonstrated by polycrystalline PbSe PC FPA, several problems are still associated with their design, including film inhomogeneity, large

[1] This chapter has two sections and based on two published papers.

The first section is based on: LL McDowell, J Qiu, **M. Rastkar Mirzaei**, B Weng, Z Shi, "Integration of Epitaxial IV–VI Pb-Chalcogenide on Group IV Vicinal Ge Substrate to Form p–n Heterogeneous Structures", Crystal Growth & Design, 2021

M. Rastkar Mirzaei author contribution: M. Rastkar Mirzaei made supporting contributions to the semiconductor growth process, manuscript editing, and material characterization, and played a lead role in device testing.

The second section is based on: L. L. McDowell, **M. Rastkar Mirzaei**, and Z. Shi, "Epitaxial CdSe/PbSe Heterojunction Growth and MWIR Photovoltaic Detector," Materials, vol. 16, no. 5, p. 1866, Feb. 2023, doi: 10.3390/ma16051866.

M. Rastkar Mirzaei author contribution: M. Rastkar Mirzaei contributed to the methodology (supporting), investigation (supporting), and data curation (lead). He also contributed to writing—original draft preparation (supporting), writing—review and editing (lead), and visualization (lead).

1/f noise and limited FPA resolution due to contact configuration for PC detectors [103], [172], [173], [174], [175], [176], [177]. Ideally, if one could develop PbSe photovoltaic detectors with the same performance as its PC counterpart, these problems could be solved. Due to fast dopant diffusion, it is hard to make an abrupt p-n homojunction. Therefore, the heterostructure p-n junction would be one potential option. The challenge for forming heterojunction is finding a substrate that PbSe can grow on, and at the same time making a viable type-II heterostructure. We proposed n-type PbSe/ p-type germanium type-II heterostructure [53], [178]. Although there is more than eight percent lattice mismatch between germanium and PbSe, single crystal PbSe were successfully grown on a surface-treated vicinal germanium substrate, resulting in an I-V curve with a very high rectification factor.

n-PbSe/p-Ge heterostructure

In this work we create a novel heterogeneous material structure by depositing MWIR absorbing monocrystalline n-PbSe film on p-Ge substrate, forming a p-n heterojunction with room temperature MWIR photovoltaic detector capabilities. Traditionally, materials such as PbSe and Ge have been found difficult, if not unsuitable for fabricating heterogeneous structures due to their large difference in lattice constant and thermal expansion coefficient. These dissimilar properties often give rise to strain-induced defects, ruining interface and bulk phenomena that researchers may hope to exploit with their material system. While IV-VI materials such as PbSe show promise in numerous MWIR optoelectronic and topological applications, the limitations of growing high-quality monocrystalline films on both low-cost and scalable substrates have been a major point of interest for researchers in recent years [179], [180], [181], [182], [183]. Due to both availability and scalability, IV-VI Pb-chalcogenide semiconductors such as PbSe are often grown on many dissimilar substrates inhibiting the formation of high-quality monocrystalline films. Further, while

most of the substrates being used for epitaxial growth such as BaF_2, CaF_2, KCl, and $SrTiO_3$ may provide beneficial mechanical, thermal, and optical properties, they are also electrically passive insulators in the heterostructure acting only as a platform to grow epitaxial films. Direct Growth of PbSe on an electrically active substrate could combine the merits of two materials and offer new device structures to advance state-of-the-art performance while reducing cost and increasing scalability [184]. Combining high-quality monocrystalline PbSe with relevant Si, Ge, or III-V material systems would improve a host of device applications including MWIR lasers, detectors, thermoelectric devices, and topological crystal insulators. However, the direct growth of high-quality PbSe films on electrically active substrates is exceedingly difficult due to the challenges discussed above. For example, direct growth on Si substrate without a CaF_2 buffer layer tends to form cracks or has inferior material quality [185]. More recently, efforts have been made to expand the list of suitable substrates for epitaxial growth of PbSe to include III-V materials such as GaAs, GaSb, and InSb [186], [187], [188]. While there has been promising success on these substrates, each material system comes with its own design hurdles, such as small critical thickness, high defect densities, or electrically inactive use of the substrate/ film interface. Additionally, growth of IV-VI/III-V heterostructures face challenges regarding growth orientation due to the nature of defect slip planes. IV-VI rock salt structure materials like PbSe have a primary slip system along {001}<1 -1 0> resulting in preferential dislocation gliding along the {001} plane. The result of which is that the slip system for accumulated dislocations in PbSe films grown in the (100) orientation feel no resolved shear stress from in-plain strain, locking dislocations in place. This handicap for PbSe films grown in the (100) orientation is often avoided by using (111) orientated substrates. However, demonstration of high-quality monocrystal PbSe films grown in the (100) direction would allow for the utilization of the more industry standard (100) substrates, improving

both production costs and scalability. For this reason, we chose to deposit PbSe films on Ge (100) substrates to take advantage of these attractive attributes. Conversely, epitaxial IV-VI films grown directly on CdTe substrates or composite CdTe/Si (211) substrates have been demonstrated, and mid-infrared detectors using PbTe/CdTe interface properties have also been reported [189], [190], [191]. However, there has been no report of devices that utilize the direct growth of thick monocrystalline PbSe film on electrically active substrates for device applications. Table 3-1 provides an extensive summary of PbSe growth's current progress on both similar and dissimilar substrates.

Table 3-1 List of relevant substrate electrical and optical properties compared with PbSe.

Material System	Substrate Treatment	Lattice Mismatch (Å)	Thermal Expansion Coef. Mismatch	Bandgap (eV)	Electron Affinity (eV)	Crystallinity
PbSe/CaF2 /Si	-	12.1% (6.126/5.464/5.43)	1.5% (19.4/19.1)	0.27/12/1.17	4.6/1/4.05	Single
PbSe/BaF2 [185]	-	1.19% (6.126/6.2)	2% (19.4/19.8)	0.27/9.1	4.6/2.1	Single
PbSe(111)/ Si(111) [185]	-	12.7% (6.126/5.431)	746% (19.4/2.6)	0.276/ 1.17	4.6/4.05	Poly
PbSe/KCl [192]		2.63% (6.126/6.292)	46% (19.4/36)	0.27/ 8.4	4.6/0.5	Single
PbSe(100) /GaAs(100) [193]	Te	8.3% (5.653/5.431)	338% (19.4/5.73)	0.27/ 1.41	4.21/4.07	Single
PbSe (511)/ GaAs(211) [193]	Te	4.1%	338% (19.4/5.73)	0.27/ 1.42	4.6/4.07	Single
PbSe(001)/ GaSb(001) [194]	-	0.5% (6.126/6.095)	250% (19.4/7.75)	0.276/ 0.726	4.6/4.06	Single
PbSe(001)/ InAs(001) [194]	PbSe	1.1% (6.126/6.058)	429% (19.4/4.52)	0.276/ 0.36	4.6/4.9	Single
PbSe(111)/ InAs(111)A [195]	PbSe	1.1% (6.126/6.058)	429% (19.4/4.52)	0.276/ 0.36	4.6/4.9	Single
PbSe/SrTi O3[196]		56.8% (6.126/3.905)	202% (19.4/9.6)	0.276/ 3.2	4.6/3.57	Topological Crystal Insulator
PbSe/Ge	Se	8.2% (6.126/5.658)	328% (19.4/5.9)	0.276/ 0.67	4.21/4	single

In addition to the interface and material quality, the band alignment of the heterojunction is exceedingly important for device applications. Figure 3-1 shows reported values of electron affinity (EA) and energy bandgap for PbSe and its most common substrate materials.

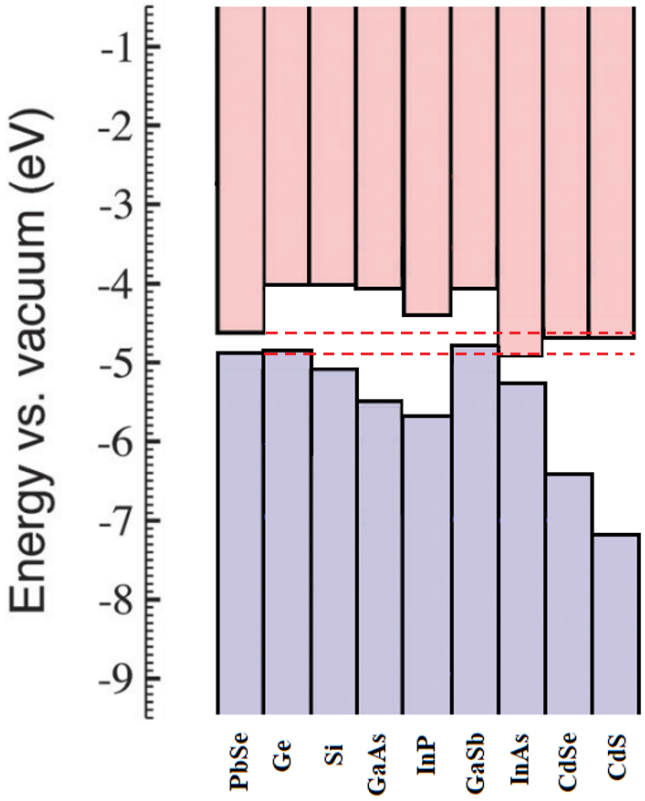


Figure 3-1 Conduction and valence band edge alignment for PbSe and other relevant material systems.

Based on the electron affinity values in Figure 3-1, PbSe forms a type-I band alignment with Si, GaAs, and InP, making them suitable for heterojunction light emitting devices, while the PbSe/InAs material system has a staggered type-III band alignment. Among the listed substrate materials, Ge forms a type-II heterojunction with PbSe while adding its own host of attractive attributes, making it a suitable candidate for p-n heterojunction photovoltaic device structures. To date, low-cost PbSe MWIR photoconductors operating at uncooled or Thermoelectric (TE)-cooled temperatures remain the choice for many sensing and imaging applications [171]. Polycrystalline PbSe MWIR photoconductors have reported D* values at room temperature of 2.8×10^{10} Jones and 4.2×10^{10} Jones at ~3.8 μm, without and with antireflective coating [168], [169], [170]. Such high performance is attributed to its low Auger recombination rate at high temperatures. Auger coefficient in IV-VI semiconductors such as PbSe is roughly an order of magnitude lower than

those in Sb-based type-II QWs, which are in turn significantly suppressed relative to other III-V and II-VI semiconductors such as MCT with the same energy gaps [74], [75], [76], [77], [78], [79], [80]. Although very promising performance has been demonstrated by polycrystalline PbSe photoconductor FPA, several problems are still associated with their design, including film inhomogeneity, large 1/f noise and limited FPA resolution due to contact configuration for PC detectors. Ideally, if one could develop PbSe photovoltaic detectors with the same performance as its PC counterpart, these problems could be solved. Previous efforts to make $Pb_{1-x}Sn_xSe$ PV detectors using epitaxial films on Si with Pb Schottky junction have made significant progress, but the performance is inferior to MCT detectors [195]. One key performance limiting factor is the difficulty to make a p-n junction detector that can outperform its Schottky counterpart. The problem is due to impurity diffusion at the p-n junction interface. To solve these problems and further improve the performance, heterojunction CdS/epi-PbSe on Si substrate detectors directly grown on conductive oxide/metal for monolithic integration with Si readout integrated circuit (ROIC) have been made [197], [198], [199]. However, the conduction band of CdS seems somewhat higher than that of PbSe which could block some of the photo-generated carriers. For IV-VI MWIR/LWIR semiconductors with bandgap energies of interest in the range of 0.1- 0.3 eV, it is very challenging to find proper materials to form heterojunction structures for photovoltaic detectors. The n-PbSe/p-Ge heterojunction has several unique advantages over the previous approaches. First, Ge serves not only as a substrate, but also as part of the heterojunction being a SWIR absorber and hole transport layer. Therefore, PbSe/Ge heterojunction monolithically integrates Ge and PbSe, naturally forming a dual-band MWIR/SWIR or PV detector. Second, the heterojunction could significantly reduce the dark current. Third, since Ge on Si substrate is commercially available, large-format PbSe/Ge/Si heterojunction detectors can be fabricated, as

well as monolithically integrated PbSe /Ge/Si FPA on Si ROIC. Figure 3-2 shows a schematic drawing of band alignment of PbSe and Ge, and carrier transport of PbSe/Ge heterojunction.

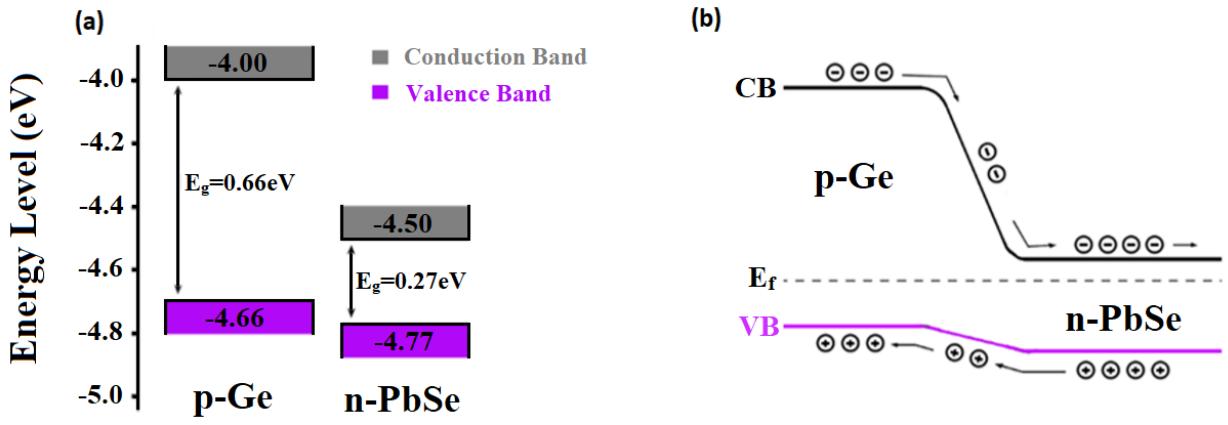


Figure 3-2 Schematic drawing of: (a) n-PbSe/p-Ge band alignment and (b)carrier transport in n-PbSe/p-Ge heterojunction structure.

In this work, we demonstrate a method for growing monocrystalline n-type PbSe on a p-type Ge substrate without the use of a thick buffer layer. The result of our efforts showcases both the ability to grow a thick monocrystalline film on a dissimilar substrate along with the formation of high-quality p-n heterojunction. The growth of monocrystalline PbSe on Ge has not been previously demonstrated, and the techniques employed here may allow for the introduction of other new combinations of materials to be explored.

II. Experimental Methods n-PbSe/p-Ge Heterostructure

The n-PbSe/p-Ge heterojunction was formed in a custom MBE system by direct evaporation of 99.9999% pure Se-rich PbSe in combination with a 99.999% pure Bi_2Se_3 as the n-type dopant. PbSe deposition was performed on a clean vicinal p-Ge substrate with carrier concentration of $1\times10^{17}cm^{-3}$ and surface orientation <100> with a 6° miscut towards <111> at a substrate temperature of 375˚C. A Bi_2Se_3 beam flux was maintained at 0.01% of the PbSe beam flux to achieve n-PbSe films with carrier concentrations of $8\times10^{17}cm^{-3}$. Before PbSe deposition,

Ge substrates were cleaned by chemical method then loaded into the MBE for thermal cleaning to encourage desorption of the surface oxide layer. Surface treatment of the germanium substrate was performed at 400˚C using a 99.999% Selenium before depositing PbSe films. In-situ RHEED analysis was performed using the KSA 400 data acquisition and analysis software. Cross-section and surface morphology were observed by SEM and AFM operating in non-contact mode. High-resolution XRD analyses were performed using a Rigaku Ultima IV diffractometer. Cu Kα radiation (40 kV, 44 mA) was used in parallel beam mode, and data analysis was completed using the MDI Jade2010 software with the ICDD (International Centre for Diffraction Data) PDF4+ database. Photoluminescence measurements were conducted in CW mode using a Bruker FTIR apparatus. Current-voltage analysis was performed using a Keithley 2400 Standard Series Source Measure Unit.

III. Results and Discussions - n-PbSe/p-Ge Heterostructure

Crystallography In-Situ RHEED Analysis

In-situ RHEED measurements were performed before, during, and after PbSe growth on germanium substrates. RHEED pattern changes were observed for both the Se surface treatment period as well as the nucleation stage and bulk growth portion of PbSe films. Transformation of the characteristic Ge RHEED lines were observed during the Se treatment period, with the disappearance of Ge reconstruction lines along with the formation of dots, indicating the presence of a new surface. This RHEED transformation could be caused by Ge-Se bonding that results in Se terminated surface, or formation of a very thin compound material such as GeSe, or $GeSe_2$. However, there is no noticeable change in the diffraction pattern and line spacing, indicating the surface layer maintains the same crystal structure and orientation as the germanium substrate. Immediately after opening the PbSe shutter, the RHEED pattern quickly changes back to lines

while decreasing in line spacing until stabilizing for the duration of the growth. Figure 3-3 shows the evolution of the RHEED pattern as the growth process develops.

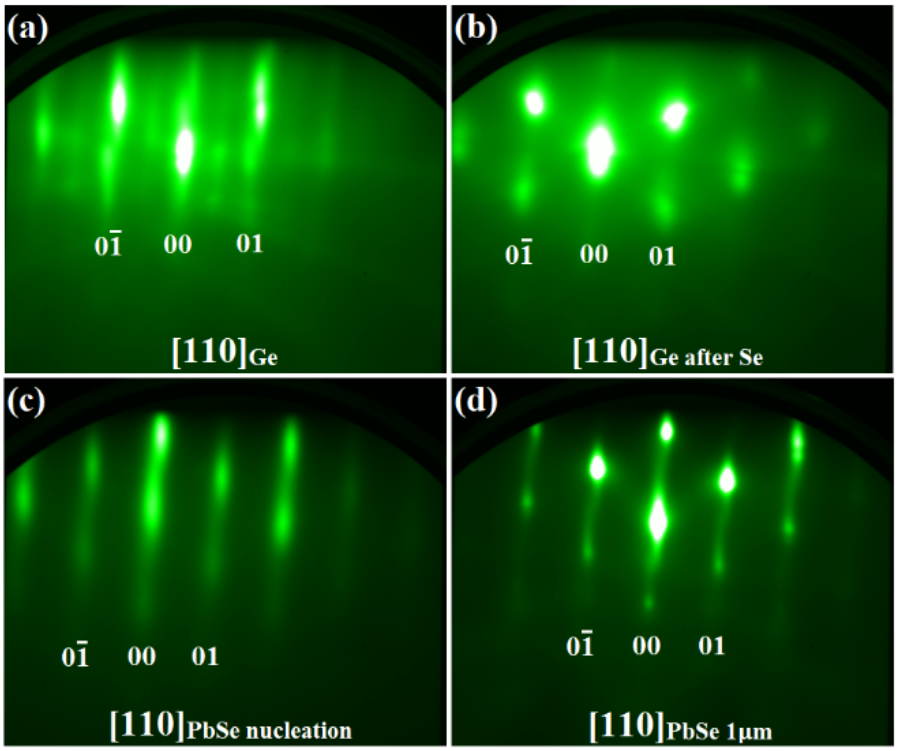


Figure 3-3 RHEED images of the: (a) cleaned vicinal germanium substrate with reconstruction, (b) substrate surface after Se treatment, (c) film surface during the first monolayers of PbSe growth (d) and the final 1µm thick PbSe film surface.

The initial RHEED pattern of the PbSe nucleation stage and thin bulk growth begins with a relatively diffuse line profile. As PbSe thickness increases, line intensity continues to increase along with decreasing line spacing and diffusivity. After roughly 11nm of PbSe deposition, RHEED line spacing stabilizes and remains unchanged for the duration of the growth. This phenomenon indicates the presence of a compressive lattice strain during the initial stages of PbSe growth, gradually relaxing with increasing film thickness until it reaches roughly 11nm. Further, the vicinal nature of the substrate can be observed in the RHEED line profile with the presence of a slight tilt and separation in the RHEED lines. Rotating the substrate 180˚ results in the same

observed RHEED pattern but tilted in the opposite direction. Post growth RHEED analysis reveals a strong monocrystalline PbSe (001) orientated surface with no signs of polycrystalline grains.

Microscopy

Scanning electron microscopy and atomic force microscopy were used to both visually observe and investigate cross-section and surface morphology for the n-PbSe/p-Ge crystal structure. The SEM cross-section observed in Figure 3-4 reveals the epitaxial nature of PbSe deposited on vicinal germanium substrate.

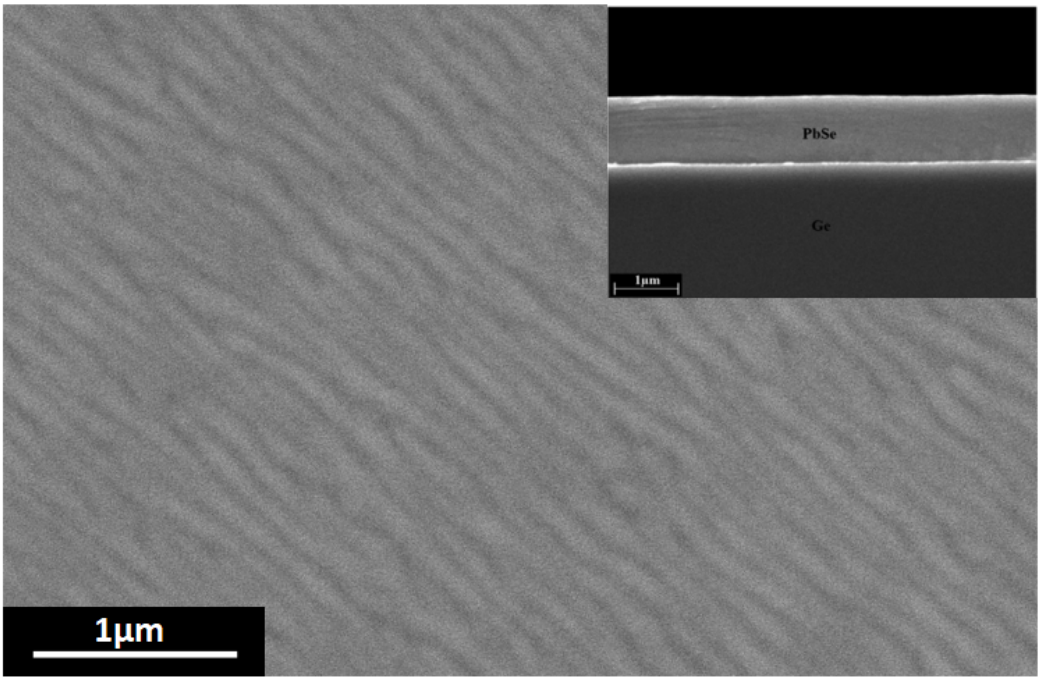


Figure 3-4 SEM image of PbSe on Ge: Surface image indicates a meandering growth mode of epitaxial PbSe films with no observable cracks over a large area, with the in-set cross-sectional image corroborating the RHEED observations of a bulk single crystalline PbSe film.

Within the resolution of the SEM, no indication of a sufficiently thick interface layer is present at the PbSe/Ge interface despite the Se surface treatment of the Ge substrate and resulting RHEED transformation. Glancing angle XRD, XPS, and Raman have been employed to further investigate on the Se treated germanium substrates without deposition of PbSe films, but there is

no indication of any new surface material. Future work aimed at investigating the presence of a possible interface layer between PbSe and germanium will involve cross-section transmission electron microscopy (TEM) in attempt to directly observe the bonding nature of this novel heterojunction interface.

PbSe surface morphology observed by AFM surface profile indicates a slight surface roughening due to the apparent step-meandering nature of the PbSe growth, along with observation of long-range order parallel peaks and valleys as seen in Figure 3-5 [200].

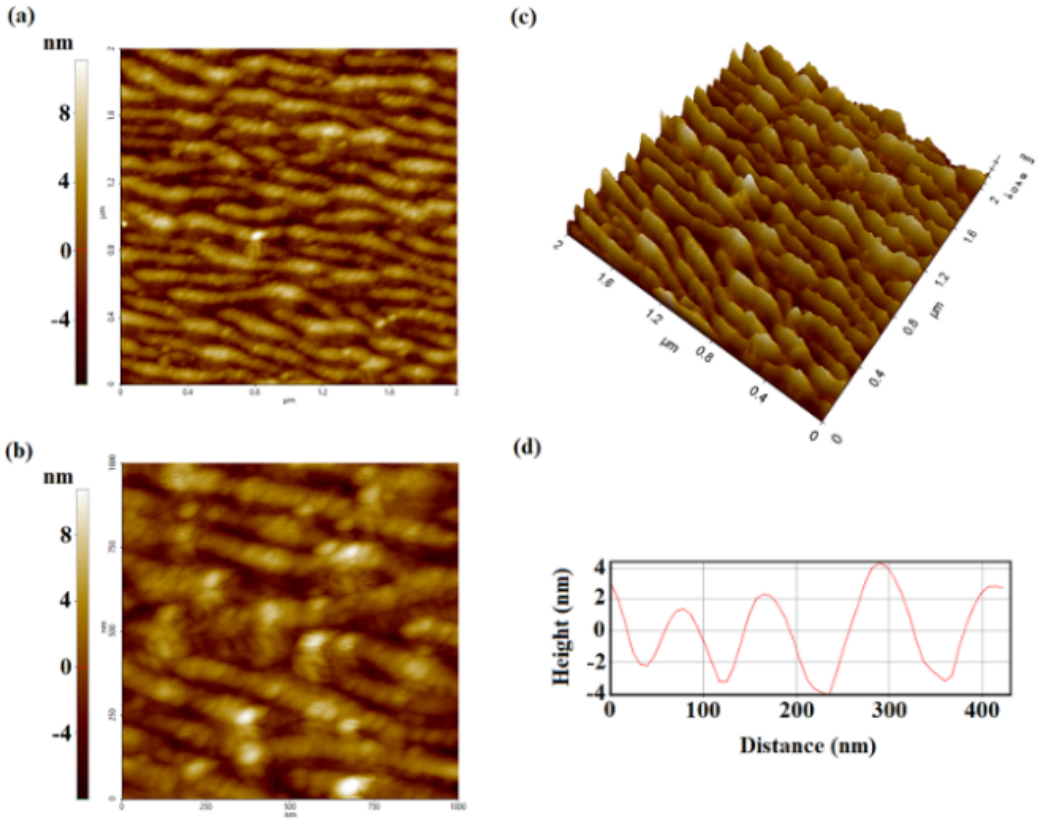


Figure 3-5 AFM image of step-meandering growth observed in PbSe films: (a) 2µm x 2µm NCM surface profile scan, (b) 1µm x 1µm NCM surface profile scan, (c) 3D surface view, and (d) height profile measurement.

The AFM surface profile in Figure 3-5 reveals a surface morphology dominated by parallel growth peaks, separated by thin valleys of shallow depth. With most of the surface area dominated by the atomically smooth growth peaks, the average surface roughness of 1.8nm is mostly due to

the thin valleys with an average depth of 5nm. However, with an average depth of only 5nm, coalescence of these growth areas is likely to occur in the bulk film resulting in a uniform monocrystalline bulk PbSe layer as observed in cross-sectional SEM. While the influence of growth temperature and deposition rate has been previously reported for films grown on vicinal substrates, for materials with dissimilar lattice constant and thermal expansion coefficient, the effectiveness of these parameters on enhancing epitaxial growth becomes drastically reduced [201]. In our case, the Se treatment period of the Ge substrate seems to play a critical role in lowering the interface energy of Pb adatoms on the growth surface, allowing for sufficient surface diffusion contributing to enhanced nucleation and subsequent layer-by-layer growth. Without this procedure, Pb and Se adatom interactions dominate over the Ge surface inducing three-dimensional adatom clusters, resulting in Volmer-Weber growth, leading to the formation of polycrystalline grains.

Photoluminescence and X-Ray Diffraction

XRD was used to identify characteristic PbSe peaks and verify the in-situ RHEED measurements which indicate the successful growth of monocrystalline PbSe on germanium. First, a wide-angle scan was performed to identify all possible contributing peaks, followed by ω-2θ XRD to investigate PbSe full-width half maximum (FWHM), as seen in Figure 3-6.

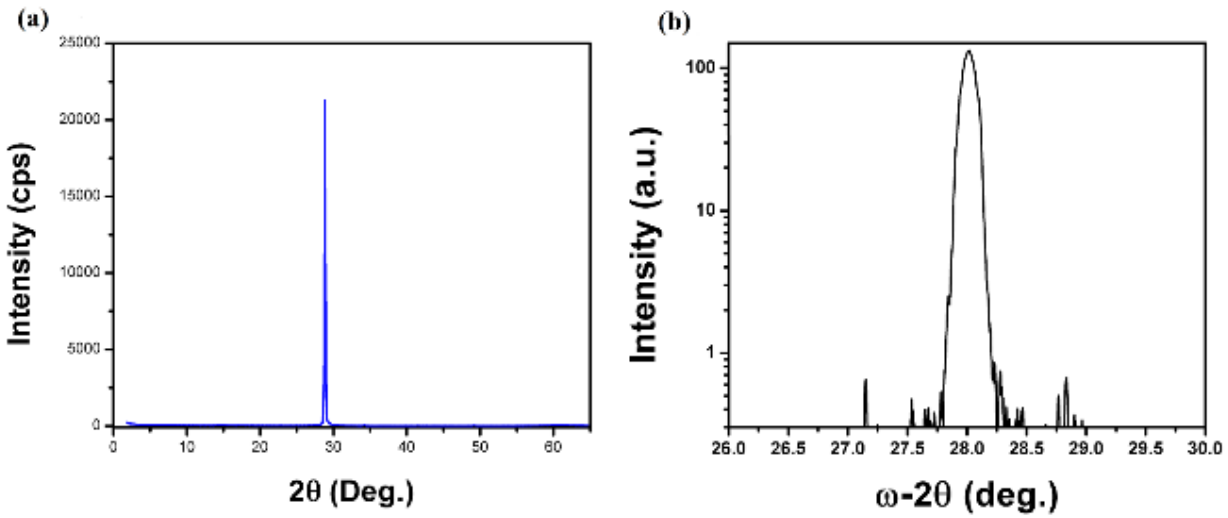


Figure 3-6 XRD pattern for the n-PbSe surface deposited on vicinal germanium substrate: (a) wide-angle scan and (b) rocking curve.

The only major identifiable peak belongs to PbSe (002), with minimal contribution from the equivalent (004) PbSe peak. High-resolution rocking curves taken along the (002) axis reveal a FWHM of 248 arcsec for the dominating PbSe peak. Table 3-2 provides a comparison of the measured FWHM value for PbSe deposited on Ge (100) with PbSe films deposited on other dissimilar substrates with the potential for type-II band alignment, along with FWHM values reported for PbSe grown on nearly lattice matched and thermal expansion coefficient matched insulating BaF_2 (111) and CaF_2/Si (111) substrate respectively.

Table 3-2 Comparison of measured and reported XRD FWHM values for PbSe films on foreign substrates.

Structure	Orientation	Thickness (nm)	FWHM (arcsec)
PbSe/Ge	(100)	1,000	248
PbSe/GaSb[194]	(100)	15ML	---
PbSe/InAs[194]	(100)	310	181
PbSe/InAs[195]	(111)	2,000	1700
PbSe/BaF_2[202]	(111)	1,000	90-275
PbSe/CaF_2/Si[203]	(111)	1,000	140-300

Compared to PbSe films deposited on other dissimilar substrates, the PbSe on Ge shows a markedly improved FWHM value, indicating strong crystalline material quality. The low measured

FWHM value for PbSe on InAs (100) was only achievable for the optimized 310nm film thickness. Thinner PbSe films on InAs (100) were found to have a larger FWHM of 444 arcsec, while thicker PbSe films formed cracks and increased dislocation densities due to the buildup of stress [194]. Further, while the PbSe film on lattice matched BaF_2 substrates often obtain the lowest FWHM values, the PbSe film on Ge has a measured FWHM falling neatly within the typical range expected for PbSe films deposited on the nearly lattice matched and thermal expansion coefficient matched BaF_2 and CaF_2/Si substrates. Photoluminescence measurements were also employed to investigate material quality. Figure 3-7 compares room-temperature continuous wave (CW) PL intensity values for the n-PbSe/p-Ge crystal structure with PbSe films deposited BaF_2 substrate.

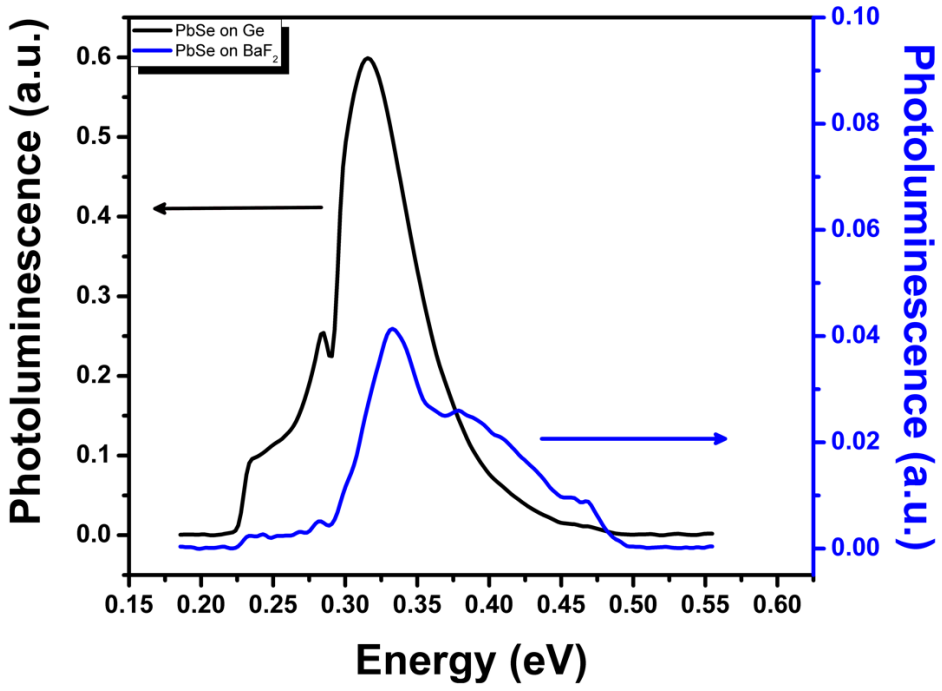


Figure 3-7 Room-Temperature CW PL spectra of PbSe films deposited on Ge and BaF2.

Significant blue shift of the PbSe PL peak was observed for both PbSe on Ge and BaF_2 substrates. This is attributed to the heating effects associated with CW pumping of the samples,

where the low thermal conductivity of germanium (60.2 $Wm^{-1}K^{-1}$) and BaF_2 (11.72 $Wm^{-1}K^{-1}$) result in a higher PbSe lattice temperature than the heat sink temperature [204]. In comparison, PbSe on Ge shows promising CW PL properties with more than a magnitude higher PL intensity compared with monocrystalline PbSe on lattice matched BaF_2 substrate, indicating strong crystalline material quality. With such promising PL recorded for PbSe on electrically active Ge substrates, this novel heterostructure may also find use in MWIR light emitting device applications.

Current-Voltage Statistics

Current-voltage (I-V) measurements were taken on the 270µm x 270µm pixel contacts, ranging from -0.5V to 0.5V. Strong p-n junction behavior was observed at room temperature, with consistently large rectifying factor and low reverse bias current densities for all pixels as seen in Figure 3-8. Current density (J) calculations used only the pixel area covered by the Au contact fingers to avoid overestimation of J-V performance. The low series resistivity measured for the n-PbSe/p-Ge material structure indicates the formation of an ohmic contact, ensuring direct characterization of the heterojunction behavior absent any influence from poor contact formation. Table 3-3 provides a list of both measured and calculated values of interest indicating strong p-n junction behavior suitable for room temperature MWIR detector applications.

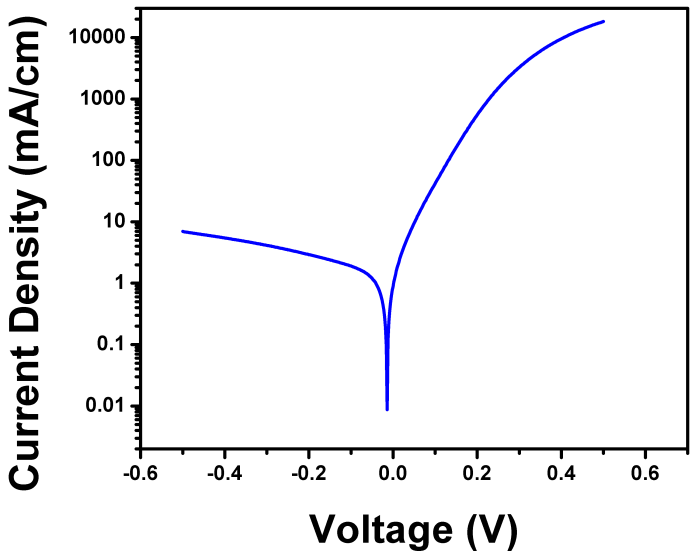


Figure 3-8 Room Temperature J-V statistics.

Table 3-3 Measured and calculated values of interest.

Structure	Contact Dimension	Shunt Resistivity (Ω cm)	Series Resistivity (Ω cm)	Rectifying Factor for 0.5V to -0.5V	Current Density at -0.1V (mA/cm^2)
n-PbSe/ p-Ge	270µm × 270µm	4.03×10^3	0.766	2,609	1.9

IV. Conclusion on n-PbSe/p-Ge Heterostructure

J-V analysis of the n-PbSe/p-Ge heterostructure reveals a high resistance reverse bias p-n junction formation with a low reverse bias current density of only 1.9mA cm^{-2} under -100mV reverse bias. Such strong p-n heterojunction behavior utilizing the MWIR PbSe absorber with SWIR Ge absorber could find great success in MWIR and SWIR photodetector applications, with easy integration into two-color detector systems [205]. Despite good rectification factor, additional work is required to optimize the growth conditions and enhance the detectivity. In the second part of this chapter another novel epitaxial heterostructure with PbSe is studied.

n-CdSe/p-PbSe heterostructure

II-VI/IV-VI heterostructures such as PbSe/CdSe(S) offer another promising alternative. Initial demonstrations of thermally evaporated polycrystalline CdS thin films on PbSe were fabricated to produce the photovoltaic structure for MWIR detection. While the initial results from these experiments have shown great potential, issues with photogenerated carrier blocking and band alignment issues at lower operating temperatures have stunted their progress [198]. The group II-selenide CdSe and group IV-selenide PbSe form an interesting pair. As shown in Table 3-4, the lattice constant of CdSe (6.08 Å) and PbSe (6.12 Å) is close (0.66% mismatch). However, their bandgaps of bulk materials are significantly different, with CdSe being a "wide" bandgap material and PbSe being a narrow bandgap material with room temperature bandgaps of 1.71 eV and 0.27 eV, respectively [206], [207], [208]. These properties offer opportunities to fabricate nearly lattice-matched high-quality PbSe/CdSe heterogeneous devices. CdSe has been widely used as the shell material for PbSe/CdSe core/shell colloidal quantum dots [161], [209], [210], [211], [212], [213], [214], [215], [216]. Two types of crystal structures, cubic zincblende, and wurtzite hexagonal crystal structures have been reported for CdSe with different bandgap energies [207], [208], [217]. Reported band alignments between CdSe and PbSe are not consistent, with the reported electron affinity value of CdSe either slightly higher or lower than that of PbSe resulting in either type-I or type-II band alignment [218], [219], [220], [221].

Table 3-4 Material Properties of PbSe and CdSe

Material	Crystal Structure	Lattice Constant (Å)	Bandgap (eV)	Reference
PbSe	Rock Salt	6.12	0.27	[206]
CdSe	Zincblende	6.08	1.71	[207], [208]
CdSe	Hexagonal	4.3	1.8	[208], [217]

In previous works, we have investigated the polycrystalline II-VI n-CdSe films and IV-VI p-PbSe heterojunction [222], [223]. While PbSe has a cubic rock salt crystal structure, polycrystalline CdSe films typically include hexagonal crystal structure [222]. Such structural difference could introduce interface defects and likely forming type-I band alignment. In this part of chapter, we report a new method for fabricating an all-epitaxial single-phase (cubic) n-CdSe/p-PbSe heterostructure and link its changes in detector behavior to its polycrystalline II-VI predecessors. The aim of this chapter is fabricating an uncooled photovoltaic mid-infrared photodetector with a decent performance. The growth of a single-phase (cubic-zincblende) epitaxial CdSe thin-film on single crystalline PbSe has never been previously reported, and its demonstration here showcases its potential for the future design of enhanced MWIR PbSe-based photovoltaic detectors. In following sections, the growth method of the heterostructure is discussed, then the material quality is characterized with RHEED and X-ray diffraction methods. Then the I-V characteristic is shown, and after all the radiometric measurement is carried out.

V. Experimental Methods n-CdSe/P-PbSe Heterostructure

Epitaxial Heterojunction Growth

The epitaxial n-CdSe/p-PbSe heterostructure was deposited by MBE on freshly cleaved BaF_2 (111) substrate with a background pressure of 1×10^{-8} Torr. BaF_2 substrates were used for

their excellent long-wave optical transmittance and similar crystal structure with PbSe, enabling epitaxial growth and subsequent back-side illumination detector design for device testing. 1.2μm PbSe thin films were deposited by direct evaporation of 99.9999% purity PbSe with 0.1% Se-rich effusion source (49.9% wt% lead atoms and 50.1 wt% selenium atoms) in combination with 99.9999% purity elemental Se effusion source to achieve a p-type carrier concentration of $2\times10^{17}cm^{-3}$. Epitaxial 200nm CdSe thin films were then deposited using 99.999% purity CdSe compound effusion source in combination with 99.999% purity Bi_2Se_3 effusion source to achieve n-type doping.

Device Fabrication

A backside illumination detector structure was fabricated by a photolithography process involving etching of CdSe mesa using a 3:1:1 mixture of 35% HCl acid, 85% phosphoric acid, and DI water for 20 seconds. Se washing was necessary immediately following the CdSe etching to remove the deposited selenium residue from the sample surface. This process consists of 98 wt% H_2SO_4 + 30 wt% H_2O_2 in a 3:1 volume-to-volume ratio.

After forming the mesa structure, 300 nm gold was thermally deposited using Lesker Nano 36, and then lift-off of the gold contacts was performed, and the sample was wire bonded using a wedge gold wire bonder for current–voltage analysis and radiometric measurements. The proposed band structure diagram in Figure 3-9b predicts a type-II heterojunction formation between an n-doped cubic CdSe epitaxial thin film with a p-PbSe layer. After PbSe absorbs the mid-infrared light, an electron–hole pair is generated. Then, the electron–hole pair is separated by the heterostructure's built-in potential. Finally, the electrons are diffused into CdSe, and holes are transported within the PbSe layer until they reach the contact.

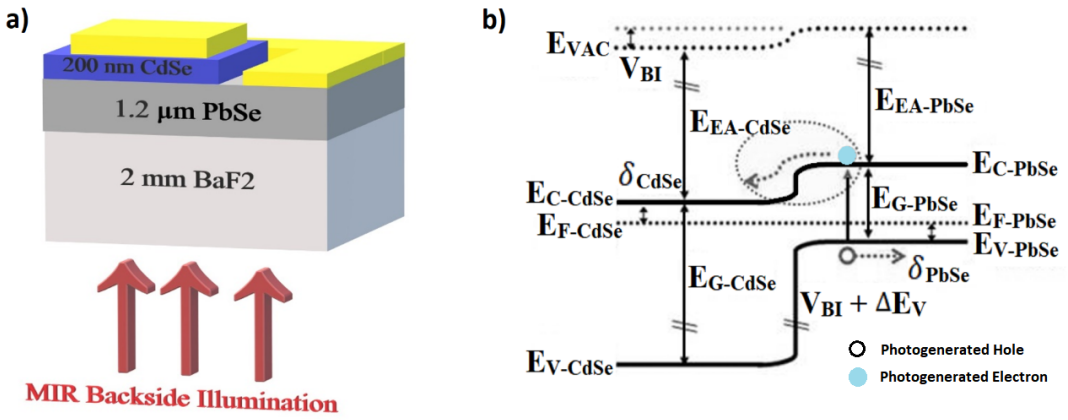


Figure 3-9 (a) Configuration schematic of the n-CdSe/p-PbSe heterojunction mid-IR photodiode with backside illumination 1.2µm PbSe deposited on 2mm BaF2 substrate. Then 200nm CdSe film deposited on top. 300 nm thick gold was deposited on top of CdSe pixel and PbSe to create the contacts. (b) suggested energy band diagram of the n-CdSe/p-PbSe heterostructure (In the figure, Evac, EC, EF, EV, EEA, VBI, EG, ΔEV, δ stands for vacuum energy, conduction band energy, Fermi energy, valence band energy, electron affinity, built-in potential, energy band gap, valence band offset, and energy difference between Fermi energy and conduction band, or Fermi energy between valence band, respectively).

VI. Results and Discussion n-CdSe/P-PbSe Heterostructure

Crystallography and Surface Morphology of Epitaxial CdSe films on PbSe

RHEED is an in-situ powerful tool in MBE to monitor and evaluate the real-time growth procedure. RHEED employs an electron gun to graze the substrate with high-energy electrons. Based on the atomic spacing and crystal structure of the surface of the sample, as well as the wavelength of the incident electrons, diffraction results in the constructive interference of the electrons at specific angles. We used this powerful tool to watch the layer-by-layer growth. In-situ RHEED monitoring of the growth evolution was captured and analyzed using the KSA 400 data acquisition and analysis software tool. XRD was used to corroborate the RHEED observations and examine the surface morphology and crystallography of the epitaxial CdSe thin films on PbSe. In-situ RHEED measurements were performed during the MBE deposition of lead selenide and cadmium selenide epitaxial films on barium fluoride substrates. Special interest was focused on

the nucleation and growth evolution of CdSe thin films on PbSe since the single phase (cubic) epitaxial growth of CdSe on the IV-VI rock salt crystal structure has never been reported.

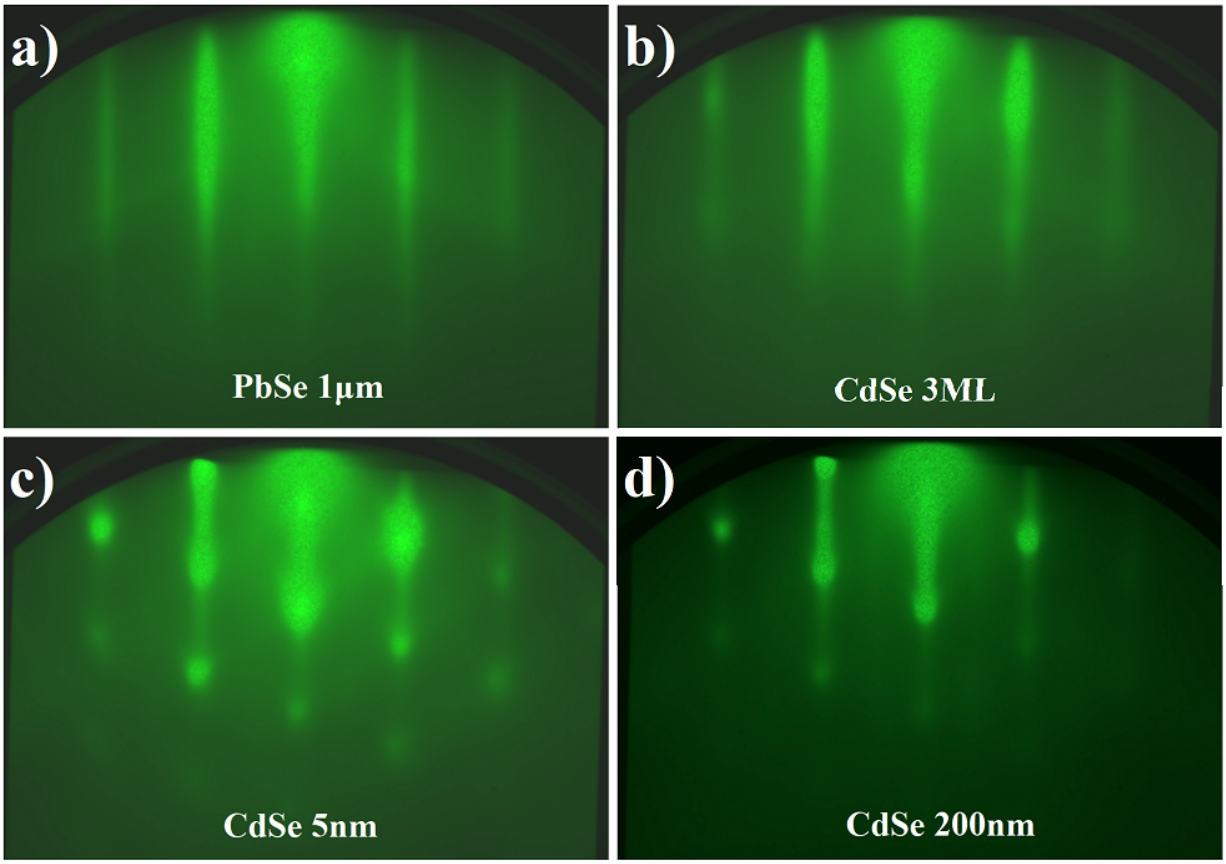


Figure 3-10 . In-Situ RHEED measurements of the characteristic [110] orientation for (a) 1µm thick PbSe film on BaF2, (b) 3ML nucleation of CdSe on PbSe, (c) 5nm of CdSe, and final 200nm bulk CdSe thin film. The nucleation on growth of CdSe suggest that the CdSe followed the PbSe crystal structure and orientation.

Observing Figure 3-10 the nucleation of CdSe shows a strong correlation with the growth surface, matching the structure and orientation of the PbSe seed layer while proceeding in a layer-by-layer growth mode. After the initial deposition accumulation exceeds 5nm, RHEED observations begin to show signs of roughening, with the formation of 3D spots along the [110] direction. The rest of the bulk 200nm thick CdSe growth proceeds virtually unchanged, with no noticeable contributions from varying CdSe crystallites, such as off-orientation cubic CdSe grains

or the formation of a secondary phase of wurtzite CdSe. Interestingly, line profile analysis of the CdSe RHEED images shows an identical diffraction spacing between the [110] CdSe and the [110] PbSe fringes. This indicates that the epitaxial growth of CdSe maintained roughly the same lattice parameter as PbSe during the bulk of the 200nm thin film growth. Only during the last few nanometers of thickness did the line spacing begin to increase, indicating a decrease in the lattice parameter. While PbSe has a relaxed lattice constant of 6.12Å, the literature indicates an expected lattice constant of 6.08Å for cubic CdSe. However, here we observe a slightly larger lattice parameter for the bulk CdSe film deposition closer to the 6.12Å of PbSe. This phenomenon is further investigated in the following XRD measurement and analysis of the as-grown heterostructure.

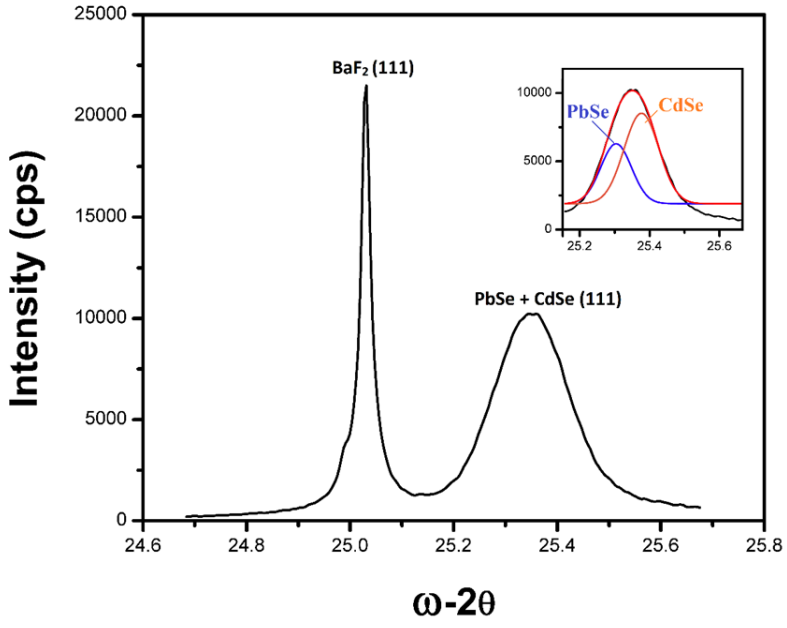


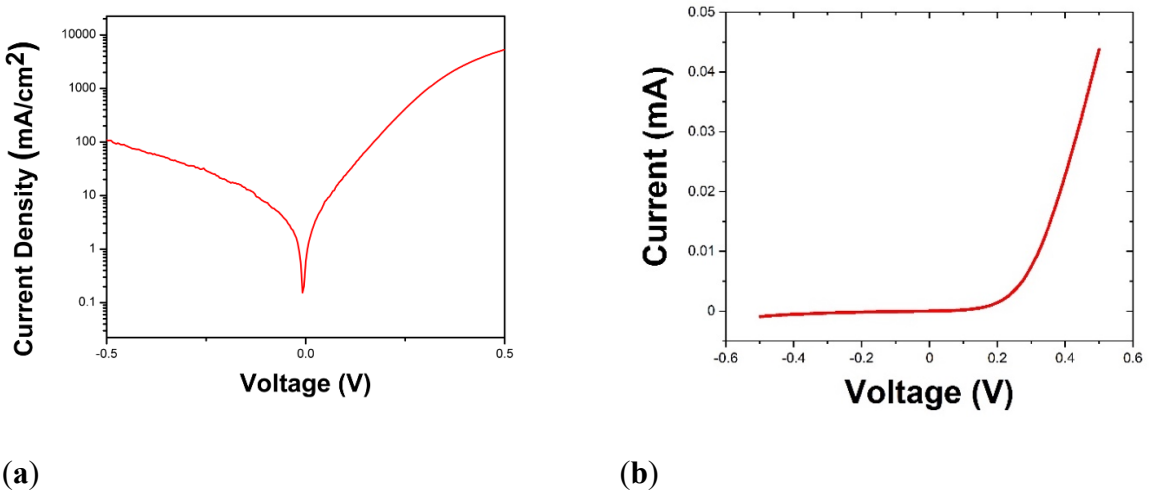
Figure 3-11. XRD measurement of the epitaxial n-CdSe/p-PbSe heterostructure on BaF2 (111) substrate. The inset shows a simulated overlapping peak of PbSe and CdSe.

High-resolution x-ray diffraction measurements were taken of the as-grown CdSe/PbSe heterostructure on BaF_2. XRD scans of the main (111) substrate and layer peaks for PbSe and

CdSe show a striking overlap of their diffraction peak contributions, as was expected from the RHEED investigation. The inset image in Figure 3-11 shows the deconvoluted peak contributions from the PbSe and CdSe layers, with a PbSe (111) peak position of 25.30° and a CdSe peak position of 25.38°. No off-orientation peak contributions were observed for either PbSe or CdSe, and neither were there any contributions from wurtzite CdSe, with characteristic peak positions at 23.4°, 24.8°, 26.5°, and 38.4°. The observations here corroborate the in-situ RHEED measurements observed during the growth of CdSe on PbSe, indicating unambiguously the successful formation of a single phase (cubic) bulk epitaxial CdSe thin film deposited directly on PbSe.

Current-Voltage and Radiometric Measurements

Processing of a 30μm × 30μm pixel for I-V measurement was performed to investigate the potential p-n junction behavior between the epitaxial n-CdSe and p-PbSe films. Current-voltage measurements were performed using a Keithley 2400 source meter instrument.



(a) **(b)**

Figure 3-12. (a) Room-temperature J-V and (b) I-V characteristic of the epitaxial n-CdSe/p-PbSe heterojunction structure shows a strong room temperature p-n junction behavior.

Figure 3-12 (a) shows the J-V statistics for the as-grown n-CdSe/p-PbSe heterojunction structure, demonstrating strong room-temperature p-n junction behavior similar to previous investigations on poly-CdSe/PbSe devices [223]. Notably, a strong rectifying factor is observed indicating the formation of a barrier for the reverse bias current, with a rectifying factor of 50 when comparing the current density at 0.5V forward bias and reverse bias respectively (Figure 3-12 (b)). Subsequently, the reverse bias current density at -100mV is only 7.5mA/cm^2. While reports of similar levels of dark current density have been observed before in PbSe-based PV structures, the report here distinguishes itself in that the low leakage current was observed for the as-grown material structure without any post-growth passivation treatments.

Figure 3-13 shows temperature-dependent radiometric measurements, which were performed from room temperature down to 230K to investigate the signal-dampening phenomenon observed in our previous CdSe/PbSe efforts. The as-grown n-CdSe/p-PbSe structure displays a temperature-dependent signal increase at lower temperatures while maintaining similar noise levels resulting in higher detectivities.

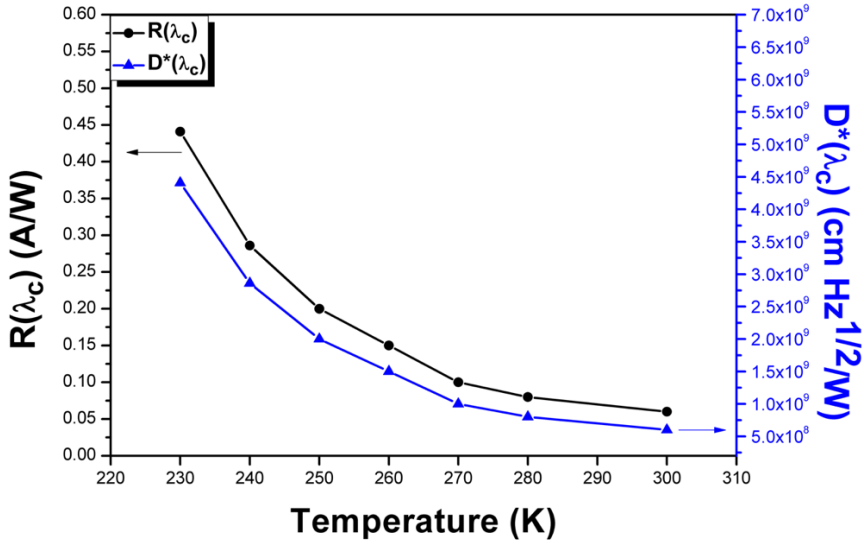


Figure 3-13. Temperature-dependent peak Responsivity and D* measurements from 300K down to 230K under zero bias photovoltaic mode. It shows almost an order of magnitude of higher signal when the device is cooled down to 230K.

To measure the specific detectivity and responsivity, a calibrated 500°C blackbody from Infrared System Development is used for infrared light source. A Thorlabs mechanical chopper is used to modulate the mid-infrared light of the blackbody with a 750Hz chopping frequency. Measurements were done under zero-bias condition The signal and noise currents from the device are collected from a Stanford Research System SR830 lock-in amplifier. The R and Specific D* was calculated using the following formulas.

$$D^* = R * \frac{\sqrt{A*\Delta f}}{I_n} \quad (Jones) \qquad (3\text{-}1)$$

$$R = \frac{I_s}{P_i} \quad (A/W) \qquad (3\text{-}2)$$

Where I_s and I_n are the measured detector output signal and noise currents, A is the device detection area, Δf is the noise bandwidth, and P_i is the incident radiant power. The room temperature 30μm × 30μm pixel achieved a peak responsivity of 0.06A/W and a D* of 6.5×10^8Jones under zero bias photovoltaic operation. With decreasing temperature, the optical signal increased by almost an

order of magnitude as it approached 230K while maintaining a similar level of noise, achieving a responsivity of 0.441A/W and a D* of 4.4×10^{9}Jones at 230K. The temperature-dependent behavior observed in this new single-phase epitaxial n-CdSe/p-PbSe heterojunction device sheds light on the inverted temperature-dependent behavior phenomenon observed by the previous explorations of similar CdSe/PbSe PV detector structures. Here, this new epitaxial interface between cubic PbSe and CdSe films without any contributions from hexagonal-CdSe grains demonstrates the first example of the CdSe/PbSe PV detector structure's continued increase in signal and detector performance down to thermoelectric-cooled operating temperatures. Further, the as-grown detector performance of this new technology demonstrates an almost 3x D* increase at room temperature compared to the as-grown poly-CdSe/PbSe PV detector structure. Combined with the previous studies on device enhancement using post-growth treatment techniques and enhanced device structure design, this new epitaxial p-n heterojunction structure demonstrates a promising advancement in the fabrication of enhanced II-VI/IV-VI interfaces and heterojunctions, with the potential for developing new state-of-the-art MWIR photodetectors operating above cryogenic cooling temperatures.

Chapter 4 Room-temperature Nano-structured PbSe/CdSe Mid-Infrared Photodetector: Annealing Effects[2]

I. Introduction

Reducing SWaP+C while maintaining good range and resolution has been the key goal for FPA imagers [53]. In MWIR, a low SWaP+C imager is highly desirable for many applications such as small unmanned aerial vehicles, smart munitions, and missile defense. Elimination of bulky and expensive cryogenic cooling systems and monolithic integration on Si ROIC to reduce fabrication cost and to increase yield become two essential requirements for low SWaP+C MWIR imagers. Polycrystalline IV-VI semiconductor PbSe PC meets both requirements. PbSe MWIR photoconductor detector has demonstrated room temperature D* of 2.8×10^{10} Jones and 4.2×10^{10} Jones at ~3.8 μm, without and with anti-reflective coating [89], [101], [224]. Monolithic integration of MWIR FPA on Si ROIC has been demonstrated [225], [226]. However, one key challenge for the state-of-the-art PbSe PC FPA grown by CBD is the large inhomogeneity of polycrystalline film which requires ROIC to perform powerful non-uniformity correction on pixels and thus increases the power consumption and cost. Besides PbSe, narrow gap MCT , and Type-II superlattice structures, are leading material systems for high-performance MWIR photodetectors [227], [228]. However, their growth necessitates a lattice-matched substrate and the costly MBE method for high performance, which makes the monolithic integration with Si ROIC difficult [24].

---

[2] This chapter is based on: **Milad Rastkar Mirzaei**, and Zhisheng Shi " Room-temperature Nano-structured PbSe/CdSe Mid-Infrared Photodetector: Annealing Effects ", Journal of Vacuum Science and Technology B (2024).

M. Rastkar Mirzaei author contribution: M. Rastkar Mirzaei contributed to conceptualization (supporting), data curation (lead), investigation (lead), methodology (lead), software (lead), visualization (lead), writing—original draft (lead), and writing—review and editing (supporting).

In recent decades, nanostructures such as QDs have emerged as one of the most compelling technologies in the field of optoelectronics to replace bulk materials [229], [230]. QDs are minute semiconductor clusters where the wave functions of electrons and holes are determined by quantum confinement effects. In simpler terms, the energy levels of QDs are quantized due to their size being smaller than the Bohr radius. This leads to unique attributes including an adjustable bandgap for tailored cutoff frequencies, effective light absorption, and the potential for high-temperature operation [229], [231], [232], [233]. There are two prominent methods for producing QDs. The first method is the epitaxial-self-assembled QDs (ESAQDs). In the deposition procedure, epitaxial islands spontaneously emerge on the crystal surface due to the strain of mismatched substrate [234]. Subsequently, these islands are transformed into QDs. The performance of MWIR photodetectors made with these QDs is often limited by low absorption, primarily due to the less dense distribution of QDs [235]. Also, the cost of synthesizing these QDs is high because of the use of expensive epitaxial methods, such as MBE or MOCVD [236]. Another method for synthesizing QDs is through wet chemical process, resulting in what is known as CQD. CQDs offer numerous advantages, such as the ease of synthesizing them through a solution-based process that doesn't necessitate expensive instruments. Additionally, this method provides a robust growth technique, ensuring the production of homogeneous QDs [237]. Nevertheless, the requirement for ligand exchange in CQDs contributes to elevated production costs and demands additional labor [147], [238]. Furthermore, in the case of lead-chalcogenide, synthesizing giant high-performance CQD to cover the MWIR range remains a challenge [236].

Three primary material systems have been explored for QD MWIR photodetectors, specifically, lead-chalcogenide, mercury-chalcogenide, and silver-chalcogenide. Mercury chalcogenides belong to a group of binary semiconductors characterized by narrow or even

negative band gaps [239]. Among the mercury-chalcogenides (HgS, HgSe, and HgTe), HgTe QDs are the most studied from the synthesis and application viewpoint [141]. HgTe is considered a semimetal with an inverted band structure attributed to its significant spin-orbit coupling [240]. Consequently, its QDs possess the capability to span the entire MWIR spectrum [240]. In contrast to HgTe QDs which behave as intrinsic material, HgSe [241] and HgS [242] QDs are inherently n-doped and display intraband transitions rather than interband transitions [243]. HgTe QD devices demonstrate superior performance compared to other QD mercury chalcogenide materials. In 2018, researchers achieved a room-temperature D* of 3 x 10^8 Jones with a photovoltaic HgTe CQD photodetector, featuring a cut-off wavelength of 3.8μm at 290K [150]. In a recent paper, Xue et. al., achieved D* of 7.6 x 10^9 Jones with photovoltaic HgTe CQD Photodetector having a cut-off wavelength of 3.5μm [244]. Despite the good performance of mercury-chalcogenides QDs, researchers are exploring alternatives to mercury-based photodetectors due to concerns about the toxicity of mercury. One candidate is silver-chalcogenide. Ag_2Se is another option showing a strong intraband absorption peak in MWIR because of its self-doping ability with excess silver ions [147]. In 2021, Hafiz et. al. reported a heterostructure of Ag_2Se and PbS QDs with a cutoff wavelength at 6μm and a specific detectivity of 1 x 10^7 Jones operating at room temperature [156]. Nevertheless, photodetectors utilizing self-doped silver-chalcogenide QDs encounter challenges in their ongoing enhancement journey. The most studied material for infrared QDs photodetectors is lead-chalcogenide [245], [246], [247]. However, the majority of dedicated research is conducted in the SWIR and even the NIR regions due to the challenges associated with the colloidal method in producing large, high-quality PbSe QDs that can effectively cover the MWIR region [24], [147]. In this study, we report a novel interconnected PbSe/CdSe nanostructure grown by VPD for RT MWIR detector with much-improved homogeneity. In comparison to epitaxial QDs, this approach

offers cost-effectiveness and the potential to monolithically integrate with Si ROIC, thanks to the growth on SiO_2/Si (100) substrates. VPD presents a range of favorable attributes, including cost-efficiency, precise growth control, uniformity, reproducibility, and compatibility with CMOS technology [97], [248]. The nanostructure also offers other advantages over its bulk PbSe photoconductor counterpart including the tunability of cut-off wavelength and potential performance improvement due to quantum effects. To evaluate the performance of the photodetector, we have performed blackbody radiometric measurements on samples with different annealing conditions and achieved peak D* of 2.49×10^9 Jones.

II. Experimental Details

Material and Device Structure

High purity (99.999%) PbSe and CdSe source materials are used for the growth of 60 alternating PbSe and CdSe layers. The structure was grown on a commercial SiO_2/Si substrate at 350°C using a custom-designed thermal evaporator under a background vapor pressure of 2×10^{-4} Pa. The deposition rates for PbSe and CdSe are 2.9 Å/second and 1 Å/second, respectively, with a deposition time of 25 seconds for PbSe and 70 seconds for CdSe to form heterogeneous nanostructures. The total thickness is 850nm. After the growth, the samples are cleaved into dimensions of 2mm x 4mm. Subsequently, the as-grown films undergo annealing within the temperature range of 425-450°C, utilizing ultra-high purity oxygen gas at a flow rate of 40 standard cubic centimeters per minute (SCCM). Following that, gold contacts, each measuring 200nm in thickness, are deposited to both sides of the photoconductor using a Kurt J. Lesker Nano360 thermal evaporator, resulting in an active area of 2mm x 2mm for light absorption. The schematic for the device is shown in Figure 4-1a.

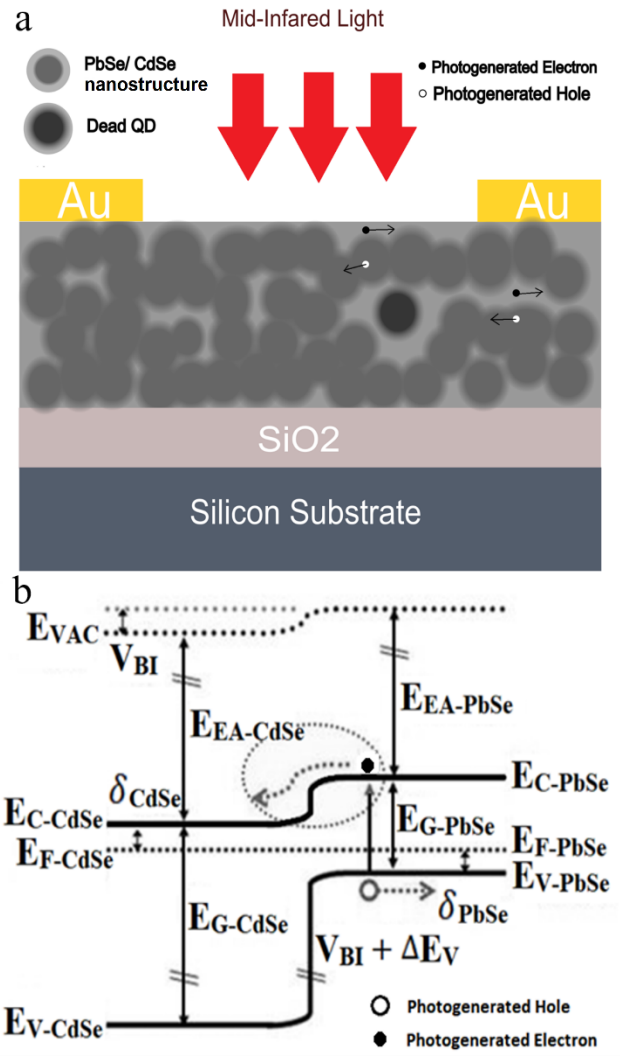


Figure 4-1. (a) Schematic structure of the PbSe/CdSe NC photodetector (it should be noted that nanostructures are depicted in spherical shape only for simplicity of presentation). (b) band diagram of the PbSe/CdSe type-II heterostructure.

Material and Device Structure

The as-grown films undergo characterization using a Zeiss Neon-40 EsB high-resolution field-emission scanning electron microscope (FE-SEM). A Bruker Invenio-R Fourier transform infrared (FTIR) spectrometer with a 16 cm^{-1} resolution is used to measure transmission in the MWIR range and is used to determine the absorption edge.

Signal, noise, and subsequently detectivity measurements are conducted at room temperature (300K) employing an SR830 DSP lock-in amplifier from Stanford Research System, in conjunction with an Infrared System Development Corp. collimated blackbody source maintained at 823K and modulated at 750Hz (MC1F10 from Thorlabs). The calculations for Responsivity in volts per watt and D* in Jones are determined using the following equations.

$$P_{in} = (A_{det}A_{BB}t\beta/d^2) \times 2c^2h \int_0^{\lambda_c} 1/(\lambda^5 \times (e^{\frac{hc}{\lambda KT}} - 1))d\lambda \quad (4\text{-}1)$$

$$R = \frac{v_s}{P_{in}} \ (V/W) \quad (4\text{-}2)$$

$$D^* = R \times \frac{\sqrt{A_{det} \times \Delta f}}{v_n} = \frac{v_s}{v_n} \times \frac{\sqrt{A_{det} \times \Delta f}}{P_{in}} \ (Jones) \quad (4\text{-}3)$$

Where, P_{in} is the incident optical power up to the cut-off wavelength of the active area of the device from blackbody radiation, and β(=0.45), T(=300K), t (=0.7, based on the refractive index of PbSe and CdSe.), A_{det}(=0.04cm^2), A_{BB}(=0.2cm^2), d (=40cm), λ_c(=4μm), v_s, v_n, and Δf(=1Hz) are the Blackbody chopper modulation coefficient, blackbody temperature, transmission coefficient of the detector film, detector active area, blackbody aperture, detector to blackbody distance, cut-off wavelength, signal voltage, noise and noise measurement bandwidth, respectively. The noise spectrum is measured by the SR760 FFT Spectrum Analyzer. The Agilent E3612A source and ST-500 probe station from Janis Research serve for device biasing, with a load resistor tailored to match the detector resistance. Also, the bias voltage given in this paper is the voltage drop on the detector. Peak D* is calculated using the method in ref [249].

III. Experimental Details

Band structure and carrier transport mechanism

It has been shown that the cubic p-PbSe and cubic n-CdSe form type-II heterojunction[211], [247]. The band alignment for the type-II p-PbSe/n-CdSe is shown Figure

4-1b [95]. Similar to the epitaxial self-assembled quantum dots, the nucleation process of the PbSe/CdSe deposition on SiO_2/Si can be described below. Due to the large dissimilarity of the SiO_2 substrate and deposited PbSe, self-assembled three-dimensional PbSe islands will be formed. Then, most of the following CdSe atoms will tend to nucleate on top of the PbSe island and some may form nucleation sites on uncovered SiO_2 substrate. As the process goes, the film will be smoothened. By controlling the island size with deposition rate, the as-grown alternating layers of PbSe and CdSe should form some shape of core/shell nanostructure. Our previous studies have shown that PbSe, CdSe, and heterojunction PbSe/CdSe grown at such substrate temperature form polycrystalline films. Following annealing, it is reported that the CdSe shell fractures reconfigure and ultimately form a heterostructure with PbSe in a Janus-like configuration [213, p. 022], [250]. With the appropriate sizes of the nanostructures, annealing could connect the PbSe cores and the CdSe shells, resulting in a hetero-nanostructure composed of interconnected PbSe and CdSe. The type-II p-PbSe/n-CdSe junction will separate the photo-generated carriers. As shown in Figure 4-1a, when bias is applied across the two contacts, the holes are conducted through the interconnected p-PbSe *nanostructure*, while the electrons flow through the interconnected n-CdSe. If a PbSe core remains unconnected to other PbSe cores, and the holes within it cannot tunnel through the CdSe barrier to reach the next PbSe core, it becomes a dead cell, as illustrated by the isolated PbSe cell in Figure 4-1a. While these dead cells do absorb light, they do not contribute to the photocurrent.

Surface morphology and absorption spectrum

Figure 4-2a and b show cross-sectional SEM images of as grown and annealed PbSe/CdSe films. The surface roughness is less than 150nm which is much smoother than CBD-grown PbSe films with typical roughness of 200-300nm [103]. As can be estimated from Figure 4-2, the

majority of polycrystalline grain size of the as-grown PbSe/CdSe film is between 150-300 nm. After annealing the typical grain size increases to 0.5-1μm, indicating recrystallization and restructure. Annealing in oxygen passivates the defects [82] at the grain boundary and could create the suggested 3-dimensional networks comprising interconnected PbSe and CdSe nanostructures.

Fourier transform infrared is employed for absorption analysis. The PbSe/CdSe film is grown on sapphire substrates transparent to MWIR along with SiO_2/Si (100) substrates in the same VPD run. The film on sapphire is utilized to examine the absorption edge and absorbance spectrum. The film on SiO_2/Si (100) on the other hand is used for detector fabrication and other analyses. To minimize potential variations between the samples, the sample on the sapphire substrate undergoes the same annealing process as the samples on SiO_2/Si substrates. The inset of Figure 4-2c illustrates the absorption spectra of PbSe/CdSe film on the sapphire substrate with a total thickness of 850nm annealed at 430°C. Utilizing the absorbance and transmission spectrum, we generate the Tauc plot (Figure 4-2c), which exhibits two linear regions. These linear regions aid in calculating absorption band edges, yielding values of 0.31eV and 0.44 eV. The 0.31eV absorption edge exceeds the bulk PbSe bandgap of 0.278eV, suggesting a quantum confinement effect. The absorption edges at 0.44 eV are attributed to higher sub-band transitions of PbSe nanostructure [251]. The low absorption edge of 0.31 eV (4 μm) is used as the cutoff wavelength for the photoconductor annealed at the same temperature.

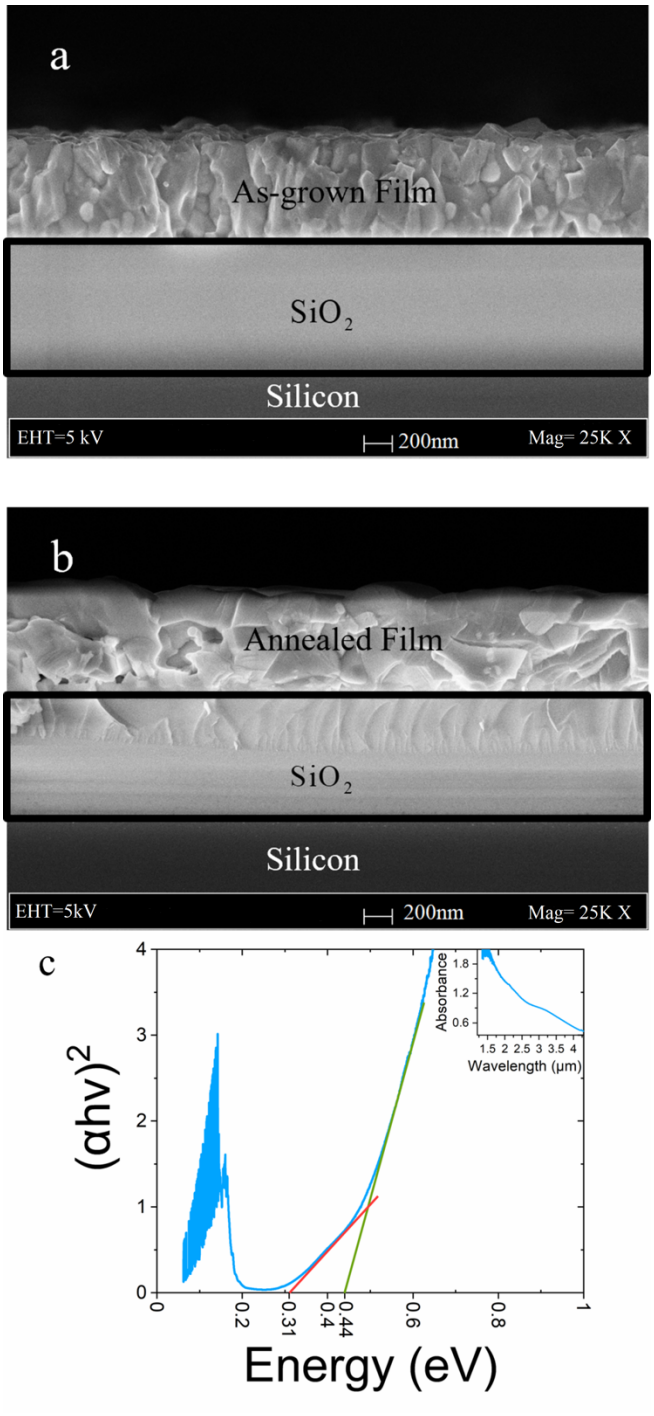


Figure 4-2. Cross-sectional SEM of as grown (a) and annealed (b) sample. (c) Tauc plot for annealed sample. The inset shows the absorption spectrum of the sample.

Device Optimization Through Annealing Conditions

We investigated four different annealing conditions across all four samples, while keeping the annealing time and oxygen flow constant at 30 minutes and 40 SCCM, respectively. The annealing temperatures are 425°C, 430°C, 440°C, and 450°C for samples #1, #2, #3, and #4, respectively. Figure 4-3b depicts the annealing temperature effect on the resistivity of different samples. As evident from the data, there is a substantial rise in resistivity corresponding to an increase in annealing temperature. Bulk PbSe, characterized by its inherently high carrier concentration, significantly contributes to dark current levels in as-grown PbSe photoconductors. The elevated background carrier concentrations pose considerable challenges in the detection of MWIR light using bulk PbSe photoconductors. Hence, researchers have explored annealing techniques involving oxygen, and in some cases, oxygen and iodine, aimed at reducing background carrier concentrations [252], [253], [254]. Figure 4-3a shows the signal and noise characteristics for four different samples at 7.5V bias voltage. The signal exhibits an increase from 0.92 mV to 1.94 mV as the annealing temperature is raised from 425°C to 430°C. This initial signal enhancement with increasing annealing temperature can be attributed to several advantageous processes. Firstly, defect passivation plays a crucial role. Previous studies have demonstrated that oxygen annealing can enhance the photoresponse of lead-salt photoconductors by passivating selenium vacancies and interstitial defects [82], [224]. Annealing could also reduce defects at PbSe/CdSe interfaces and grain boundaries. Additionally, the annealing process could result in the proposed hetero-nanostructure of interconnected PbSe and CdSe 3D networks. As mentioned in Ref. [89], the nano-structured p-PbSe/n-CdSe heterojunction could effectively separate the electrons and holes leading to reduced carrier concentration and improved mobility. For a given as-grown PbSe/CdSe nanostructure, an optimal annealing temperature should passivate defects

most effectively and create the interconnected 3D network. With the four annealing conditions, annealing at 430°C shows the highest signal of 1.94mV. Signal decreases at higher annealing temperatures to 1.1mV and 0.67mV for 440°C and 450°C, respectively. The decline in signal could be attributed to over annealing which may lead to formation of thicker oxide layers at grain boundaries, blocking some of the carrier transport pathways. As shown in Figure 4-3a noise on the other hand decreases with increase in annealing temperature. The noise decrease could be due to the decrease in dark current since resistivity increases with annealing temperature as shown in Figure 4-3b. Higher annealing temperature could also improve the defect passivation which reduces generation and recombination (GR) noise. To discuss the noise contribution, we plotted the calculated Johnson and shot noise (in voltage) shown in Figure 4-3a from the equations below:

$$v_{th} = \sqrt{4KTR\Delta f} \tag{4-4}$$

$$v_{sh} = \sqrt{2qI\Delta f} \times R = \sqrt{2qVR\Delta f} \tag{4-5}$$

Where K is the Boltzmann constant, T is temperature, R is the detector resistance, Δf is the noise measurement bandwidth (=1Hz), I is the sum of dark current and photocurrent, and V is the sum of DC bias voltage and AC signal voltage. As can be seen in Figure 4-3a, the sum of the thermal noise and shot noise is smaller than the measured noise with annealing temperatures below 440°C, suggesting that GR noise is the dominating noise and that higher annealing temperature reduces the GR noise by passivating defect more effectively. However, at 450°C, the calculated shot noise value is close to the measured noise value due to current increase at higher voltage. Figure 4-3a also shows that sample #2 annealed at 430°C has the highest signal-to-noise ratio. Figure 4-3c shows the RT specific detectivity (D*) and a peak D*. Sample #2 annealed at 430°C achieved D* of 6.75×10^8 Jones and peak D* of 1.96×10^9 Jones at 7.5V bias voltage.

We noticed that the 430°C annealing temperature used in this paper is about 30 degrees higher than that of the typical CBD PbSe photoconductors. Although monolithic integration of annealed CBD PbSe photoconductor FPA on Si ROIC has been demonstrated, lower annealing temperature is much preferred to make this technology more Si-CMOS friendly. Future work will aim to lower annealing temperature by optimizing device structures, oxygen flux, and annealing time.

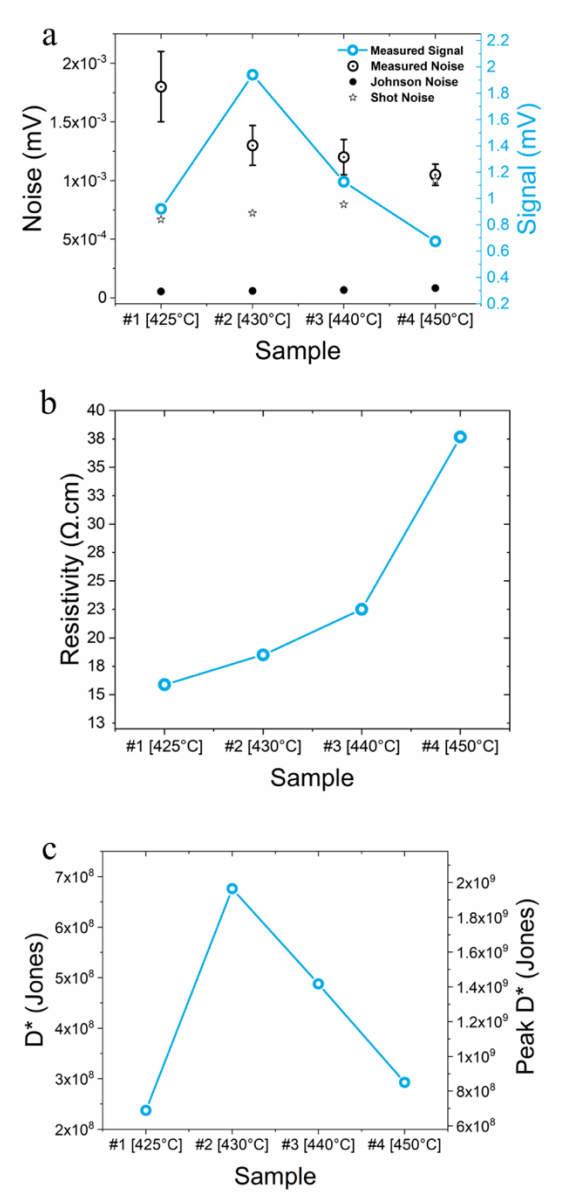


Figure 4-3. (a) Signal and noise, (b) resistivity, (c) D* and peak D* intensity of four different samples annealed at 425°C to 450°C.

Device Radiometric Characteristics

Because of the better performance of sample #2, bias-dependent radiometric measurements and frequency-dependent noise analysis are performed as shown in Figure 4-4. The signal (Figure 4-4a) exhibits a linear increase from 1.94mV to 14.5mV in the bias range of 7.5V to 45V.

Conversely, the noise does not escalate at the same rate as the signal does. As shown in Figure 4-4a, the sum of calculated voltage-dependent shot noise and Johnson noise is smaller than the measured noise. This suggests that the voltage (E-field)-dependent GR noise, likely from surface/interfaces is dominant. Figure 4-4b shows frequency-dependent noise spectrum. The knee frequency for bias voltages up to 30V is around 300Hz. It is apparent that the 1/f noise can be ignored at 750Hz chopper frequency of the measurement in the bias range, though at 45V 1/f noise contributes a small portion of the total measured noise value. As shown in Figure 4-4c, the highest signal-to-noise ratio occurs at 30V bias and D* and peak D* are determined to be 8.57×10^8 Jones and 2.49×10^9 Jones, respectively, using the measured 4 μm absorption edge as the cut-off wavelength.

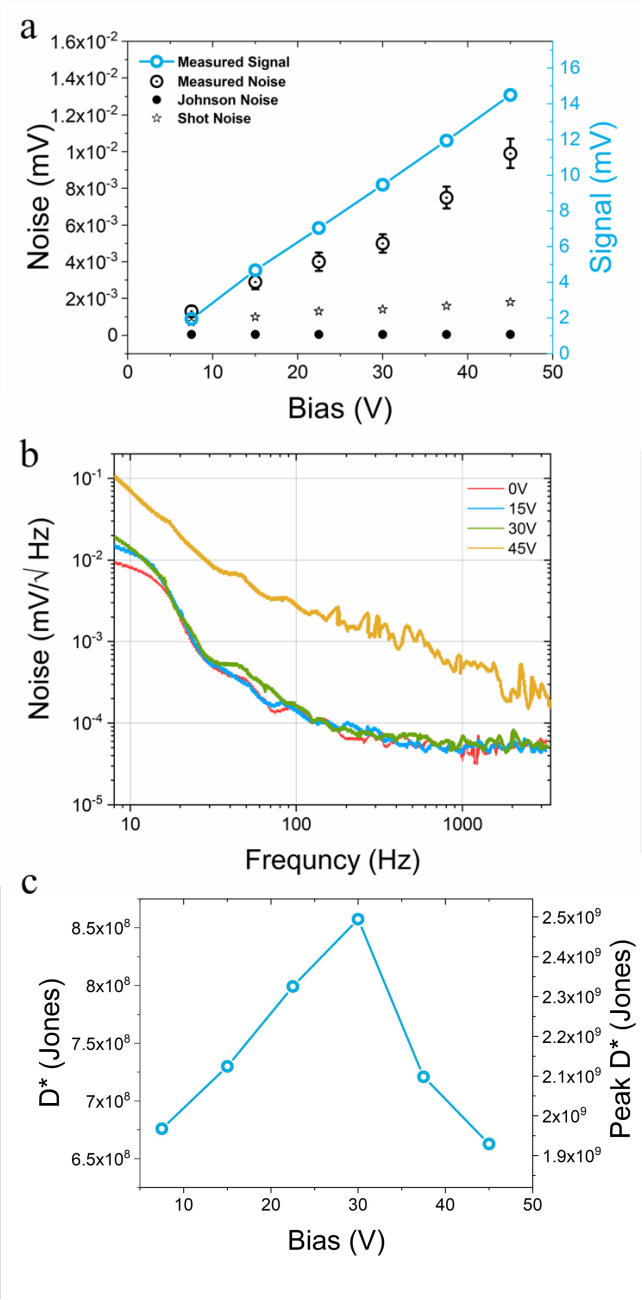


Figure 4-4. (a) Bias-dependent signal and noise for sample #2. (b) 1/f noise spectrum. (c) Specific detectivity D* and peak D* VS. bias for sample #2.

IV. Summary and Conclusion

This research introduces a new PbSe/CdSe nano-structure network grown by VPD for potential high-performance RT MWIR photoconductor with improved surface morphology.

Through oxygen annealing interconnected 3D nanostructures are believed to be formed, facilitating charge separation for photogenerated carriers and passivating defects. The annealing temperature impacts the performance of the photoconductor. This optimal temperature under current annealing conditions for the structure is found to be 430°C with a resultant encouraging peak D* of 2.49 x 10^9 Jones. VPD method produces significantly improved surface smoothness compared to the state-of-the-art CBD method. Further performance enhancement is anticipated due to the quantum effect of the nanostructured PbSe/CdSe. In our future efforts, we will focus on lowering the annealing temperature to enhance compatibility with the silicon ROIC. Simultaneously, we aim to optimize the device structure to enhance the detector performance.

The ability to fabricate MWIR detectors on cost-effective SiO_2/Si(100) substrates via the affordable VPD method enables low-cost monolithic integration with Si-based ROIC for large-scale FPAs and potentially MWIR-integrated photonics on the Si platform for sensing applications.

Chapter 5 High-performance uncooled PbSe/CdSe nanostructured Mid-Infrared Photodetector with Tunable Cut-off Wavelength[3]

I. Introduction

For several decades, MWIR photodetectors (PDs) have been intensively explored, and their capabilities are well-proven for applications in gas and bio-marker sensing, security and defense, medical diagnostics, and astronomy [255], [256], [257]. Epitaxial mercury-cadmium-telluride and type-II superlattice structures are the leading MWIR PDs in detectivity performance [227], [228]. However, due to the requirement of cryogenic cooling to maintain high performance, these PDs are facing challenges in reducing SWaP+C at RT [258], [259]. Therefore, there is a demand for high-performance uncooled MWIR PDs with fast response times and low SWaP+C. To date, the low-cost solution for uncooled MWIR PDs is CBD polycrystalline PbSe photoconductors (PCs) [224]. PbSe PC FPA grown by CBD with promising performances have been demonstrated [225], [226]. Some challenges still remain including film inhomogeneity for such PbSe PC FPA which requires implementation of complex Si ROIC to mitigate non-uniformities in performance.

Promising progress has been made to grow PbSe PC films by alternate methods [50], [175], [260], [261], [262], [263], [264]. However, the performance lags behind that of the CBD technology. Vapor phase deposition (VPD) is a competing technology to produce more uniform

[3] This chapter is based on: **Milad Rastkar Mirzaei**, and Zhisheng Shi " High-performance uncooled PbSe/CdSe nanostructured Mid-Infrared Photodetector with Tunable Cut-off Wavelength", Applied Physics Letters (2024).

M. Rastkar Mirzaei author contribution: M. Rastkar Mirzaei contributed to conceptualization (supporting), data curation (lead), formal analysis (supporting), investigation (lead), methodology (lead), visualization (lead), writing—original draft (lead), and writing—review and editing (supporting).

lead-salt PDs with promises such as low cost, good uniformity, and CMOS compatibility [97], [248], [265]. A RT peak D* of $1.6x10^{10}$ Jones is reported [103] for VPD-grown PbSe with a more uniform morphology, which approaches the best reported RT peak D* of $2.8x10^{10}$ Jones by the CBD method [101].

QD MWIR thin film PDs are another promising approach, especially when specific wavelength photodetection is required, making them particularly intriguing for gas sensing applications [266]. QD MWIR PDs offer several advantages over conventional PDs, including quantum confinement and tunable bandgaps [267], enhanced photoresponse from efficient light absorption [231], [232], [233], and improved operability at elevated temperatures owing to reduced thermal carrier generation [244]. Among various promising approaches of QD PDs [141], [143], [239], [267], [268], [269], [270], [271], [272], [273], the best performance is demonstrated by CQD Mercury-telluride PDs with RT D* of $7.6x10^{9}$ Jones at 3.5μm [244]. Another MWIR material is PbSe with a bulk bandgap of about 0.278eV (4.46μm) and a large Bohr radius of 46nm. However, reported PbSe CQDs have predominantly been in the NWIR and SWIR spectrum [161], [162]. This is due to synthesis limitations of high-quality large-size PbSe CQDs, such as low air stability and difficulty in cation exchange for shell growth [147]. The air instability of large PbSe QDs stems from inadequate surface defect passivation, as they grow in the (100) orientation with no available dangling bonds for effective ligand binding. Consequently, these larger QDs exhibit high surface defect levels, impeding performance [24]. Thus, there's a need for tunable RT high-performance photodetectors that can match CBD PbSe PCs' performance without their drawbacks.

In previous chapter, we developed a large-area (2mm x 2mm) nanostructured PbSe/CdSe photoconductor with a 4μm cut-off wavelength using the VPD method to address wet chemical synthesis issues and studied the impact of annealing [102]. In this chapter, in addition to the much-

improved surface smoothness of our VPD film compared to CBD film, we demonstrate cutoff wavelength tunability with nanostructures of two different sizes. RT peak D* of $2.17x10^{10}$ and $1.61x10^{10}$ Jones for pixels with absorption edge at 3.75μm and 4μm, respectively, is demonstrated. Such PbSe/CdSe NC PC detectors demonstrate promise for RT high-performance MWIR PDs with tunable bandgaps and pave the way for large-scale, low-cost production, and monolithic integration with silicon ROIC.

II. Experimental Details

The samples were grown using a custom-designed VPD system with high-purity (99.999%) PbSe and CdSe sources on commercial SiO_2/Si and sapphire substrates. An automatic shutter control system ensured precise multi-stacked growth. For samples #1 and #2, 120 and 90 alternating squence of PbSe and CdSe were deposited at PbSe rate of 0.91Å/Sec for 29 and 64 seconds, respectively. The CdSe deposited with a rate of 0.28Å/Sec for 63 seconds for both samples at 350°C substrate temperature, at $2x10^{-4}$ Pa background vapor pressure. During PbSe deposition, the CdSe shutter remains closed, and vice versa, to prevent co-deposition and minimize the risk of ternary PbCdSe compound. Similar to the epitaxial self-assembled QDs [234], [274], and as discussed in previous chapter [102], The nucleation process of PbSe/CdSe deposition on SiO_2/Si starts with the formation of self-assembled three-dimensional PbSe islands due to the dissimilarity between the SiO_2 substrate and PbSe. Subsequent CdSe atoms mostly nucleate on these PbSe islands, with some forming on the unfilled SiO_2 substrate. The film smoothens over time, and by controlling the deposition rate, alternating layers of PbSe and CdSe are expected to form a core/shell nanocrystal of some kind (5-4 (a)).

XRD Analysis

Figure 5-1c depicts the XRD analysis for both as-grown and annealed sample. The crystal structure of both the as-grown and annealed samples exhibits the presence of cubic PbSe. Specifically, peaks are observed at 2θ=25.27°, 29.17°, 41.79°, 49.41°, 51.84°, 60.45°, 68.76°, and 76.3°, corresponding to (111), (200), (220), (311), (222), (400), (420), and (422) facets, respectively. The growth of PbSe NCs is dominated by the (200) and (400) planes, followed by (220) and (111) planes. After annealing, {111} planes are significantly suppressed, while {100} planes remain unchanged. This is likely due to oriented attachment and Ostwald Ripening, as observed in sensitized VPD-PbSe and QDs [103], [163]. During this process and at lower annealing temperatures, the PbSe NCs with the same orientation combine to form larger ones [275]. At higher annealing temperatures, all crystallites transform into {100} or react with oxygen, which is because the {100} facet is a non-polar surface, consisting of both lead and selenium atoms. That is why among other facets, it is the most stable one [103] with a surface energy of 0.184 J m^{-2}. In contrast {110}, and polar {111} facets have a significantly higher surface energy of 0.318 J m^{-2} and 0.328 J m^{-2}, respectively [276]. The peak at 2θ=41.86° corresponds to hexagonal CdSe (110), whereas multiple peaks of cubic CdSe are observed at 2θ=25.45° (111), 44.45° (200), 49.47° (311), 61.68° (400), and 65.85° (420).

To estimate the crystallite sizes (D) before and after annealing, we obtained data from the PbSe (400) and CdSe (400) XRD peaks (dominant peaks) and calculated the crystallite sizes using Scherrer's equation with a shape factor (K) of 0.9 and the X-Ray wavelength (λ) 1.5406 Å and summarized the data in:

$$D = \frac{K.\lambda}{\beta.cos\theta} \tag{5-1}$$

Table 5-1. As-grown and annealed Scherrer equation parameters and crystallite size

Sample	Bragg Angle θ (°)	β (radian×10^{-3})	Crystallite Size (nm)
As-grown PbSe (400)	30.25	7.5	21.4
Annealed PbSe (400)	30.25	5.76	27.91
As-grown CdSe (400)	30.84	2.27	71.1
Annealed CdSe (400)	30.84	2.79	58.04

Using the Scherrer equation to estimate crystallite size from the XRD peaks of the dominant PbSe (400) and CdSe (400) reflections reveals a PbSe core size of 21.4 nm and a CdSe size of 71.1 nm. These results suggest that CdSe may wrap around a PbSe core, forming a core/shell nanocrystal configuration. The cubic PbSe and CdSe (with bandgap of 1.71eV [208]) Shell form a type-II band alignment [95], [102], [211], [247], where electrons and holes will be separated. The presence and dominance of cubic PbSe and CdSe is confirmed via XRD analysis (Figure 5-1 (c)). Following the growth, the as-grown films are annealed at the temperature range of 365-400°C with a flow rate of 45SCCM ultra-high purity oxygen gas. The Si ROIC can withstand annealing temperatures around 400°C [248].

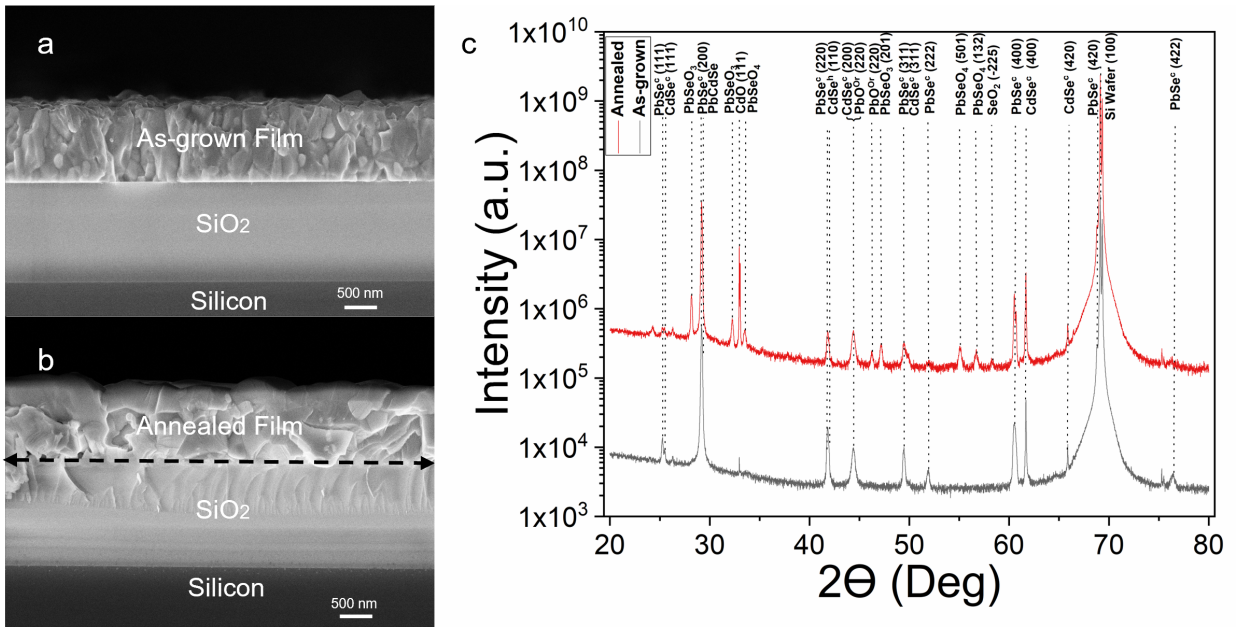


Figure 5-1 FE-SEM and XRD images of as-grown and annealed sample #2: (a) Cross-sectional FE-SEM of as-grown sample #2 displaying a smooth film surface. (b) Cross-sectional FE-SEM of oxygen-annealed sample #2. (c) XRD patterns for both as-grown and annealed samples, with the dominant PbSe growth orientation observed along {100}.

SEM Analysis

As can be seen from cross-sectional FE-SEM (Figure 5-1 (a) and 1(b)) our VPD film both as-grown and annealed has a much smoother surface than that of the CBD-grown sample.[224] The total film thickness of 480nm and 689nm (Figure 5-1(a)) is confirmed by SEM for sample #1 and sample #2, respectively. It is worth noting that the striation marks on SiO_2 in Figure 5-1(b) are a result of the non-ideal cleavage of the film. Figure 5-2(a) and (b) show the Energy Dispersive Spectroscopy (EDS). The film in its as-grown state exhibits nearly identical atomic ratios of lead to selenium, along with some traces of cadmium. The morphological transition after oxygen annealing is attributed to the reshaping and recrystallization of PbSe/CdSe NCs, along with oxide formation in the crystal (Figure 5-1(b)) [102]. EDS analysis after annealing (Figure 5-2(b)) shows a significant increase in O_2 content and a decrease in Se content, indicating the escape of Se as gaseous SeO_2 or elemental selenium. The PbSe and CdSe reaction with oxygen at high

temperatures resulted in the creation of PbO, PbSeO3, PbSeO4, and CdO, which has been previously demonstrated through reactions 5-2 to 5-6 [163], [277], [278].

$$PbSe(s) + 1.5O_2(g) \rightarrow PbO(S) + SeO_2(g) \quad (5\text{-}2)$$

$$CdSe(s) + 1.5O_2(g) \rightarrow CdO(S) + SeO_2(g) \quad (5\text{-}3)$$

$$PbSe(s) + 1.5O_2(g) \rightarrow PbSeO_3(S) \quad (5\text{-}4)$$

$$PbSeO_3(s) + 0.5O_2(g) \rightarrow PbSeO_4(S) \quad (5\text{-}5)$$

$$PbSe(s) + 2O_2(g) \rightarrow PbSeO_4(S) \quad (5\text{-}6)$$

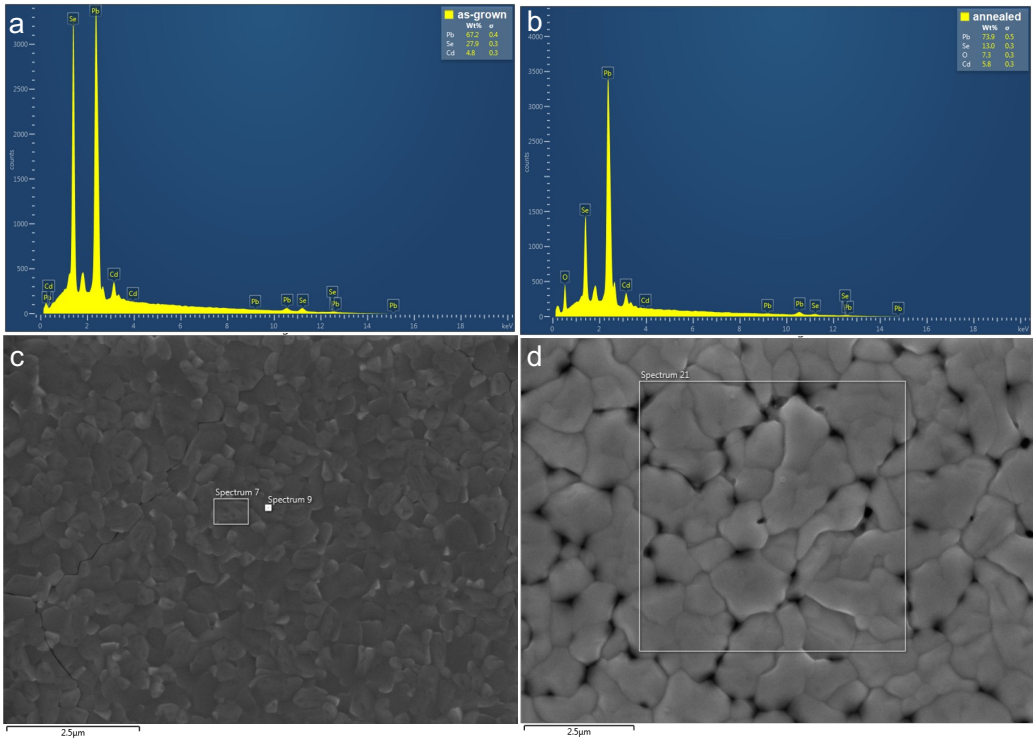


Figure 5-2 EDS images of as-grown and annealed. (a) (b) EDS image of the as-grown sample #2 showing peaks of lead, selenium, and cadmium. (b) EDS image of the annealed sample #2 displaying oxygen peaks. SEM image and EDS region of (c)as-grown film (Spectrum 7) and (d) annealed film (Spectrum 21).

Absorption, Photoluminescence, and Tauc Plot

Absorption and photoluminescence were analyzed via FTIR spectroscopy. The films on MWIR transparent sapphire and SiO_2/Si substrates (for both sample #1 and sample #2) were

annealed simultaneously to ensure consistent annealing conditions for studying absorption edge and absorbance. Figure 5-3 (b) and (c) show the absorption spectra for samples #1 and #2, respectively. The absorbance and transmission spectra are used to obtain the Tauc plot (Figure 5-3 (a)), revealing absorption edges of 0.33eV (3.75μm) for sample #1 and 0.31eV (4μm) for sample #2. These values exceed the bulk PbSe bandgap of 0.278eV (4.46μm), indicating the quantum confinement effect. The shorter PbSe growth duration in sample #1 (resulting in a smaller core size) led to a blue shift in the absorption edge compared to both sample #2 and bulk PbSe [251]. Both samples after annealing with oxygen exhibit strong photoluminescence at 3.35μm and 3.56μm (Figure 5-3 (b) and (c)). After annealing, both samples show significantly enhanced photoluminescence intensity, approximately 100 times higher for sample #1 and 88 times higher for sample #2 compared to the as-grown samples. This emphasizes the significance of oxygen in defect passivation, aligning with conclusions from previous research [82].

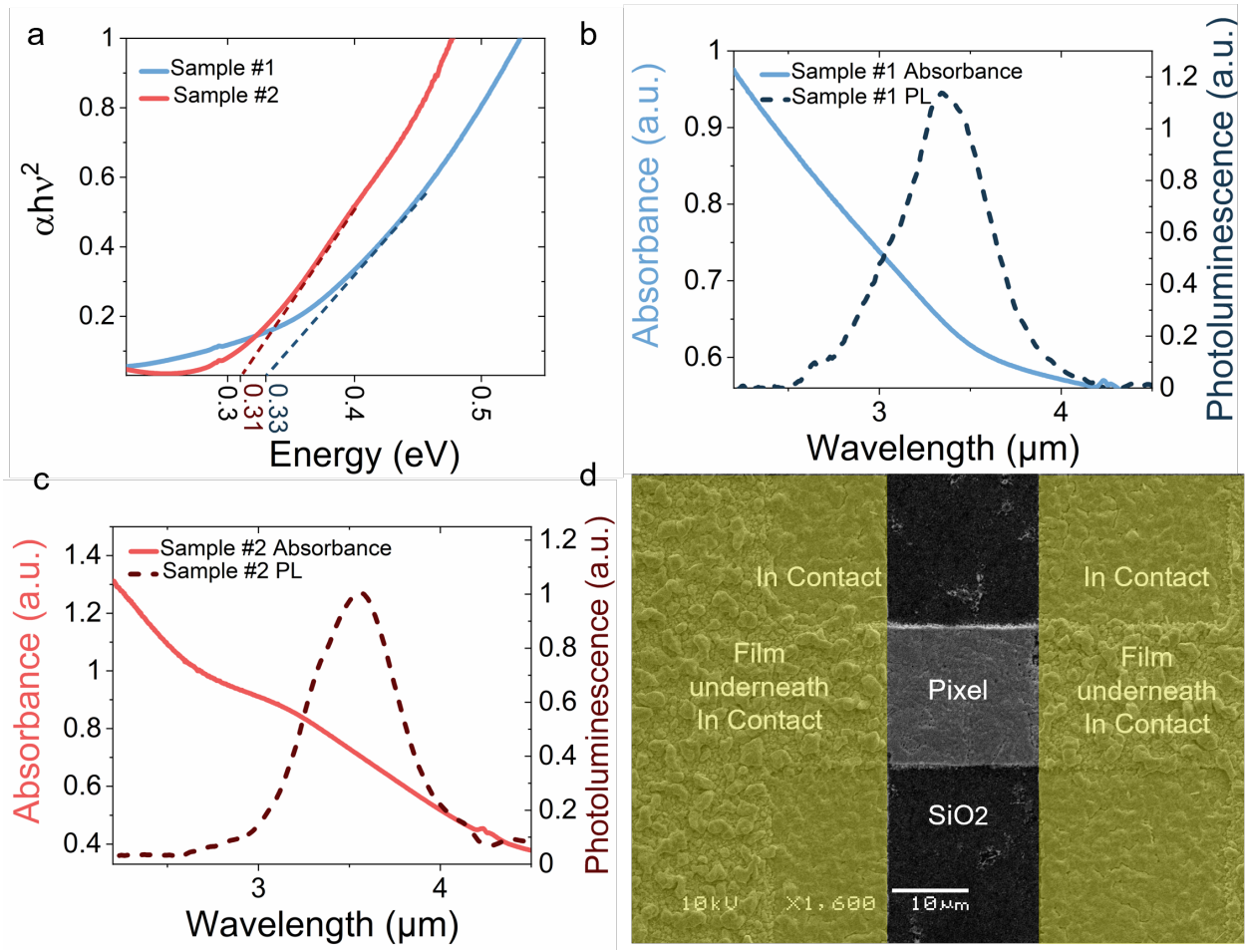


Figure 5-3 (a) Tauc plot for annealed PbSe/CdSe NC films revealing band edge absorption of 3.7μm and 4μm, respectively. (b), (c) Absorbance and photoluminescence of the annealed PbSe/CdSe NCs showing a photoluminescent peak of 3.35μm and 3.56μm for samples #1 and #2, respectively. (d) SEM topography of 17.5μm x 20μm pixel.

Pixel Fabrication

Positive photoresist photolithography patterns are applied to annealed samples for subsequent etching using reactive ion etching (RIE). The etching process operates at a rate of 50nm/min with an $Ar/CH_4/H_2$ ratio of 5/10/10. This etching recipe, originally tailored for PbSe [279], proves effective for this material system as well. The detector pixel is etched down to SiO_2 to delineate the active area. Following RIE, thermal deposition and lift-off techniques are employed to create

Indium contacts with a thickness of 450nm. As shown in Figure 5-3 (d), the detector area for top light illumination is 17.5μm x 20μm (350μm^2) with sideline ruggedness of about 0.5μm.

III. Results and Discussion

Electrical and Radiometric Measurement and Discussion

The dark current-voltage (I-V) measurements for pixels fabricated from both samples are illustrated in Figure 5-5(a). The linearity in the I-V curve suggests symmetrical contact formation between the film and indium, confirming film electrical homogeneity. The signal and noise measurements, conducted at a modulation frequency of 750Hz using a Locked-in amplifier, are depicted in Figure 5-5 (b). Photocurrent in PCs can be written as:

$$I_{ph} = g\eta q A_{det} \phi_s = EQE \times q A_{det} \phi_s, \quad (5\text{-}7)$$

Where I_{ph}, g, η, q, A_{det}, and Φ_s are photocurrent, photoconductive gain, quantum efficiency, electron charge, detector active area, and signal photon flux density. As shown in Figure 5-5(b), for both samples, the signal increases linearly with bias up to 0.8V (E= 400V/cm). Upon further increase in the electric field, the signal begins to saturate, an indication of sweep-out [90], [280]. Measured signal and noise are used to determine responsivity and D* of the detector, as shown below:

$$R = I_{ph}/P_{in}\ (A/W), \quad (5\text{-}8)$$

$$P_{in} = (A_{det} A_{BB} \beta / d^2) \times 2c^2 h \int_0^{\lambda_c} 1/(\lambda^5 (e^{hc/\lambda KT} - 1)) d\lambda, \quad (5\text{-}9)$$

$$D^* = (R/i_n) \times \sqrt{A_{det}\Delta f} = (I_{ph}/i_n) \times \sqrt{A_{det}\Delta f}/P_{in}, \quad (5\text{-}10)$$

Where R, P_{in}, and D* are responsivity and incident blackbody optical power up to the cut-off wavelength of each sample, and specific detectivity. Device active area (A_{det}=350μm^2), blackbody

aperture (A_{BB}=0.2cm^2), chopper modulation coefficient (β=0.45), Blackbody temperature (T=823K), blackbody to device distance (d=40cm), cut-off wavelength (λ_c=3.75 and 4μm), the noise current ($i_{n,}$ derived from noise voltage measured with locked-in amplifier, and respective sample resistance), and noise measurement bandwidth (Δf=1Hz) are used to calculate the R and D*. We use the absorption edge as the cutoff wavelength in this paper.

The blackbody responsivity along with External Quantum Efficiency (EQE) is depicted in Figure 5-5 (c). For detectors with 100% EQE under a blackbody illumination at 823K, the theoretical responsivity is 2.33A/W and 2.43A/W for cutoff wavelengths of 3.75μm (sample #1) and 4μm (sample #2), respectively. As shown in Figure 5-5 (c), both examples show over 100% EQE when bias voltages exceed a certain value. This is a clear indication of photoconductive gain. Based on the reference [281], we attribute the underlying gain mechanism to oxygen-related electron traps in our p-type film. The oxygen-related trap model [282], [283] is widely accepted for explaining photoconductive gain in Pb-salt PCs. Our sensitization process involving only oxygen supports this model. It suggests that oxygen-related traps significantly increase carrier lifetime, contributing to the photoconductive mechanism. However, a challenge remains: minority carrier traps alone cannot explain the over three orders of magnitude increase in resistivity. The barrier model [284] could potentially resolve this issue by adjusting barrier heights to match experimental resistivity. Typically, sensitizing PbSe PC films involves oxygen and iodine. Since Pb- and PbSe-oxides as well as Pb-iodides have larger bandgaps than PbSe, it's challenging to understand how these barriers achieve desired heights in the model. Furthermore, explaining high EQE becomes challenging if photogenerated carriers must traverse multiple potential barriers via thermionic emission. The charge separation model [89] explains the increase in resistivity and

carrier lifetime. Introducing oxygen traps at grain boundaries into this model can explain experimental observations, including the photoconductive gain of sensitized Pb-salt PCs.

As suggested in reference [102], annealing in oxygen may facilitate the formation of interconnected p-type PbSe and n-type CdSe, thus initiating the process of charge separation (5-4 (c)). There are multiple reports of PbSe/CdSe core/shell QD structures where, after annealing, the CdSe shell can break and reorganize into a Janus-like heteronanocrystal with PbSe, facilitating the melting of PbSe cores (Figure 5-4 (b)) [213], [250], [285]. Using the Scherrer equation to estimate crystallite size of PbSe and CdSe after annealing shows the PbSe crystallite size increased from 21.4 nm to 27.91 nm due to grain boundary growth and Ostwald Ripening [163], [275]. The CdSe crystallite size decreased from 71.1 nm to 58.04 nm, which supports the idea that the CdSe shell undergoes reconfiguration after annealing (Figure 5-4). Annealing at excessively high temperatures or for prolonged durations could result in the formation of thick oxides at the boundaries of PbSe and CdSe, hindering charge flow Figure 5-4 (d)) [102], [286]. Considering the observed photoconductive gain, we believe that oxygen-related electron traps are induced into the grain boundaries during the oxygen annealing. These traps capture minority electrons while allowing holes to transport, recombine in one contact and inject from the other contact. This process repeats τ_{life}/τ_{tr} times, preserving charge neutrality until the trapped electrons are released and thus generating photoconductive gain (Figure 5-4 (c)), where τ_{life} is carrier lifetime and τ_{tr} is the majority carrier transit time between electrodes. τ_{tr} can be calculated from $\tau_{tr=L^2/\mu V}$. Taking the measured Hall mobility of 9.49cm^2/V.s into account (Table 5-2), the carrier transit time at 0.8V and a device length (L) of 20μm would be 0.52μs. With EQE 218% at 0.8V for sample #1, the carrier lifetime is estimated to be 1.13μs. If carrier trapping serves as the predominant mechanism affecting response time, the detector response time is 1.13μs. When compared to the typical

response time range of commercial PbSe devices, which falls between 2 and 25μs [287], it's evident that the carrier lifetime enhancement due to traps does not adversely affect the device speed.

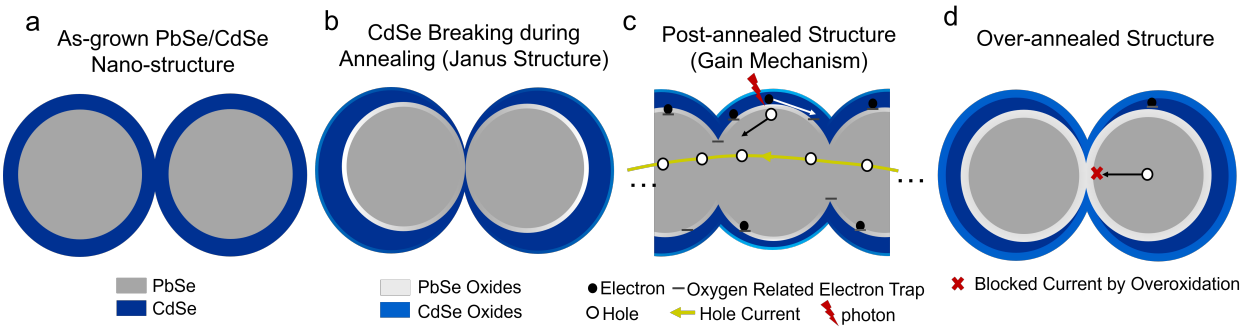


Figure 5-4 Schematic depicting the evolution and photoconduction mechanism of the material system: (a) As-grown PbSe/CdSe Core/Shell structure. (b) CdSe shell reorganization facilitating connections between PbSe cores and some oxide formation at boundaries. (c) Optimized structure with threaded PbSe cores enabling hole transportation, recombination, and injection of new holes while trapping minority electrons. (d) Over-annealed structure causing carrier blocking. Note: NC shapes may not be spherical.

Table 5-2 The Hall measurement for annealed sample #1 and #2

Sample		Carrier type	Mobility	Carrier Concentration
#1	As-grown	P-type	56.7	8.3×10^{17}
	Annealed	P-type	9.49	5.2×10^{16}
#2	As-grown	P-type	39.2	1.2×10^{18}
	Annealed	P-type	6.1	6.2×10^{16}

The blackbody Peak-D* is calculated using the method in reference [249] by assuming a sharp absorption edge. As shown in Figure 5-5(d), maximum D* is observed at 0.4V for both samples with calculated peak D* of $2.17\text{x}10^{10}$ Jones (blackbody D*=$7.5\text{x}10^{9}$) and $1.61\text{x}10^{10}$ Jones (blackbody D*=$5.56\text{x}10^{9}$), for sample #1 and sample #2, respectively. These D* values are

comparable to the best commercially available CBD-grown PbSe PCs [287], [288]. By factoring in the refractive index of PbSe and CdSe, roughly 30 % of light would be lost due to reflection. This reflection loss could be reduced by anti-reflection a coating [101], increasing D* to 9.75×10^9 and 7.2×10^9 Jones for samples #1 and #2, respectively. Assuming effective PbSe thickness (t) to be 320 nm for sample #1, and estimated absorption coefficient (α) of 8000cm^{-1} (at 0.33eV) [289], only 22% of MWIR light is absorbed. It's established that $D^* \propto (1 - e^{-\alpha t})/\sqrt{\alpha t}$ [290]. To optimize the signal-to-noise ratio, the thickness should ideally be $1.27/\alpha$, ignoring the interface reflection. In such case, for maximum signal-to-noise ratio, the PbSe thickness should be 1.57μm, resulting in a 48% increase in D*. However, it's important to note that achieving uniform sensitization for thicker films could be challenging.

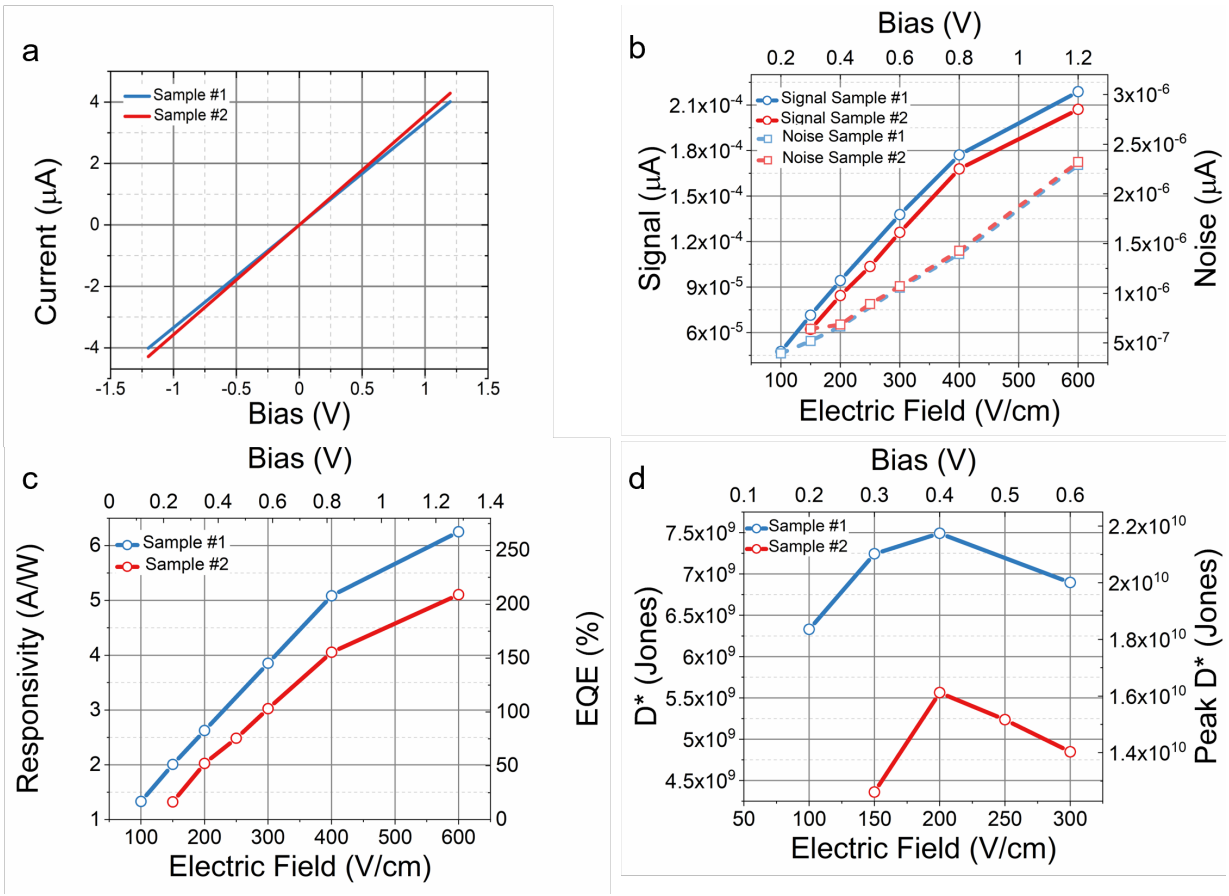


Figure 5-5. Radiometric and noise measurement of the device. (a) The dark current-voltage characteristics of both samples. (b) The signal and noise current of the devices under different bias voltages. (c) Responsivity and EQE, (d) specific detectivity, and peak specific detectivity of devices vs. different bias voltages.

The frequency-dependent noise was measured using an FFT spectrum analyzer in dark conditions, as shown in Figure 5-6 (a) for sample #2 (Similar results are also observed for sample #1). No knee frequency was observed in the measured frequency range of 1-1.56kHz, indicating dominance of 1/f noise. This aligns with observations in other reported Pb-salt PCs, where 1/f-like noise is the primary noise source [291]. At zero bias voltage, the measured noise floor corresponds to the Johnson noise level. Increasing the bias voltage results in higher current, causing the noise levels to rise accordingly. The root cause of 1/f noise has not been extensively studied in lead-salt PCs. The 1/f noise has been attributed to either mobility fluctuations [292], [293], [294] or

fluctuations in the barrier height resulting from carrier trapping at grain boundaries [295] aligning with a typical number-fluctuation model. Another root cause of 1/f noise is related to trapping and detrapping in the surface and bulk trap states. When carriers are captured and subsequently released (detrapped) from these traps, they cause fluctuations in the carrier population, leading to current or voltage noise [296], [297]. Since different trap states have varying trapping and detrapping times, these processes contribute to a broad range of frequency-dependent fluctuations, which manifest as 1/f noise. Moreover, the temporal dynamics of trapping and detrapping can also be influenced by the chopper frequency when light is periodically modulated, linking the observed noise behavior to the optical excitation conditions. Interestingly, the 1/f noise spectra in polycrystalline semiconductors still adhere to the empirical relation discovered by Hooge for a homogeneous semiconductor and resistor [23], [298], [299].

$$S_{i_n}(1/f) = \gamma \frac{I_d^{\beta}}{N_0 f^{\alpha}} \tag{5-11}$$

$S_{i_n}(1/f)$ is the power spectral density of the noise current (i_n^2), I_d is the mean value of dark current, and N_0 is the total number of charge carriers. γ is the Hooge coefficient. In the polycrystalline 1/f noise models, γ carries information on crystallites and interfaces [300]. α and β are fitting parameters with ideal values of 1 and 2, respectively, in scenarios where 1/f noise is the dominant mechanism. For an inhomogeneous semiconductor, values of β larger than 2 are observed [260], [299], [300]. If the measured Hall concentration of 6.2×10^{16} cm^{-3} (Table 5-2) is used to calculate N_0. Figure 5-6 (b) exhibits measured noise spectral density and fitted line for voltages of 0.4-1.2V. We found the range of α to be 1.02-1.03 under different bias voltages, indicating that 1/f noise predominates in our device. β is determined to be 2.01, suggesting that the VPD-process can produce much more uniform films compared to wet chemical approaches [50],

[260]. Additionally, γ is found to $3.2x10^{-3}$, falling within the typical range of non-single crystalline materials [298], [299].

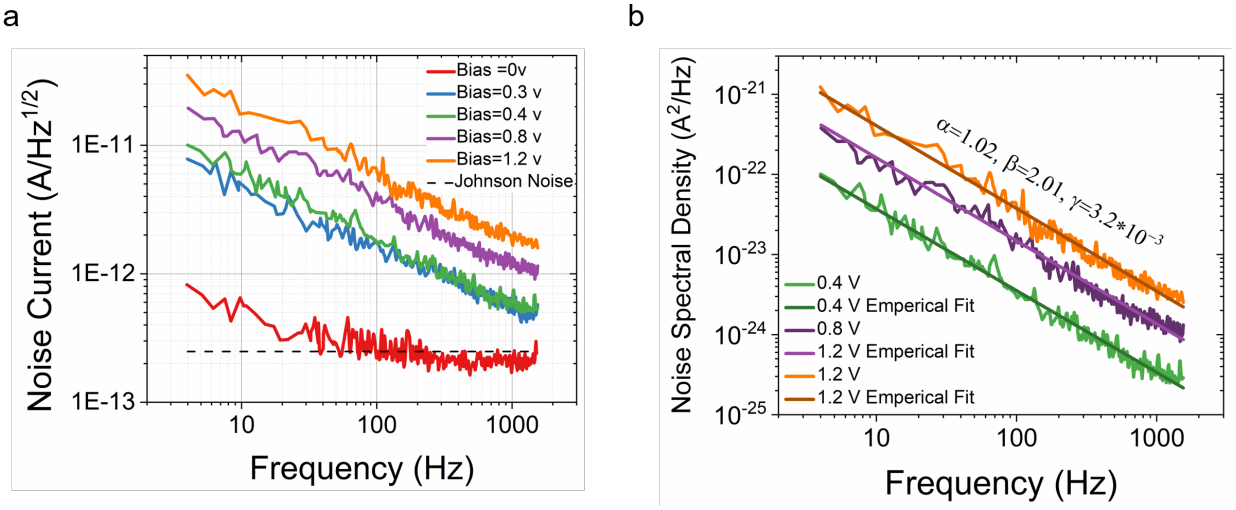


Figure 5-6 Spectral noise current (a), noise spectral density and analysis (b) of sample #2.

While VPD yields films with superior uniformity compared to CBD, annealing in oxygen-rich, high-temperature environments still causes surface roughening, which is detrimental for FPA PDs [82], [223]. Group's future work will explore alternative approaches to high-temperature oxygen annealing. Additionally, frequency modulation is essential for lead-salt photoconductors to mitigate 1/f noise, limiting the use of commercially available Si ROICs for high-performance FPA applications. Figure 5-7 depicts the D* measurements versus the modulation frequency for sample #2. The D* and Peak D* are calculated from measured spectral noise at different frequencies and 0.4V bias for sample #2. Due to the dominance of 1/f noise at lower modulation frequencies, the D* decreases rapidly from 5.97×10^{9} Jones to 2.57×10^{8} Jones as the frequency decreases from 835 Hz to 4 Hz. While the device still shows acceptable D* at near-DC modulation, it is not as high as preferred for imaging applications. Therefore, future efforts will concentrate on reducing 1/f noise.

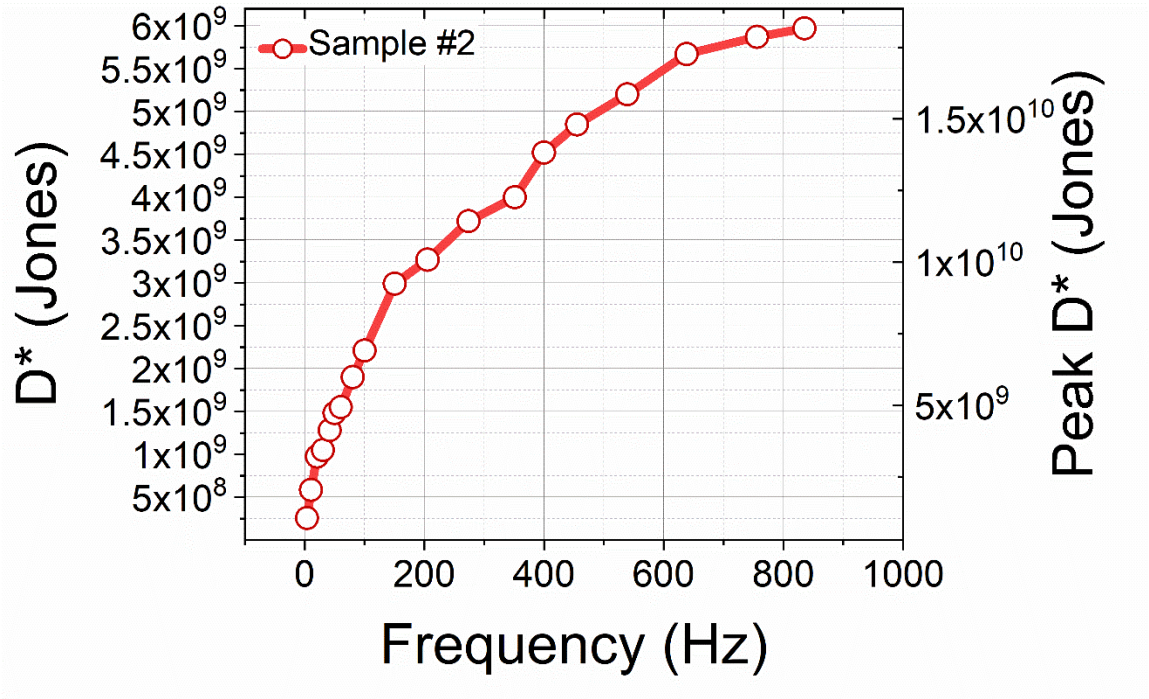


Figure 5-7 The D* and Peak D* versus modulation frequencies measured at 0.4V bias.

IV. Summary and Conclusion

In conclusion, we developed high-performance MWIR PbSe/CdSe heterostructure nanocrystal photoconductors on SiO_2/Si substrates using vapor phase deposition (VPD). By fine-tuning the growth conditions and employing oxygen annealing, we achieved tunable absorption edges at 3.75μm and 4.0μm. Our devices exhibited high morphological and electrical uniformity, as confirmed by SEM and noise analysis. This enhanced uniformity is crucial for achieving high-performance focal plane arrays (FPAs) in practical applications. The investigation into noise mechanisms revealed the dominance of 1/f noise, consistent with Hooge's empirical equation for homogeneous materials. Despite the presence of 1/f noise, the devices achieved external quantum EQE exceeding 100%, indicating significant photoconductive gain. This gain is attributed to oxygen-related electron traps, which enhance carrier lifetime and contribute to the observed high performance. The room-temperature peak D* of 2.17×10^{10} and 1.61×10^{10} Jones for pixels with

absorption edges at 3.75μm and 4.0μm, respectively, highlight the potential for VPD-grown PbSe/CdSe photoconductors in practical MWIR applications.

Chapter 6 Conclusion, Summary, and Future Directions

I. Summary and conclusion

This dissertation has charted a comprehensive and progressive investigation into the development of uncooled mid-wavelength infrared (MWIR) photodetectors based on lead selenide (PbSe), culminating in the demonstration of a high-performance, scalable, and manufacturable device architecture. The research trajectory systematically evolved from foundational materials science on epitaxial substrates to the fabrication of state-of-the-art nanostructured devices on industry-standard silicon substrates.

The work began in Chapter 3 with a fundamental exploration of epitaxial growth to overcome the inherent challenges of lattice and thermal mismatch. We demonstrated, for the first time, the successful growth of crack-free, monocrystalline n-type PbSe films on highly mismatched p-type vicinal Ge(100) substrates. The critical enabling technology was an *in-situ* selenium surface treatment that modified the adatom kinetics, suppressing 3D islanding and promoting layer-by-layer growth. The resulting n-PbSe/p-Ge heterojunction exhibited excellent diode characteristics, with a rectification factor exceeding 2,600 and a low reverse-bias current density, validating a new pathway for integrating PbSe with mature Group IV electronics for applications like dual-band SWIR/MWIR sensing. Building on this, we also achieved the first-ever epitaxial growth of single-phase cubic n-CdSe on p-PbSe. This was a significant materials science breakthrough, as *in-situ* RHEED monitoring confirmed that the CdSe growth proceeded layer-by-layer, adopting the cubic crystal structure of the PbSe seed layer rather than its typical hexagonal wurtzite phase. Both RHEED and XRD analysis confirmed the growth of a single-phase cubic CdSe film. This all-epitaxial, single-phase interface was critical: the resulting photovoltaic detector showed a clear photoresponse at room temperature (D* of 6.5×10^8 Jones) and,

significantly, exhibited the correct temperature-dependent behavior—improving performance upon cooling. This resolved the inverted temperature-dependence issues that had plagued previous polycrystalline CdSe/PbSe devices, which were compromised by mixed-phase (cubic and hexagonal) interfaces. This chapter established that meticulous interface and epitaxial engineering could produce high-quality PbSe-based heterojunctions with superior electronic properties.

Recognizing the cost and scalability limitations of epitaxial methods, the research pivoted in Chapter 4 to a more manufacturable approach: vapor phase deposition (VPD) on amorphous SiO_2/Si substrates. This work translated the PbSe/CdSe heterostructure concept into a nanostructured, polycrystalline photoconductor. The key finding was that a post-deposition oxygen annealing step is critical for device performance. We systematically optimized this annealing process, demonstrating that an ideal thermal budget (430°C) passivates defects and likely facilitates the formation of an interconnected 3D network of p-PbSe and n-CdSe, which enhances charge separation and carrier lifetime. This low-cost, large-area (2 mm x 2 mm) photoconductor achieved a promising uncooled peak D* of 2.49×10^9 Jones, proving the viability of the VPD-on-silicon platform.

Finally, Chapter 5 consolidated all previous findings to produce a device with state-of-the-art performance and features. By refining the VPD process, we demonstrated tunable cutoff wavelengths (3.75 μm and 4.0 μm) by controlling the PbSe nanocrystal core size via deposition time—a clear manifestation of the quantum confinement effect. More importantly, we scaled the devices down to small, FPA-compatible pixels (17.5×20 μm²) using standard photolithography and reactive ion etching. These small-pixel devices yielded a record uncooled peak D* of 2.17×10^{10} Jones, placing them in direct competition with the best commercial PbSe detectors. This high performance was linked to photoconductive gain (EQE > 100%), attributed to an oxygen-trap-

assisted charge separation mechanism. Crucially, noise analysis revealed that the dominant 1/f noise spectrum followed Hooge's empirical relation for homogeneous materials ($\beta \approx 2.01$). This finding is of profound significance, as it provides the first quantitative evidence that our VPD-grown nanostructured films are far more electrically uniform than conventional, non-uniform CBD-grown films, addressing a primary obstacle for large-format FPA production.

In summary, this dissertation established a complete pathway for uncooled PbSe MWIR photodetectors: from proving the fundamental quality of epitaxial heterojunctions (Ch. 3), to developing a scalable VPD-on-silicon process (Ch. 4), and ultimately demonstrating a highly uniform, quantum-tunable, small-pixel device with state-of-the-art performance (Ch. 5).

II. Future Directions:

The results presented in this dissertation establish a strong foundation for uncooled PbSe-based MWIR photodetectors and highlight several promising directions for further research. Building on the insights into epitaxial interface quality, defect control, and trap-assisted transport, the following paths are expected to advance both the scientific understanding and practical performance of IV–VI infrared detectors.

1. **Broadband bulk PbSe/ nanostructured PbSe/CdSe photodetector:** A promising future direction is the development of broadband PbSe-based photodetectors by integrating bulk PbSe and nanostructured PbSe/CdSe layers into a single heterostructure. Bulk PbSe, with its narrow bandgap and strong intrinsic absorption extending up to ~4.6 μm, can efficiently detect the mid-infrared portion of the spectrum, while nanostructured PbSe/CdSe layers—with quantum confinement–induced bandgap widening—can be engineered to absorb shorter wavelengths down to ~2 μm. By carefully controlling nanostructure size, shell thickness, and layer

composition, it is possible to tailor the spectral response of each region, enabling a broadband, room-temperature detector that spans the entire 2–4.6 μm range. Such a vertically graded or hybrid design would allow simultaneous detection of multiple spectral bands within a single device architecture, improving spectral selectivity and responsivity without the need for cooling. Future work should focus on optimizing the coupling between bulk and nanostructured regions to ensure efficient carrier transfer across interfaces while minimizing recombination, paving the way for compact, tunable, and cost-effective broadband MWIR photodetectors.

2. **Investigation and Mitigation of 1/f Noise in PbSe Photoconductors:** The strong photoconductive gain observed in the nanostructured PbSe/CdSe devices arises from trap-assisted carrier recycling, yet these same traps are also possible dominant source of 1/f noise, making it essential for future work to balance the beneficial and detrimental effects of trap states through deliberate trap-state engineering. This effort could include correlating trap lifetimes with gain and noise behavior by employing time-resolved photoconductivity measurements and low-frequency noise spectroscopy to directly link carrier trapping dynamics with photoconductive gain and flicker-noise mechanisms. At the materials level, advanced passivation strategies—such as annealing in alternative gas ambients like nitrogen or forming gas, or implementing targeted chemical passivation treatments such as mild halide exposure—could be explored to selectively neutralize or stabilize the interfacial and grain-boundary trap states most responsible for noise. In parallel, device-level engineering could investigate how pixel geometry influences trap-assisted fluctuations, since prior results indicate that both pixel size and layout significantly impact 1/f noise; systematically varying

pixel dimensions and shapes may uncover pathways to suppress noise through optimized device architecture. Together, these approaches will enable a deeper understanding of the interplay between trap physics, gain, and noise, guiding the design of PbSe/CdSe photodetectors with higher stability, lower noise, and improved room-temperature performance.

Funding

Throughout the dissertation period, this dissertation work was supported by the US army research office (ARO) under Grant No. W911NF-18-1-0418, and by the United States Air Force Lab under Contract No. FA2377-25-P-B008

References

[1] M. Razeghi and B.-M. Nguyen, "Advances in mid-infrared detection and imaging: a key issues review," *Rep. Prog. Phys.*, vol. 77, no. 8, p. 082401, Aug. 2014, doi: 10.1088/0034-4885/77/8/082401.

[2] A. Rogalski and K. Chrzanowski, "Infrared Devices And Techniques (Revision)," *Metrology and Measurement Systems*, vol. 21, no. 4, pp. 565–618, Dec. 2014, doi: 10.2478/mms-2014-0057.

[3] D. Jung, S. Bank, M. L. Lee, and D. Wasserman, "Next-generation mid-infrared sources," *J. Opt.*, vol. 19, no. 12, p. 123001, Dec. 2017, doi: 10.1088/2040-8986/aa939b.

[4] C. R. Petersen *et al.*, "Non-Destructive Subsurface Inspection of Marine and Protective Coatings Using Near- and Mid-Infrared Optical Coherence Tomography," *Coatings*, vol. 11, no. 8, p. 877, July 2021, doi: 10.3390/coatings11080877.

[5] I. Zorin, J. Kilgus, R. Su, B. Lendl, M. Brandstetter, and B. Heise, "Multimodal mid-infrared optical coherence tomography and spectroscopy for non-destructive testing and art diagnosis," in *Optics for Arts, Architecture, and Archaeology VII*, P. Targowski, R. Groves, and H. Liang, Eds., Munich, Germany: SPIE, July 2019, p. 22. doi: 10.1117/12.2528279.

[6] S. A. Kharitonov, D. Yates, R. A. Robbins, P. J. Barnes, R. Logan-Sinclair, and E. A. Shinebourne, "Increased nitric oxide in exhaled air of asthmatic patients," *The Lancet*, vol. 343, no. 8890, pp. 133–135, Jan. 1994, doi: 10.1016/S0140-6736(94)90931-8.

[7] M. Phillips *et al.*, "Volatile Markers of Breast Cancer in the Breath," *Breast Journal*, vol. 9, no. 3, pp. 184–191, May 2003, doi: 10.1046/j.1524-4741.2003.09309.x.

[8] W. Petrich, "MID-INFRARED AND RAMAN SPECTROSCOPY FOR MEDICAL DIAGNOSTICS," *Applied Spectroscopy Reviews*, vol. 36, no. 2–3, pp. 181–237, June 2001, doi: 10.1081/ASR-100106156.

[9] S.-S. Kim, C. Young, B. Vidakovic, S. G. A. Gabram-Mendola, C. W. Bayer, and B. Mizaikoff, "Potential and Challenges for Mid-Infrared Sensors in Breath Diagnostics," *IEEE Sensors J.*, vol. 10, no. 1, pp. 145–158, Jan. 2010, doi: 10.1109/JSEN.2009.2033940.

[10] S. P. Quanz *et al.*, "Atmospheric characterization of terrestrial exoplanets in the mid-infrared: biosignatures, habitability, and diversity," *Exp Astron*, vol. 54, no. 2–3, pp. 1197–1221, Dec. 2022, doi: 10.1007/s10686-021-09791-z.

[11] D. Popa and F. Udrea, "Towards Integrated Mid-Infrared Gas Sensors," *Sensors*, vol. 19, no. 9, p. 2076, May 2019, doi: 10.3390/s19092076.

[12] S. B. Hafiz, M. Scimeca, A. Sahu, and D.-K. Ko, "Colloidal quantum dots for thermal infrared sensing and imaging," *Nano Convergence*, vol. 6, no. 1, p. 7, Dec. 2019, doi: 10.1186/s40580-019-0178-1.

[13] Y. Zhang *et al.*, "Ultrasensitive photodetectors exploiting electrostatic trapping and percolation transport," *Nat Commun*, vol. 7, no. 1, p. 11924, June 2016, doi: 10.1038/ncomms11924.

[14] G. Konstantatos *et al.*, “Ultrasensitive solution-cast quantum dot photodetectors,” *Nature*, vol. 442, no. 7099, pp. 180–183, July 2006, doi: 10.1038/nature04855.

[15] J. P. Clifford, G. Konstantatos, K. W. Johnston, S. Hoogland, L. Levina, and E. H. Sargent, “Fast, sensitive and spectrally tuneable colloidal-quantum-dot photodetectors,” *Nature Nanotech*, vol. 4, no. 1, pp. 40–44, Jan. 2009, doi: 10.1038/nnano.2008.313.

[16] B. N. Pal, I. Robel, A. Mohite, R. Laocharoensuk, D. J. Werder, and V. I. Klimov, “High-Sensitivity p–n Junction Photodiodes Based on PbS Nanocrystal Quantum Dots,” *Adv Funct Materials*, vol. 22, no. 8, pp. 1741–1748, Apr. 2012, doi: 10.1002/adfm.201102532.

[17] N. Li, Z. Lan, L. Cai, and F. Zhu, “Advances in solution-processable near-infrared phototransistors,” *J. Mater. Chem. C*, vol. 7, no. 13, pp. 3711–3729, 2019, doi: 10.1039/C8TC06078A.

[18] “Review of photodetectors characterization methods,” *Bulletin of the Polish Academy of Sciences Technical Sciences*, Nov. 2023, doi: 10.24425/bpasts.2022.140534.

[19] L. Dou *et al.*, “Solution-processed hybrid perovskite photodetectors with high detectivity,” *Nat Commun*, vol. 5, no. 1, p. 5404, Nov. 2014, doi: 10.1038/ncomms6404.

[20] K. Shen *et al.*, “Enhanced performance of ZnO nanoparticle decorated all-inorganic $CsPbBr_3$ quantum dot photodetectors,” *J. Mater. Chem. A*, vol. 7, no. 11, pp. 6134–6142, 2019, doi: 10.1039/C9TA00230H.

[21] Y. Wei *et al.*, “Hybrid Organic/PbS Quantum Dot Bilayer Photodetector with Low Dark Current and High Detectivity,” *Adv Funct Materials*, vol. 28, no. 11, p. 1706690, Mar. 2018, doi: 10.1002/adfm.201706690.

[22] R. Guo, M. Zhang, J. Ding, A. Liu, F. Huang, and M. Sheng, “Advances in colloidal quantum dot-based photodetectors,” *J. Mater. Chem. C*, vol. 10, no. 19, pp. 7404–7422, 2022, doi: 10.1039/D2TC00219A.

[23] F. N. Hooge, “$1/f$ noise is no surface effect,” *Physics Letters A*, vol. 29, no. 3, pp. 139–140, Apr. 1969, doi: 10.1016/0375-9601(69)90076-0.

[24] Z. Wu, Y. Ou, M. Cai, Y. Wang, R. Tang, and Y. Xia, “Short-Wave Infrared Photodetectors and Imaging Sensors Based on Lead Chalcogenide Colloidal Quantum Dots,” *Advanced Optical Materials*, vol. 11, no. 1, p. 2201577, Jan. 2023, doi: 10.1002/adom.202201577.

[25] D. Panos G. and N. V. Lavrik, “Detectors—Figures of merit,” *Encyclopedia of Optical Engineering*. in 349, no. 57. 2003. Accessed: Nov. 26, 2023. [Online]. Available: https://123.physics.ucdavis.edu/week_6_files/detectors_figures_of_merit.pdf

[26] “MCT heterostructures for higher operating temperature infrared detectors designed in Poland,” *Opto-Electronics Review*, Jan. 2024, doi: 10.24425/opelre.2023.144551.

[27] O. Gravrand *et al.*, “Latest achievements on MCT IR detectors for space and science imaging,” presented at the SPIE Defense + Security, B. F. Andresen, G. F. Fulop, C. M. Hanson, J. L. Miller, and P. R. Norton, Eds., Baltimore, Maryland, United States, May 2016, p. 98191W. doi: 10.1117/12.2228456.

[28] N. C. Mansfield *et al.*, “Room temperature mid-wave infrared guided mode resonance InAsSb photodetectors,” *Applied Physics Letters*, vol. 125, no. 17, p. 171107, Oct. 2024, doi: 10.1063/5.0238913.

[29] “MCT’S ADVANTAGES AS AN INFRARED IMAGING.” Leonardo DRS. Accessed: Sept. 02, 2025. [Online]. Available: https://www.leonardodrs.com/wp-content/uploads/2023/08/201306_advantages_of_mct.pdf

[30] H. Lutz, R. Breiter, H. Figgemeier, T. Schallenberg, W. Schirmacher, and R. Wollrab, “Improved high operating temperature MCT MWIR modules,” presented at the SPIE Defense + Security, B. F. Andresen, G. F. Fulop, C. M. Hanson, and P. R. Norton, Eds., Baltimore, Maryland, USA, June 2014, p. 90701D. doi: 10.1117/12.2050427.

[31] VIGO PHOTONICS, “HgCdTe Photovoltaic IR Detectors.” Accessed: Sept. 07, 2025. [Online]. Available: https://vigophotonics.com/products/infrared-detectors/hgcdte-mct-photovoltaic-detectors/

[32] Teledyne, “Photovoltaic Mercury Cadmium Telluride Detectors.”

[33] E. A. Plis, “InAs/GaSb Type-II Superlattice Detectors,” *Advances in Electronics*, vol. 2014, pp. 1–12, Apr. 2014, doi: 10.1155/2014/246769.

[34] D. Z. Ting *et al.*, “InAs/InAsSb Type-II Strained-Layer Superlattice Infrared Photodetectors,” *Micromachines*, vol. 11, no. 11, p. 958, Oct. 2020, doi: 10.3390/mi11110958.

[35] D. Kwan, M. Kesaria, E. A. Anyebe, and D. Huffaker, “Recent trends in 8–14 μm type-II superlattice infrared detectors,” *Infrared Physics & Technology*, vol. 116, p. 103756, Aug. 2021, doi: 10.1016/j.infrared.2021.103756.

[36] M. Walther *et al.*, “Industrialization of type-II superlattice infrared detector technology at Fraunhofer IAF,” in *Infrared Technology and Applications XLV*, G. F. Fulop, C. M. Hanson, and B. F. Andresen, Eds., Baltimore, United States: SPIE, May 2019, p. 12. doi: 10.1117/12.2518424.

[37] L. Nordin, A. J. Muhowski, and D. Wasserman, “High operating temperature plasmonic infrared detectors,” *Applied Physics Letters*, vol. 120, no. 10, p. 101103, Mar. 2022, doi: 10.1063/5.0077456.

[38] A. Kamboj, L. Nordin, A. J. Muhowski, D. Woolf, and D. Wasserman, “Room-Temperature Mid-Wave Infrared Guided-Mode Resonance Detectors,” *IEEE Photon. Technol. Lett.*, vol. 34, no. 11, pp. 615–618, June 2022, doi: 10.1109/LPT.2022.3175110.

[39] L. She *et al.*, “Mid-wave infrared p+-B-n InAs/InAsSb type-II superlattice photodetector with an AlAsSb/InAsSb superlattice barrier,” *Infrared Physics & Technology*, vol. 121, p. 104015, Mar. 2022, doi: 10.1016/j.infrared.2021.104015.

[40] “Type-II superlattice unipolar barrier infrared detectors,” in *Semiconductors and Semimetals*, vol. 118, Elsevier, 2025, pp. 1–63. doi: 10.1016/bs.semsem.2025.05.003.

[41] L. Nordin, P. Petluru, A. Kamboj, A. J. Muhowski, and D. Wasserman, “Ultra-thin plasmonic detectors,” *Optica*, vol. 8, no. 12, p. 1545, Dec. 2021, doi: 10.1364/OPTICA.438039.

[42] S.-Y. Ahn *et al.*, “Enhanced broadband quantum efficiency in LWIR T2SL detectors with guided-mode resonance structure,” *Opt. Express*, vol. 33, no. 2, p. 1898, Jan. 2025, doi: 10.1364/OE.543617.

[43] S. Purkait *et al.*, “Lateral Cavity-Enhanced Guided Mode Resonance Structures for Mid-wave Infrared Photodetector Pixels,” Apr. 02, 2025, *arXiv*: arXiv:2504.02056. doi: 10.48550/arXiv.2504.02056.

[44] TELEDYNE, “T2SL Room Temperature.” Accessed: Oct. 02, 2025. [Online]. Available: https://www.teledynevisionsolutions.com/products/t2sl-room-temperature/?model=J24-5400-18C-R01M&vertical=tvs-judson-general&segment=tvs

[45] L3Harris, “SPIE Defense + Commercial Sensing | L3Harris® Fast. Forward.” Accessed: Oct. 03, 3035. [Online]. Available: https://www.l3harris.com/events/trade-show/spie-defense-commercial-sensing-0

[46] R. A. Jones, J. Blevins, S. Allen, D. Chmielewski, and R. Fink, “L3Harris advancements in large format type II superlattice FPA technology,” in *Infrared Technology and Applications LI*, D. Z. Ting, G. F. Fulop, M. Kimata, and M. H. MacDougal, Eds., Orlando, United States: SPIE, May 2025, p. 23. doi: 10.1117/12.3053979.

[47] V. Daumer *et al.*, “Type-II superlattices: a promising material for space applications,” in *International Conference on Space Optics — ICSO 2018*, N. Karafolas, Z. Sodnik, and B. Cugny, Eds., Chania, Greece: SPIE, July 2019, p. 234. doi: 10.1117/12.2536154.

[48] A. Rogalski, *Infrared and Terahertz Detectors*, 3rd ed. CRC Press, 2019. Accessed: May 27, 2025. [Online]. Available: https://books.google.com/books?hl=en&lr=&id=JTqDDwAAQBAJ&oi=fnd&pg=PP1&dq=Rogalski,+A.+(2020).+Infrared+and+Terahertz+Detectors+(3rd+ed.).+CRC+Press.&ots=m3aFY3IgKv&sig=R46QeaKB4XC6ql1Ovdkb0BX88lY#v=onepage&q=Rogalski%2C%20A.%20(2020).%20Infrared%20and%20Terahertz%20Detectors%20(3rd%20ed.).%20CRC%20Press.&f=false

[49] A. Rogalski, “Recent progress in infrared detector technologies,” *Infrared Physics & Technology*, vol. 54, no. 3, pp. 136–154, May 2011, doi: 10.1016/j.infrared.2010.12.003.

[50] M. M. Al Mahfuz *et al.*, “Mid-wavelength infrared photoconductive film synthesized from PbSe molecular ink,” *Applied Physics Letters*, vol. 123, no. 20, p. 203301, Nov. 2023, doi: 10.1063/5.0179127.

[51] P. Martyniuk and A. Rogalski, “HOT infrared photodetectors,” *Opto-Electronics Review*, vol. 21, no. 2, Jan. 2013, doi: 10.2478/s11772-013-0090-x.

[52] M. Rastkar Mirzaei and Z. Shi, “High-performance uncooled PbSe/CdSe nanostructured mid-infrared photodetector with tunable cutoff wavelength,” *Applied Physics Letters*, vol. 125, no. 8, p. 083501, Aug. 2024, doi: 10.1063/5.0223178.

[53] L. L. McDowell, J. Qiu, M. R. Mirzaei, B. Weng, and Z. Shi, “Integration of Epitaxial IV–VI Pb-Chalcogenide on Group IV Vicinal Ge Substrate to Form p–n Heterogeneous Structures,” *Crystal Growth & Design*, vol. 22, no. 1, pp. 461–468, Jan. 2022, doi: 10.1021/acs.cgd.1c01074.

[54] H. Hu, C. Deng, K. Zhang, M. Sun, H. Xuan, and S. Kong, “Novel two-dimensional lead sulfide quadrangular pyramid-aggregated arrays with self-supporting structure prepared at room temperature,” *Materials Science in Semiconductor Processing*, vol. 16, no. 6, pp. 1566–1572, Dec. 2013, doi: 10.1016/j.mssp.2013.06.003.

[55] R. Leitsmann *et al.*, “Structural and electronic properties of PbTe (rocksalt)/CdTe (zinc-blende) interfaces,” *Applied Surface Science*, vol. 254, no. 1, pp. 397–400, Oct. 2007, doi: 10.1016/j.apsusc.2007.07.099.

[56] S.-H. Wei and A. Zunger, “Electronic and structural anomalies in lead chalcogenides,” *Phys. Rev. B*, vol. 55, no. 20, pp. 13605–13610, May 1997, doi: 10.1103/PhysRevB.55.13605.

[57] Z. M. Gibbs *et al.*, “Temperature dependent band gap in PbX (X = S, Se, Te),” *Applied Physics Letters*, vol. 103, no. 26, p. 262109, Dec. 2013, doi: 10.1063/1.4858195.

[58] Yu. I. Ravich, B. A. Efimova, and I. A. Smirnov, *Semiconducting Lead Chalcogenides*. Boston, MA: Springer US, 1970. doi: 10.1007/978-1-4684-8607-0.

[59] S. L. Elizondo *et al.*, “Dielectric Charge Screening of Dislocations and Ionized Impurities in PbSe and MCT,” *Journal of Elec Materi*, vol. 37, no. 9, pp. 1411–1414, Sept. 2008, doi: 10.1007/s11664-008-0418-3.

[60] I. Melngailis and T. C. Harman, “Chapter 4 Single-Crystal Lead-Tin Chalcogenides,” in *Semiconductors and Semimetals*, vol. 5, Elsevier, 1970, pp. 111–174. doi: 10.1016/S0080-8784(08)62815-X.

[61] A. Rogalski, “History of infrared detectors,” *Opto-Electronics Review*, vol. 20, no. 3, Jan. 2012, doi: 10.2478/s11772-012-0037-7.

[62] A. Pastor, “Infrared guidance systems. A review of two man-portable defense applications,” Sept. 02, 2020, *Open Science Framework*. doi: 10.31219/osf.io/c6gxf.

[63] A. Rogalski, “Infrared detectors: status and trends,” *Progress in Quantum Electronics*, vol. 27, no. 2–3, pp. 59–210, Jan. 2003, doi: 10.1016/S0079-6727(02)00024-1.

[64] D. A. Kondas, “INTRODUCTION TO LEAD SALT INFRARED DETECTORS,” U.S. ARMY ARMAMENT RESEARCH, DEVELOPMENT AND ENGINEERING CENTER, Technical Report ARFSD-TR-92024, Feb. 1993. Accessed: May 27, 2025. [Online]. Available: https://apps.dtic.mil/sti/tr/pdf/ADA260781.pdf

[65] R. Ashokan, T. Lee, J. Zhao, and Y. Chang, “MERCURY CADMIUM TELLURIDE FOR HIGH OPERATING TEMPERATURE INFRARED DETECTORS,” University of Illinois at Chicago, Army Research Laboratory, 2004. Accessed: Oct. 06, 2025. [Online]. Available: https://apps.dtic.mil/sti/tr/pdf/ADA433522.pdf

[66] X. Zhang, J.-X. Shen, and C. G. Van De Walle, “Anomalous Auger Recombination in PbSe,” *Phys. Rev. Lett.*, vol. 125, no. 3, p. 037401, July 2020, doi: 10.1103/PhysRevLett.125.037401.

[67] Xu Xiang-Yan, Ye Zhen-Hua, Li Zhi-Feng, Lu Wei, and 中国科学院上海技术物理研究所,红外物理国家重点实验室,上海 200083, “Optimizing modeling of two-color middle

wavelength infrared photovoltaic HgCdTe detectors," *Acta Phys. Sin.*, vol. 56, no. 5, p. 2882, 2007, doi: 10.7498/aps.56.2882.

[68] Y. Jiang, M. C. Teich, and W. I. Wang, "Carrier lifetimes and threshold currents in HgCdTe double heterostructure and multi-quantum-well lasers," *Journal of Applied Physics*, vol. 69, no. 10, pp. 6869–6875, May 1991, doi: 10.1063/1.347676.

[69] C. CIRLOGANU, "EXPERIMENTAL AND THEORETICAL APPROACHES TO CHARACTERIZATION OF ELECTRONIC NONLINEARITIES IN DIRECT-GAP SEMICONDUCTORS," University of Central Florida, Orlando, Florida, 2010. Accessed: Nov. 13, 2025. [Online]. Available: https://www.researchgate.net/publication/264853110_EXPERIMENTAL_AND_THEORETICAL_APPROACHES_TO_CHARACTERIZATION_OF_ELECTRONIC_NONLINEARITIES_IN_DIRECT-GAP_SEMICONDUCTORS

[70] E. Kioupakis, D. Steiauf, P. Rinke, K. T. Delaney, and C. G. Van De Walle, "First-principles calculations of indirect Auger recombination in nitride semiconductors," *Phys. Rev. B*, vol. 92, no. 3, p. 035207, July 2015, doi: 10.1103/PhysRevB.92.035207.

[71] H. J. Haugan, G. J. Brown, B. V. Olson, E. A. Kadlec, J. K. Kim, and E. A. Shaner, "Minority carrier lifetimes in very long-wave infrared InAs/GaInSb superlattices," *Journal of Vacuum Science & Technology B, Nanotechnology and Microelectronics: Materials, Processing, Measurement, and Phenomena*, vol. 34, no. 2, p. 02L104, Mar. 2016, doi: 10.1116/1.4941132.

[72] S. P. Svensson, D. Donetsky, D. Wang, P. Maloney, and G. Belenky, "Carrier lifetime measurements in InAs/GaSb strained layer superlattice structures," presented at the SPIE Defense, Security, and Sensing, B. F. Andresen, G. F. Fulop, and P. R. Norton, Eds., Orlando, Florida, Apr. 2010, p. 76601V. doi: 10.1117/12.849514.

[73] J. R. Meyer *et al.*, "Comparison of Auger Coefficients in Type I and Type II Quantum Well Midwave Infrared Lasers," *IEEE J. Quantum Electron.*, vol. 57, no. 5, pp. 1–10, Oct. 2021, doi: 10.1109/JQE.2021.3096219.

[74] R. Klann, T. Höfer, R. Buhleier, T. Elsaesser, and J. W. Tomm, "Fast recombination processes in lead chalcogenide semiconductors studied via transient optical nonlinearities," *Journal of Applied Physics*, vol. 77, no. 1, Art. no. 1, Jan. 1995, doi: 10.1063/1.359388.

[75] P. C. Findlay *et al.*, "Auger recombination dynamics of lead salts under picosecond free-electron-laser excitation," *Phys. Rev. B*, vol. 58, no. 19, Art. no. 19, Nov. 1998, doi: 10.1103/PhysRevB.58.12908.

[76] O. Ziep, M. Mocker, D. Genzow, and K. H. Herrmann, "Auger recombination in PbSnTe-like semiconductors," *Phys. Stat. Sol. (b)*, vol. 90, no. 1, Art. no. 1, Nov. 1978, doi: 10.1002/pssb.2220900121.

[77] E. R. Youngdale *et al.*, "Auger lifetime enhancement in InAs–Ga $_{1-x}$ In $_{x}$ Sb superlattices," *Appl. Phys. Lett.*, vol. 64, no. 23, Art. no. 23, June 1994, doi: 10.1063/1.111325.

[78] J. R. Meyer *et al.*, "Auger coefficients in type-II InAs/Ga1−xInxSb quantum wells," *Appl. Phys. Lett.*, vol. 73, no. 20, Art. no. 20, Nov. 1998, doi: 10.1063/1.122609.

[79] C. M. Ciesla *et al.*, “Auger recombination dynamics of Hg0.795Cd0.205Te in the high excitation regime,” *Appl. Phys. Lett.*, vol. 71, no. 4, Art. no. 4, July 1997, doi: 10.1063/1.119588.

[80] A. R. Beattie and A. M. White, “An analytic approximation with a wide range of applicability for electron initiated Auger transitions in narrow-gap semiconductors,” *J. Appl. Phys.*, vol. 79, no. 2, Art. no. 2, 1996, doi: 10.1063/1.360828.

[81] Y. X. Ren, T. J. Dai, W. B. Luo, and X. Z. Liu, “Evidences of sensitization mechanism for PbSe thin films photoconductor,” *Vacuum*, vol. 149, pp. 190–194, Mar. 2018, doi: 10.1016/j.vacuum.2017.12.017.

[82] F. Zhao, S. Mukherjee, J. Ma, D. Li, S. L. Elizondo, and Z. Shi, “Influence of oxygen passivation on optical properties of PbSe thin films,” *Applied Physics Letters*, vol. 92, no. 21, p. 211110, May 2008, doi: 10.1063/1.2938417.

[83] M. Yu *et al.*, “Effect of oxygen and nitrogen sensitization on structural, optical and electrical properties of PbSe thin films,” *Thin Solid Films*, vol. 787, p. 140143, Dec. 2023, doi: 10.1016/j.tsf.2023.140143.

[84] M.-H. Jang *et al.*, “Photoconductive mechanism of IR-sensitive iodized PbSe thin films via strong hole–phonon interaction and minority carrier diffusion,” *Appl. Opt.*, vol. 59, no. 33, p. 10228, Nov. 2020, doi: 10.1364/AO.403641.

[85] S. Ganguly, M.-H. Jang, Y. Tan, S.-S. Yoo, M. C. Gupta, and A. W. Ghosh, “A multiscale materials-to-systems modeling of polycrystalline PbSe photodetectors,” *Journal of Applied Physics*, vol. 126, no. 14, p. 143103, Oct. 2019, doi: 10.1063/1.5087818.

[86] J. T. Harrison and M. C. Gupta, “Photoconductive PbSe thin films and the role of potassium iodide,” *Journal of Alloys and Compounds*, vol. 905, p. 164155, June 2022, doi: 10.1016/j.jallcom.2022.164155.

[87] D. Gao *et al.*, “PbSe sensitized with iodine and oxygen for high-performance photoelectronic detection,” *Materials Science in Semiconductor Processing*, vol. 190, p. 109327, May 2025, doi: 10.1016/j.mssp.2025.109327.

[88] A. Carbone and P. Mazzetti, “Grain-boundary effects on photocurrent fluctuations in polycrystalline photoconductors,” *Phys. Rev. B*, vol. 57, no. 4, pp. 2454–2460, Jan. 1998, doi: 10.1103/PhysRevB.57.2454.

[89] L. Zhao, J. Qiu, B. Weng, C. Chang, Z. Yuan, and Z. Shi, “Understanding sensitization behavior of lead selenide photoconductive detectors by charge separation model,” *Journal of Applied Physics*, vol. 115, no. 8, p. 084502, Feb. 2014, doi: 10.1063/1.4867038.

[90] S. Jost, “Identifying the physical mechanisms of polycrystalline lead salt photoconductors,” *Journal of Applied Physics*, vol. 132, no. 6, p. 064503, Aug. 2022, doi: 10.1063/5.0098505.

[91] B. Weng, J. Qiu, L. Zhao, Z. Yuan, C. Chang, and Z. Shi, “Recent development on the uncooled mid-infrared PbSe detectors with high detectivity,” presented at the SPIE OPTO, M. Razeghi, E. Tournié, and G. J. Brown, Eds., San Francisco, California, United States, Dec. 2013, p. 899311. doi: 10.1117/12.2041276.

[92] J. T. Harrison and M. C. Gupta, “Mechanistic studies of oxidation and iodization of PbSe thin film sensitization for mid-infrared detection,” *Journal of Applied Physics*, vol. 131, no. 2, p. 025308, Jan. 2022, doi: 10.1063/5.0077053.

[93] M.-H. Jang, S.-S. Yoo, M. T. Kramer, N. K. Dhar, and M. C. Gupta, “Electrical transport properties of sensitized PbSe thin films for IR imaging sensors,” *Semicond. Sci. Technol.*, vol. 34, no. 6, p. 065009, June 2019, doi: 10.1088/1361-6641/ab19e7.

[94] M. C. Gupta, J. T. Harrison, and M. T. Islam, “Photoconductive PbSe thin films for infrared imaging,” *Mater. Adv.*, vol. 2, no. 10, pp. 3133–3160, 2021, doi: 10.1039/D0MA00965B.

[95] L. L. McDowell, M. Rastkar Mirzaei, and Z. Shi, “Epitaxial CdSe/PbSe Heterojunction Growth and MWIR Photovoltaic Detector,” *Materials*, vol. 16, no. 5, p. 1866, Feb. 2023, doi: 10.3390/ma16051866.

[96] R. Schwanninger *et al.*, “Highly Responsive Mid-Infrared Metamaterial Enhanced Heterostructure Photodetector Formed out of Sintered PbSe/PbS Colloidal Quantum Dots,” *ACS Appl. Mater. Interfaces*, vol. 15, no. 8, pp. 10847–10857, Mar. 2023, doi: 10.1021/acsami.2c23050.

[97] G. Zhang *et al.*, “Lead Selenide Thin Films and Uncooled Midinfrared Detectors by Vapor Phase Deposition,” *J. Phys. Chem. Lett.*, vol. 13, no. 48, pp. 11176–11182, Dec. 2022, doi: 10.1021/acs.jpclett.2c03418.

[98] “PbS Detectors,” Laser Components. Accessed: May 29, 2025. [Online]. Available: https://www.lasercomponents.com/us/product/pbs-detectors/

[99] “PbS Detectors,” OPTO DIODE. Accessed: May 29, 2025. [Online]. Available: https://optodiode.com/product-category/pbs/

[100] “PbSe Detectors,” Laser Components. Accessed: May 29, 2025. [Online]. Available: https://www.lasercomponents.com/us/product/pbse-detectors/

[101] B. Weng, J. Qiu, Z. Yuan, P. R. Larson, G. W. Strout, and Z. Shi, “Responsivity enhancement of mid-infrared PbSe detectors using CaF_2 nano-structured antireflective coatings,” *Appl. Phys. Lett.*, vol. 104, no. 2, p. 021109, Jan. 2014, doi: 10.1063/1.4861186.

[102] M. Rastkar Mirzaei and Z. Shi, “Room-temperature nanostructured PbSe/CdSe mid-infrared photodetector: Annealing effects,” *Journal of Vacuum Science & Technology B*, vol. 42, no. 1, p. 012204, Jan. 2024, doi: 10.1116/6.0003193.

[103] J. Qiu, Y. Liu, G. Zhang, K. Shi, Y. Li, and Y. Luo, “Modified vapor phase deposition technology for high-performance uncooled MIR PbSe detectors,” *RSC Adv.*, vol. 11, no. 55, pp. 34908–34914, 2021, doi: 10.1039/D1RA06144E.

[104] “LEPTON uncooled detector,” New Infrared Technologies. Accessed: May 29, 2025. [Online]. Available: https://www.niteurope.com/single-infrared-detectors/

[105] W. Jianfei, “Resonant-cavity-enhanced multispectral infrared photodetectors for monolithic integration on silicon,” Massachusetts Institute of Technology. Dept. of Materials Science and Engineering., 2010. Accessed: May 29, 2025. [Online]. Available: https://dspace.mit.edu/handle/1721.1/62682

[106] A. Rogalski and J. Piotrowski, “Intrinsic infrared detectors,” *Progress in Quantum Electronics*, vol. 12, no. 2–3, pp. 87–289, Jan. 1988, doi: 10.1016/0079-6727(88)90001-8.

[107] “PbSe 4 Channel Infrared Detector,” Infrared materials. Accessed: May 29, 2025. [Online]. Available: https://infraredmaterials.com/pbse-detectors/quad-detector-assembly/

[108] “Comparison of gas detection limits of NDIR Thermopile, Pyroelectric and PbSe detectors,” Trinamix. Accessed: May 29, 2025. [Online]. Available: https://trinamixsensing.com/news-events/news/comparison-of-gas-detection-limits-of-ndir-thermopile-pyroelectric-and-pbse-detectors/

[109] Electro Optical Components, Inc, “Carbon dioxide (CO2) measurement using Non-Dispersive Infrared (NDIR) Spectroscopy with lead selenide (PbSe) photodetectors.” Accessed: May 29, 2025. [Online]. Available: https://www.eoc-inc.com/wp-content/uploads/NDIR-CO2-sensing-with-PbSe.pdf

[110] USDA Forest Service, “Fire Imaging Technologies Users Guide.” 2020. Accessed: Aug. 28, 2024. [Online]. Available: https://www.nifc.gov/sites/default/files/document-media/Fire%20Imaging%20Technologies%20Users%20Guide.pdf

[111] S. Kim, S. Choo, Y. Kim, W. S. Hwang, and M. Shin, “Comparative study of the near-infrared detection of PbSe fabricated using a sputter deposition method,” *Thin Solid Films*, vol. 795, p. 140313, Apr. 2024, doi: 10.1016/j.tsf.2024.140313.

[112] S. Brauer, D. H. Ryan, J. O. Ström-Olsen, M. Sutton, and G. B. Stephenson, “Pyrometric temperature controller for million degree per second heating,” *Review of Scientific Instruments*, vol. 61, no. 8, pp. 2214–2219, Aug. 1990, doi: 10.1063/1.1141392.

[113] Y. Fu *et al.*, “A Self-Amplified Near-Infrared Bipolar Phototransistor With a PbSe Nanoband Array Heterostructure for Pharmaceutical Solute Detection,” *IEEE Photonics J.*, vol. 16, no. 4, pp. 1–7, Aug. 2024, doi: 10.1109/JPHOT.2024.3412201.

[114] Y. Huang, S. K. Kalyoncu, Q. Zhao, R. Torun, and O. Boyraz, “Silicon-on-sapphire waveguides design for mid-IR evanescent field absorption gas sensors,” *Optics Communications*, vol. 313, pp. 186–194, Feb. 2014, doi: 10.1016/j.optcom.2013.10.022.

[115] M. Pujadas, A. Oche, J. M. Barcala, and J. Teres, “Continuous emission monitoring system based on a PbSe detector array,” presented at the European Symposium on Optics for Environmental and Public Safety, P. Fabian, V. Klein, M. Tacke, K. Weber, and C. Werner, Eds., Munich, Germany, Sept. 1995, pp. 738–747. doi: 10.1117/12.221078.

[116] D. Tyagi *et al.*, “Recent advances in two-dimensional-material-based sensing technology toward health and environmental monitoring applications,” *Nanoscale*, vol. 12, no. 6, pp. 3535–3559, 2020, doi: 10.1039/C9NR10178K.

[117] HAMAMATSU, “Type II superlattice infrared detector.” Accessed: Oct. 06, 2025. [Online]. Available: https://www.hamamatsu.com/us/en/product/optical-sensors/infrared-detector/type2-superlattice.html

[118] HAMAMATSU, “InAsSb photovoltaic detectors.” Accessed: Oct. 06, 2025. [Online]. Available: https://www.hamamatsu.com/us/en/product/optical-sensors/infrared-detector/inassb-photovoltaic-detector.html

[119] “InAs and InAsSb IR Detectors.” Accessed: Oct. 05, 2025. [Online]. Available: https://vigophotonics.com/products/infrared-detectors/inas-and-inassb-ir-detectors/?_gl=1*v00lpl*_up*MQ..*_ga*MTUzMDA5NTc5LjE3NTk3MTQ0OTE.*_ga_1ZY6DNW5XK*czE3NTk3MTQ0OTAkbzEkZzAkdDE3NTk3MTQ0OTAkajYwJGwwJGg2MDEzMjQwNTU.

[120] TELEDYNE, “PV MCT TE Cooled.” Accessed: Oct. 05, 2025. [Online]. Available: https://www.teledynevisionsolutions.com/products/pv-mct-te-cooled/?vertical=tvs-judson-general&segment=tvs

[121] “HgCdTe room temperature optically immersed photovoltaic infrared detector, PVI-5-1x1-TO39-NW-36.” Accessed: July 21, 2025. [Online]. Available: https://vigophotonics.com/product/hgcdte-photovoltaic-ir-detector-pvi-5-1x1-to39-nw-36/?_gl=1*k1mnn9*_up*MQ..*_ga*MTkyMDA3NTA1OS4xNzUyNjg0NzU4*_ga_1ZY6DNW5XK*czE3NTI2ODQ3NTYkbzEkZzAkdDE3NTI2ODQ3NTYkajYwJGwwJGg1NDEyODIwNjQ.

[122] J. Qiu, B. Weng, Z. Yuan, and Z. Shi, “Study of sensitization process on mid-infrared uncooled PbSe photoconductive detectors leads to high detectivity,” *Journal of Applied Physics*, vol. 113, no. 10, Mar. 2013, doi: 10.1063/1.4794492.

[123] A. Rogalski, “Next decade in infrared detectors,” in *Electro-Optical and Infrared Systems: Technology and Applications XIV*, D. A. Huckridge, R. Ebert, and H. Bürsing, Eds., Warsaw, Poland: SPIE, Oct. 2017, p. 100. doi: 10.1117/12.2300779.

[124] A. Rogalski, P. Martyniuk, and M. Kopytko, “Type-II superlattice photodetectors versus HgCdTe photodiodes,” *Progress in Quantum Electronics*, vol. 68, p. 100228, Nov. 2019, doi: 10.1016/j.pquantelec.2019.100228.

[125] N. Korti-Baghdadli, A. E. Merad, and T. Benouaz, “Adjusted Adashi’s Model of Exciton Bohr Parameter and New Proposed Models for Optical Properties of III-V Semiconductors,” *AJMST*, 2013, doi: 10.7726/ajmst.2013.1008.

[126] A. M. Smith and S. Nie, “Semiconductor Nanocrystals: Structure, Properties, and Band Gap Engineering,” *Acc. Chem. Res.*, vol. 43, no. 2, pp. 190–200, Feb. 2010, doi: 10.1021/ar9001069.

[127] A. P. Alivisatos, “Semiconductor clusters, nanocrystals, and quantum dots,” *science*, vol. 271, no. 5251, pp. 933–937, 1996.

[128] V. Proshchenko and Y. Dahnovsky, “Tunable Luminescence in CdSe Quantum Dots Doped by Mn Impurities,” *J. Phys. Chem. C*, vol. 118, no. 48, pp. 28314–28321, Dec. 2014, doi: 10.1021/jp5103324.

[129] A. M. Smith, L. A. Lane, and S. Nie, “Mapping the spatial distribution of charge carriers in quantum-confined heterostructures,” *Nat Commun*, vol. 5, no. 1, p. 4506, July 2014, doi: 10.1038/ncomms5506.

[130] H. Shabbir and M. Wojnicki, “Recent Progress of Non-Cadmium and Organic Quantum Dots for Optoelectronic Applications with a Focus on Photodetector Devices,” *Electronics*, vol. 12, no. 6, p. 1327, Mar. 2023, doi: 10.3390/electronics12061327.

[131] G. Liu *et al.*, “Emerging 2D Materials with Nonparabolic Bands for Ultrafast Photonics,” *Small Science*, vol. 3, no. 10, p. 2300030, Oct. 2023, doi: 10.1002/smsc.202300030.

[132] F. Rana, “2D Nanostructures: Semiconductor Quantum Wells.” Cornell University, 2009. Accessed: Oct. 19, 2025. [Online]. Available: https://courses.cit.cornell.edu/mse5470/handout26.pdf

[133] E. Stock *et al.*, “Acoustic and optical phonon scattering in a single In(Ga)As quantum dot,” *Phys. Rev. B*, vol. 83, no. 4, p. 041304, Jan. 2011, doi: 10.1103/PhysRevB.83.041304.

[134] A. Demić, Z. Ikonić, P. Dean, and D. Indjin, “Dual resonance phonon–photon–phonon terahertz quantum-cascade laser: physics of the electron transport and temperature performance optimization,” *Opt. Express*, vol. 28, no. 26, p. 38788, Dec. 2020, doi: 10.1364/OE.410014.

[135] Y. Go, R. Dutt, and N. Neophytou, “Theory of quasistatically screened electron-polar optical phonon scattering,” *Phys. Rev. B*, vol. 111, no. 19, p. 195211, May 2025, doi: 10.1103/PhysRevB.111.195211.

[136] N. Prodanović, Z. Ikonić, D. Indjin, and P. Harrison, “Relationship between electron-LO phonon and electron-light interaction in quantum dots,” *Phys. Rev. B*, vol. 85, no. 19, p. 195435, May 2012, doi: 10.1103/PhysRevB.85.195435.

[137] T. Meunier *et al.*, “Experimental Signature of Phonon-Mediated Spin Relaxation in a Two-Electron Quantum Dot,” *Phys. Rev. Lett.*, vol. 98, no. 12, p. 126601, Mar. 2007, doi: 10.1103/PhysRevLett.98.126601.

[138] S. V. Kilina, A. J. Neukirch, B. F. Habenicht, D. S. Kilin, and O. V. Prezhdo, “Quantum Zeno Effect Rationalizes the Phonon Bottleneck in Semiconductor Quantum Dots,” *Phys. Rev. Lett.*, vol. 110, no. 18, p. 180404, May 2013, doi: 10.1103/PhysRevLett.110.180404.

[139] J. Zhang *et al.*, “Colloidal Quantum Dots: Synthesis, Composition, Structure, and Emerging Optoelectronic Applications,” *Laser & Photonics Reviews*, vol. 17, no. 3, p. 2200551, Mar. 2023, doi: 10.1002/lpor.202200551.

[140] J. A. Smyder and T. D. Krauss, “Coming attractions for semiconductor quantum dots,” *Materials Today*, vol. 14, no. 9, pp. 382–387, Sept. 2011, doi: 10.1016/S1369-7021(11)70182-1.

[141] C. Gréboval, A. Chu, N. Goubet, C. Livache, S. Ithurria, and E. Lhuillier, “Mercury Chalcogenide Quantum Dots: Material Perspective for Device Integration,” *Chem. Rev.*, vol. 121, no. 7, pp. 3627–3700, Apr. 2021, doi: 10.1021/acs.chemrev.0c01120.

[142] E. Lhuillier, S. Keuleyan, H. Liu, and P. Guyot-Sionnest, “Mid-IR Colloidal Nanocrystals,” *Chem. Mater.*, vol. 25, no. 8, pp. 1272–1282, Apr. 2013, doi: 10.1021/cm303801s.

[143] S. Keuleyan, E. Lhuillier, V. Brajuskovic, and P. Guyot-Sionnest, “Mid-infrared HgTe colloidal quantum dot photodetectors,” *Nature Photon*, vol. 5, no. 8, pp. 489–493, Aug. 2011, doi: 10.1038/nphoton.2011.142.

[144] E. Lhuillier, S. Keuleyan, P. Rekemeyer, and P. Guyot-Sionnest, “Thermal properties of mid-infrared colloidal quantum dot detectors,” *Journal of Applied Physics*, vol. 110, no. 3, p. 033110, Aug. 2011, doi: 10.1063/1.3619857.

[145] E. Lhuillier, S. Keuleyan, P. Zolotavin, and P. Guyot-Sionnest, “Mid-Infrared HgTe/As $_2$ S $_3$ Field Effect Transistors and Photodetectors,” *Advanced Materials*, vol. 25, no. 1, pp. 137–141, Jan. 2013, doi: 10.1002/adma.201203012.

[146] M. E. Cryer and J. E. Halpert, “300 nm Spectral Resolution in the Mid-Infrared with Robust, High Responsivity Flexible Colloidal Quantum Dot Devices at Room Temperature,” *ACS Photonics*, vol. 5, no. 8, pp. 3009–3015, Aug. 2018, doi: 10.1021/acsphotonics.8b00738.

[147] T. Nakotte *et al.*, “Colloidal quantum dot based infrared detectors: extending to the mid-infrared and moving from the lab to the field,” *J. Mater. Chem. C*, vol. 10, no. 3, pp. 790–804, 2022, doi: 10.1039/D1TC05359K.

[148] A. J. Ciani, R. E. Pimpinella, C. H. Grein, and P. Guyot-Sionnest, “Colloidal quantum dots for low-cost MWIR imaging,” presented at the SPIE Defense + Security, B. F. Andresen, G. F. Fulop, C. M. Hanson, J. L. Miller, and P. R. Norton, Eds., Baltimore, Maryland, United States, May 2016, p. 981919. doi: 10.1117/12.2234734.

[149] P. Guyot-Sionnest and J. A. Roberts, “Background limited mid-infrared photodetection with photovoltaic HgTe colloidal quantum dots,” *Applied Physics Letters*, vol. 107, no. 25, p. 253104, Dec. 2015, doi: 10.1063/1.4938135.

[150] M. M. Ackerman, X. Tang, and P. Guyot-Sionnest, “Fast and Sensitive Colloidal Quantum Dot Mid-Wave Infrared Photodetectors,” *ACS Nano*, vol. 12, no. 7, pp. 7264–7271, July 2018, doi: 10.1021/acsnano.8b03425.

[151] X. Tang, M. M. Ackerman, and P. Guyot-Sionnest, “Thermal Imaging with Plasmon Resonance Enhanced HgTe Colloidal Quantum Dot Photovoltaic Devices,” *ACS Nano*, vol. 12, no. 7, pp. 7362–7370, July 2018, doi: 10.1021/acsnano.8b03871.

[152] X. Xue, M. Chen, Y. Luo, T. Qin, X. Tang, and Q. Hao, “High-operating-temperature mid-infrared photodetectors via quantum dot gradient homojunction,” *Light Sci Appl*, vol. 12, no. 1, p. 2, Jan. 2023, doi: 10.1038/s41377-022-01014-0.

[153] W. H. Strehlow and E. L. Cook, “Compilation of Energy Band Gaps in Elemental and Binary Compound Semiconductors and Insulators,” *Journal of Physical and Chemical Reference Data*, vol. 2, no. 1, pp. 163–200, Jan. 1973, doi: 10.1063/1.3253115.

[154] M. Park, D. Choi, Y. Choi, H. Shin, and K. S. Jeong, “Mid-Infrared Intraband Transition of Metal Excess Colloidal Ag $_2$ Se Nanocrystals,” *ACS Photonics*, vol. 5, no. 5, pp. 1907–1911, May 2018, doi: 10.1021/acsphotonics.8b00291.

[155] J. Qu *et al.*, “Intraband Mid-Infrared Transitions in Ag $_2$ Se Nanocrystals: Potential and Limitations for Hg-Free Low-Cost Photodetection,” *J. Phys. Chem. C*, vol. 122, no. 31, pp. 18161–18167, Aug. 2018, doi: 10.1021/acs.jpcc.8b05699.

[156] S. B. Hafiz, M. M. Al Mahfuz, S. Lee, and D.-K. Ko, “Midwavelength Infrared p–n Heterojunction Diodes Based on Intraband Colloidal Quantum Dots,” *ACS Appl. Mater. Interfaces*, vol. 13, no. 41, pp. 49043–49049, Oct. 2021, doi: 10.1021/acsami.1c14749.

[157] D. Vankhade, A. Kothari, and T. K. Chaudhuri, "Direct-Coated Photoconducting Nanocrystalline PbS Thin Films with Tunable Band Gap," *Journal of Elec Materi*, vol. 45, no. 6, pp. 2789–2795, June 2016, doi: 10.1007/s11664-016-4364-1.

[158] C. E. Ekuma, D. J. Singh, J. Moreno, and M. Jarrell, "Optical properties of PbTe and PbSe," *Phys. Rev. B*, vol. 85, no. 8, p. 085205, Feb. 2012, doi: 10.1103/PhysRevB.85.085205.

[159] A. I. Belogorokhov, I. I. Ivanchik, and D. R. Khokhlov, "Pbte(Ga) - New Multispectral Infrared Photodetector," *MRS Proc.*, vol. 487, p. 645, 1997, doi: 10.1557/PROC-487-645.

[160] E. Indrea and A. Barbu, "Indirect photon interaction in PbS photodetectors," *Applied Surface Science*, vol. 106, pp. 498–501, Oct. 1996, doi: 10.1016/S0169-4332(96)00394-7.

[161] K. R. Williams *et al.*, "Synthesis of Type I PbSe/CdSe Dot-on-Plate Heterostructures with Near-Infrared Emission," *J. Am. Chem. Soc.*, vol. 141, no. 13, pp. 5092–5096, Apr. 2019, doi: 10.1021/jacs.8b13794.

[162] X. Xing, H. Liu, W. Shang, and Z. Chen, "An ammonia gas detection system using liquid quantum dot LEDs based differential optical absorption spectroscopy," *Optics Communications*, vol. 451, pp. 28–34, Nov. 2019, doi: 10.1016/j.optcom.2019.06.002.

[163] J. Qiu, B. Weng, L. L. McDowell, and Z. Shi, "Low-cost uncooled MWIR PbSe quantum dots photodiodes," *RSC Adv.*, vol. 9, no. 72, pp. 42516–42523, 2019, doi: 10.1039/C9RA07664F.

[164] "Molecular-beam epitaxy." Accessed: June 06, 2025. [Online]. Available: https://en.wikipedia.org/wiki/Molecular-beam_epitaxy

[165] X. Yan *et al.*, "*In situ* x-ray and electron scattering studies of oxide molecular beam epitaxial growth," *APL Materials*, vol. 8, no. 10, p. 101107, Oct. 2020, doi: 10.1063/5.0025849.

[166] M. Mahandesh, "Scanning Electron Microscope." Accessed: June 09, 2025. [Online]. Available: https://www.tribonet.org/wiki/scanning-electron-microscope/

[167] "Park Systems AFM." [Online]. Available: https://parksystems.com/cn/AFM_gallery/AFM_gallery_view.php?id=91&word=Nano

[168] J. Qiu, B. Weng, Z. Yuan, and Z. Shi, "Study of sensitization process on mid-infrared uncooled PbSe photoconductive detectors leads to high detectivity," *Journal of Applied Physics*, vol. 113, no. 10, Art. no. 10, Mar. 2013, doi: 10.1063/1.4794492.

[169] L. Zhao, J. Qiu, B. Weng, C. Chang, Z. Yuan, and Z. Shi, "Understanding sensitization behavior of lead selenide photoconductive detectors by charge separation model," *Journal of Applied Physics*, vol. 115, no. 8, Art. no. 8, Feb. 2014, doi: 10.1063/1.4867038.

[170] B. Weng, J. Qiu, Z. Yuan, P. R. Larson, G. W. Strout, and Z. Shi, "Responsivity enhancement of mid-infrared PbSe detectors using CaF_2 nano-structured antireflective coatings," *Appl. Phys. Lett.*, vol. 104, no. 2, Art. no. 2, Jan. 2014, doi: 10.1063/1.4861186.

[171] K. Green, S.-S. Yoo, and C. Kauffman, "Lead salt TE-cooled imaging sensor development," presented at the SPIE Defense + Security, B. F. Andresen, G. F. Fulop, C. M. Hanson, and P. R. Norton, Eds., Baltimore, Maryland, USA, June 2014, p. 90701G. doi: 10.1117/12.2053302.

[172] S. Ganguly, X. Tang, S.-S. Yoo, P. Guyot-Sionnest, and A. W. Ghosh, "Extrinsic voltage control of effective carrier lifetime in polycrystalline PbSe mid-wave IR photodetectors for increased detectivity," *AIP Advances*, vol. 10, no. 9, p. 095117, Sept. 2020, doi: 10.1063/5.0019342.

[173] H. Yang, G. Wang, X. Li, and J. Zheng, "Effect of in situ O+ beam induction on the microstructures and optical properties of polycrystalline lead selenide films," *Materials Letters*, vol. 251, pp. 85–88, Sept. 2019, doi: 10.1016/j.matlet.2019.05.042.

[174] P. Kumar, M. Pfeffer, E. Schweda, O. Eibl, J. Qiu, and Z. Shi, "PbSe mid-IR photoconductive thin films (part I): Phase analysis of the functional layer," *Journal of Alloys and Compounds*, vol. 724, pp. 316–326, Nov. 2017, doi: 10.1016/j.jallcom.2017.06.330.

[175] P. Kumar, M. Pfeffer, C. Berthold, and O. Eibl, "PbSe mid-IR photoconductive thin films (part-II): Structural analysis of the functional layer," *Journal of Alloys and Compounds*, vol. 735, pp. 1654–1661, Feb. 2018, doi: 10.1016/j.jallcom.2017.11.252.

[176] H. Wu, J. Si, T. Xu, and C. Cao, "Progress of IV-VI Semiconductor Research in China," in *2006 Joint 31st International Conference on Infrared Millimeter Waves and 14th International Conference on Teraherz Electronics*, Shanghai: IEEE, Sept. 2006, pp. 407–407. doi: 10.1109/ICIMW.2006.368615.

[177] H. Yang, X. Li, G. Wang, and J. Zheng, "The electrical properties of carrier transport between lead selenide polycrystallites manipulated by iodine concentration," *AIP Advances*, vol. 8, no. 8, p. 085316, Aug. 2018, doi: 10.1063/1.5023450.

[178] L. L. McDowell, M. Rastkar, and Z. Shi, "Integration of epitaxial n-PbSe Films on mismatched p-Ge substrates to form a p-n heterogeneous structure," in *Infrared Technology and Applications XLVIII*, G. F. Fulop, M. Kimata, L. Zheng, B. F. Andresen, J. L. Miller, and Y.-H. Kim, Eds., Orlando, United States: SPIE, May 2022, p. 67. doi: 10.1117/12.2618652.

[179] M. Tacke, "New developments and applications of tunable IR lead salt lasers," *Infrared Physics & Technology*, vol. 36, no. 1, Art. no. 1, Jan. 1995, doi: 10.1016/1350-4495(94)00101-P.

[180] B. Weng *et al.*, "Room temperature mid-infrared surface-emitting photonic crystal laser on silicon," *Appl. Phys. Lett.*, vol. 99, no. 22, Art. no. 22, Nov. 2011, doi: 10.1063/1.3665402.

[181] H. Zogg, "Epitaxial lead-chalcogenide on silicon layers for thermal imaging applications," presented at the Material Science and Material Properties for Infrared Optoelectronics, F. F. Sizov, Ed., Kiev, Ukraine, Nov. 1999, pp. 22–26. doi: 10.1117/12.368352.

[182] J. J. Choi *et al.*, "PbSe Nanocrystal Excitonic Solar Cells," *Nano Lett.*, vol. 9, no. 11, Art. no. 11, Nov. 2009, doi: 10.1021/nl901930g.

[183] E. O. Wrasse and T. M. Schmidt, "Prediction of Two-Dimensional Topological Crystalline Insulator in PbSe Monolayer," *Nano Lett.*, vol. 14, no. 10, Art. no. 10, Oct. 2014, doi: 10.1021/nl502481f.

[184] J. M. Woodall, "Heterogeneous integration of semiconductor materials: basic issues, current progress, and future prospects," presented at the SPIE Defense, Security, and Sensing,

T. George, M. S. Islam, and A. Dutta, Eds., Baltimore, Maryland, USA, May 2012, p. 83731B. doi: 10.1117/12.917911.

[185] P. Müller, A. Fach, J. John, A. N. Tiwari, H. Zogg, and G. Kostorz, "Structure of epitaxial PbSe grown on Si(111) and Si(100) without a fluoride buffer layer," *Journal of Applied Physics*, vol. 79, no. 4, pp. 1911–1916, Feb. 1996, doi: 10.1063/1.361076.

[186] X. J. Wang *et al.*, "Heteroepitaxy of PbSe on GaAs(100) and GaAs(211)B by molecular beam epitaxy," *Journal of Crystal Growth*, vol. 311, no. 8, pp. 2359–2362, Apr. 2009, doi: 10.1016/j.jcrysgro.2009.01.140.

[187] B. B. Haidet, E. T. Hughes, and K. Mukherjee, "Nucleation control and interface structure of rocksalt PbSe on (001) zincblende III-V surfaces," *Phys. Rev. Materials*, vol. 4, no. 3, p. 033402, Mar. 2020, doi: 10.1103/PhysRevMaterials.4.033402.

[188] B. B. Haidet *et al.*, "Interface structure and luminescence properties of epitaxial PbSe films on InAs(111)A," *Journal of Vacuum Science & Technology A*, vol. 39, no. 2, p. 023404, Mar. 2021, doi: 10.1116/6.0000774.

[189] S. Jin, C. Cai, G. Bi, B. Zhang, H. Wu, and Y. Zhang, "Two-dimensional electron gas at the metastable twisted interfaces of CdTe/PbTe (111) single heterojunctions," *Phys. Rev. B*, vol. 87, no. 23, Art. no. 23, June 2013, doi: 10.1103/PhysRevB.87.235315.

[190] X. J. Wang *et al.*, "Characterization of PbSnSe/CdTe/Si (211) Epilayers Grown by Molecular Beam Epitaxy," *Journal of Elec Materi*, vol. 37, no. 9, Art. no. 9, Sept. 2008, doi: 10.1007/s11664-008-0480-x.

[191] S. Chusnutdinow, S. Schreyeck, S. Kret, A. Kazakov, and G. Karczewski, "Room temperature infrared detectors made of PbTe/CdTe multilayer composite," *Appl. Phys. Lett.*, vol. 117, no. 7, Art. no. 7, Aug. 2020, doi: 10.1063/5.0018686.

[192] A. Pashaev, O. Davarashvili, Z. Akhvlediani, M. Enukashvili, R. Gulyaev, and V. Zlomanov, "Unrelaxed State in Epitaxial Heterostructures Based on Lead Selenide," *JMP*, vol. 03, no. 06, pp. 502–510, 2012, doi: 10.4236/jmp.2012.36068.

[193] X. J. Wang *et al.*, "Heteroepitaxy of PbSe on GaAs(100) and GaAs(211)B by molecular beam epitaxy," *Journal of Crystal Growth*, vol. 311, no. 8, pp. 2359–2362, Apr. 2009, doi: 10.1016/j.jcrysgro.2009.01.140.

[194] B. B. Haidet, E. T. Hughes, and K. Mukherjee, "Nucleation control and interface structure of rocksalt PbSe on (001) zincblende III-V surfaces," *Phys. Rev. Materials*, vol. 4, no. 3, p. 033402, Mar. 2020, doi: 10.1103/PhysRevMaterials.4.033402.

[195] B. B. Haidet *et al.*, "Interface structure and luminescence properties of epitaxial PbSe films on InAs(111)A," *Journal of Vacuum Science & Technology A*, vol. 39, no. 2, p. 023404, Mar. 2021, doi: 10.1116/6.0000774.

[196] Z. Shao *et al.*, "Epitaxial Growth of PbSe Few-Layers on $SrTiO_3$: The Effect of Compressive Strain and Potential Two-Dimensional Topological Crystalline Insulator," *ACS Nano*, p. acsnano.9b00072, Feb. 2019, doi: 10.1021/acsnano.9b00072.

[197] B. Weng, J. Qiu, L. Zhao, Z. Yuan, C. Chang, and Z. Shi, "Recent development on the uncooled mid-infrared PbSe detectors with high detectivity," presented at the SPIE OPTO, M.

Razeghi, E. Tournié, and G. J. Brown, Eds., San Francisco, California, United States, Dec. 2013, p. 899311. doi: 10.1117/12.2041276.

[198] B. Weng, J. Qiu, L. Zhao, C. Chang, and Z. Shi, "CdS/PbSe heterojunction for high temperature mid-infrared photovoltaic detector applications," *Appl. Phys. Lett.*, vol. 104, no. 12, Art. no. 12, Mar. 2014, doi: 10.1063/1.4869752.

[199] J. Qiu, B. Weng, L. L. McDowell, and Z. Shi, "Low-cost uncooled MWIR PbSe quantum dots photodiodes," *RSC Adv.*, vol. 9, no. 72, Art. no. 72, 2019, doi: 10.1039/C9RA07664F.

[200] C. Misbah, O. Pierre-Louis, and Y. Saito, "Crystal surfaces in and out of equilibrium: A modern view," *Rev. Mod. Phys.*, vol. 82, no. 1, Art. no. 1, Mar. 2010, doi: 10.1103/RevModPhys.82.981.

[201] Nils. A. K. Kaufmann, L. Lahourcade, B. Hourahine, D. Martin, and N. Grandjean, "Critical impact of Ehrlich–Schwöbel barrier on GaN surface morphology during homoepitaxial growth," *Journal of Crystal Growth*, vol. 433, pp. 36–42, Jan. 2016, doi: 10.1016/j.jcrysgro.2015.06.013.

[202] T. N. Xu, H. Z. Wu, J. X. Si, and C. F. Cao, "Observation of triangle pits in PbSe grown by molecular beam epitaxy," *Applied Surface Science*, vol. 253, no. 12, pp. 5457–5461, Apr. 2007, doi: 10.1016/j.apsusc.2006.12.028.

[203] X. M. Fang, "Molecular beam epitaxial growth of Bi[sub 2]Se[sub 3]- and Tl[sub 2]Se-doped PbSe and PbEuSe on CaF[sub 2]/Si(111)," *J. Vac. Sci. Technol. B*, vol. 16, no. 3, p. 1459, May 1998, doi: 10.1116/1.589965.

[204] F. Zhao, H. Wu, A. Majumdar, and Z. Shi, "Continuous wave optically pumped lead-salt mid-infrared quantum-well vertical-cavity surface-emitting lasers," *Appl. Phys. Lett.*, vol. 83, no. 25, pp. 5133–5135, Dec. 2003, doi: 10.1063/1.1636246.

[205] X. Shi *et al.*, "Study on the Theoretical Limitation of the Mid-Infrared PbSe N⁺-P Junction Detectors at High Operating Temperature," *Detection*, vol. 06, no. 01, Art. no. 01, 2018, doi: 10.4236/detection.2018.61001.

[206] M. Lach-hab, D. A. Papaconstantopoulos, and M. J. Mehl, "Electronic structure calculations of lead chalcogenides PbS, PbSe, PbTe," *Journal of Physics and Chemistry of Solids*, vol. 63, no. 5, pp. 833–841, May 2002, doi: 10.1016/S0022-3697(01)00237-2.

[207] N. Samarth *et al.*, "Growth of cubic (zinc blende) CdSe by molecular beam epitaxy," *Appl. Phys. Lett.*, vol. 54, no. 26, pp. 2680–2682, June 1989, doi: 10.1063/1.101033.

[208] E. Y. Muslih, B. Munir, and M. M. Khan, "Advances in chalcogenides and chalcogenides-based nanomaterials such as sulfides, selenides, and tellurides," in *Chalcogenide-Based Nanomaterials as Photocatalysts*, Elsevier, 2021, pp. 7–31. doi: 10.1016/B978-0-12-820498-6.00002-0.

[209] C. J. Hanson *et al.*, "Giant PbSe/CdSe/CdSe Quantum Dots: Crystal-Structure-Defined Ultrastable Near-Infrared Photoluminescence from Single Nanocrystals," *J. Am. Chem. Soc.*, vol. 139, no. 32, pp. 11081–11088, Aug. 2017, doi: 10.1021/jacs.7b03705.

[210] G. Zaiats *et al.*, "PbSe/CdSe Thin-Shell Colloidal Quantum Dots," *Zeitschrift für Physikalische Chemie*, vol. 229, no. 1–2, pp. 3–21, Feb. 2015, doi: 10.1515/zpch-2014-0625.

[211] C. M. Cirloganu *et al.*, "Enhanced carrier multiplication in engineered quasi-type-II quantum dots," *Nat Commun*, vol. 5, no. 1, p. 4148, Sept. 2014, doi: 10.1038/ncomms5148.

[212] L. Lystrom, P. Tamukong, D. Mihaylov, and S. Kilina, "Phonon-Driven Energy Relaxation in PbS/CdS and PbSe/CdSe Core/Shell Quantum Dots," *J. Phys. Chem. Lett.*, vol. 11, no. 11, pp. 4269–4278, June 2020, doi: 10.1021/acs.jpclett.0c00845.

[213] B. B. V. Salzmann *et al.*, "Two-Dimensional CdSe-PbSe Heterostructures and PbSe Nanoplatelets: Formation, Atomic Structure, and Optical Properties," *J. Phys. Chem. C*, vol. 126, no. 3, pp. 1513–1522, Jan. 2022, doi: 10.1021/acs.jpcc.1c09412.

[214] B. De Geyter *et al.*, "The Different Nature of Band Edge Absorption and Emission in Colloidal PbSe/CdSe Core/Shell Quantum Dots," *ACS Nano*, vol. 5, no. 1, pp. 58–66, Jan. 2011, doi: 10.1021/nn102980e.

[215] Y. Zhang *et al.*, "Formation of PbSe/CdSe Core/Shell Nanocrystals for Stable Near-Infrared High Photoluminescence Emission," *Nanoscale Res Lett*, vol. 5, no. 8, pp. 1279–1283, Aug. 2010, doi: 10.1007/s11671-010-9637-7.

[216] M. R. Mirzaei, A. Rostami, S. Matloub, and H. Mirtaghizadeh, "Ultra-high-efficiency luminescent solar concentrator using superimposed colloidal quantum dots," *Optical and Quantum Electronics*, vol. 52, no. 6, pp. 1–16, 2020, doi: 10.1007/s11082-020-02442-1.

[217] B. Zorman, M. V. Ramakrishna, and R. A. Friesner, "Quantum Confinement Effects in CdSe Quantum Dots," *J. Phys. Chem.*, vol. 99, no. 19, pp. 7649–7653, May 1995, doi: 10.1021/j100019a052.

[218] S. Adachi, *Properties of Group-IV, III-V and II-VI Semiconductors: Adachi/Properties of Group-IV, III-V and II-VI Semiconductors*. Chichester, UK: John Wiley & Sons, Ltd, 2005. doi: 10.1002/0470090340.

[219] A. S. Chizhov *et al.*, "Visible light activation of room temperature NO 2 gas sensors based on ZnO, SnO 2 and In 2 O 3 sensitized with CdSe quantum dots," *Thin Solid Films*, vol. 618, pp. 253–262, Nov. 2016, doi: 10.1016/j.tsf.2016.09.029.

[220] R. K. Swank, "Surface Properties of II-VI Compounds," *Phys. Rev.*, vol. 153, no. 3, pp. 844–849, Jan. 1967, doi: 10.1103/PhysRev.153.844.

[221] H. Suzuki, "Electron Affinity of Semiconducting Compound CdSe," *Jpn. J. Appl. Phys.*, vol. 5, no. 12, p. 1253, Dec. 1966, doi: 10.1143/JJAP.5.1253.

[222] J. Qiu, Y. Liu, Z. Cai, Q. Phan, and Z. Shi, "CdSe:In Mid-infrared transparent conductive films prospering uncooled PbSe/CdSe heterojunction photovoltaic detectors," *Mater. Adv.*, vol. 3, no. 2, pp. 1079–1086, 2022, doi: 10.1039/D1MA00760B.

[223] Y. Luo, L. McDowell, L. Su, Y. Liu, J. Qiu, and Z. Shi, "Enhanced performance in uncooled n-CdSe/p-PbSe photovoltaic detectors by high-temperature chloride passivation," *RSC Adv.*, vol. 12, no. 14, pp. 8423–8428, 2022, doi: 10.1039/D2RA00483F.

[224] J. Qiu, B. Weng, Z. Yuan, and Z. Shi, "Study of sensitization process on mid-infrared uncooled PbSe photoconductive detectors leads to high detectivity," *Journal of Applied Physics*, vol. 113, no. 10, p. 103102, Mar. 2013, doi: 10.1063/1.4794492.

[225] K. Green, S.-S. Yoo, and C. Kauffman, "Lead salt TE-cooled imaging sensor development," presented at the SPIE Defense + Security, Baltimore, Maryland, USA: SPIE, June 2014, p. 90701G. doi: https://doi.org/10.1117/12.2053302.

[226] T. R. Beystrum, R. Himoto, N. Jacksen, and M. Sutton, "Low-cost PbSalt FPAs," presented at the Defense and Security, Orlando, FL: SPIE, Aug. 2004, p. 287. doi: https://doi.org/10.1117/12.544177.

[227] D. Wu, A. Dehzangi, J. Li, and M. Razeghi, "High performance Zn-diffused planar mid-wavelength infrared type-II InAs/InAs1−xSbx superlattice photodetector by MOCVD," *Applied Physics Letters*, vol. 116, no. 16, p. 161108, Apr. 2020, doi: 10.1063/5.0005326.

[228] A. Rogalski, P. Martyniuk, and M. Kopytko, "Type-II superlattice photodetectors versus HgCdTe photodiodes," *Progress in Quantum Electronics*, vol. 68, p. 100228, Nov. 2019, doi: 10.1016/j.pquantelec.2019.100228.

[229] J. Kim, J. Roh, M. Park, and C. Lee, "Recent Advances and Challenges of Colloidal Quantum Dot Light-Emitting Diodes for Display Applications," *Advanced Materials*, p. 2212220, July 2023, doi: 10.1002/adma.202212220.

[230] E. Jang, Y. Kim, Y.-H. Won, H. Jang, and S.-M. Choi, "Environmentally Friendly InP-Based Quantum Dots for Efficient Wide Color Gamut Displays," *ACS Energy Lett.*, vol. 5, no. 4, pp. 1316–1327, Apr. 2020, doi: 10.1021/acsenergylett.9b02851.

[231] S. Ahn, W. Chen, and O. Vazquez-Mena, "High resolution patterning of PbS quantum dots/graphene photodetectors with high responsivity *via* photolithography with a top graphene layer to protect surface ligands," *Nanoscale Adv.*, vol. 3, no. 21, pp. 6206–6212, 2021, doi: 10.1039/D1NA00582K.

[232] M. Sulaman *et al.*, "Hybrid Bulk-Heterojunction of Colloidal Quantum Dots and Mixed-Halide Perovskite Nanocrystals for High-Performance Self-Powered Broadband Photodetectors," *Adv Funct Materials*, vol. 32, no. 28, p. 2201527, July 2022, doi: 10.1002/adfm.202201527.

[233] P. Martyniuk and A. Rogalski, "Comparison of performance of quantum dot and other types of infrared photodetectors," presented at the SPIE Defense and Security Symposium, B. F. Andresen, G. F. Fulop, and P. R. Norton, Eds., Orlando, FL, Apr. 2008, p. 694004. doi: 10.1117/12.785200.

[234] P. M. Petroff, A. Lorke, and A. Imamoglu, "Epitaxially Self-Assembled Quantum Dots," *Physics Today*, vol. 54, no. 5, pp. 46–52, May 2001, doi: 10.1063/1.1381102.

[235] C. Livache *et al.*, "A colloidal quantum dot infrared photodetector and its use for intraband detection," *Nat Commun*, vol. 10, no. 1, p. 2125, May 2019, doi: 10.1038/s41467-019-10170-8.

[236] H. Song, Y. Tischenko, D. Wasserman, and K. S. Jeong, "Quantum dot materials for mid-IR photodetection: opinion," *Opt. Mater. Express*, vol. 13, no. 5, p. 1328, May 2023, doi: 10.1364/OME.489877.

[237] S. Zhang, Y. Hu, and Q. Hao, "Advances of Sensitive Infrared Detectors with HgTe Colloidal Quantum Dots," *Coatings*, vol. 10, no. 8, p. 760, Aug. 2020, doi: 10.3390/coatings10080760.

[238] J. Jean *et al.*, "Synthesis cost dictates the commercial viability of lead sulfide and perovskite quantum dot photovoltaics," *Energy Environ. Sci.*, vol. 11, no. 9, pp. 2295–2305, 2018, doi: 10.1039/C8EE01348A.

[239] S. M. Tenney *et al.*, "Mercury Chalcogenide Nanoplatelet–Quantum Dot Heterostructures as a New Class of Continuously Tunable Bright Shortwave Infrared Emitters," *J. Phys. Chem. Lett.*, vol. 11, no. 9, pp. 3473–3480, May 2020, doi: 10.1021/acs.jpclett.0c00958.

[240] G. SHEN, "SYNTHESIS OF MERCURY CHALCOGENIDE COLLOIDAL QUANTUM DOTS AND CORE SHELLS," THE UNIVERSITY OF CHICAGO, 2019. Accessed: Sept. 11, 2023. [Online]. Available: https://www.google.com/url?sa=i&rct=j&q=&esrc=s&source=web&cd=&cad=rja&uact=8&ved=0CDgQw7AJahcKEwjY4crF16OBAxUAAAAAHQAAAAAQAw&url=https%3A%2F%2Fknowledge.uchicago.edu%2Frecord%2F1713%2Ffiles%2FShen_uchicago_0330D_14676.pdf&psig=AOvVaw3HwlwRCqzVSPNEqZVvAtMa&ust=1694560394625780&opi=89978449

[241] J. Jeong, B. Yoon, Y.-W. Kwon, D. Choi, and K. S. Jeong, "Singly and Doubly Occupied Higher Quantum States in Nanocrystals," *Nano Lett.*, vol. 17, no. 2, pp. 1187–1193, Feb. 2017, doi: 10.1021/acs.nanolett.6b04915.

[242] G. Shen and P. Guyot-Sionnest, "HgS and HgS/CdS Colloidal Quantum Dots with Infrared Intraband Transitions and Emergence of a Surface Plasmon," *J. Phys. Chem. C*, vol. 120, no. 21, pp. 11744–11753, June 2016, doi: 10.1021/acs.jpcc.6b04014.

[243] C. Livache *et al.*, "Investigation of the Self-Doping Process in HgSe Nanocrystals," *Phys. Status Solidi A*, vol. 215, no. 3, p. 1700294, Feb. 2018, doi: 10.1002/pssa.201700294.

[244] X. Xue, M. Chen, Y. Luo, T. Qin, X. Tang, and Q. Hao, "High-operating-temperature mid-infrared photodetectors via quantum dot gradient homojunction," *Light Sci Appl*, vol. 12, no. 1, p. 2, Jan. 2023, doi: 10.1038/s41377-022-01014-0.

[245] W. Koh, A. C. Bartnik, F. W. Wise, and C. B. Murray, "Synthesis of Monodisperse PbSe Nanorods: A Case for Oriented Attachment," *J. Am. Chem. Soc.*, vol. 132, no. 11, pp. 3909–3913, Mar. 2010, doi: 10.1021/ja9105682.

[246] W. K. Bae *et al.*, "Highly Effective Surface Passivation of PbSe Quantum Dots through Reaction with Molecular Chlorine," *J. Am. Chem. Soc.*, vol. 134, no. 49, pp. 20160–20168, Dec. 2012, doi: 10.1021/ja309783v.

[247] Q. Lin *et al.*, "Design and Synthesis of Heterostructured Quantum Dots with Dual Emission in the Visible and Infrared," *ACS Nano*, vol. 9, no. 1, pp. 539–547, Jan. 2015, doi: 10.1021/nn505793y.

[248] F. J. Sanchez *et al.*, "Progress on monolithic integration of cheap IR FPAs of polycrystalline PbSe," presented at the Defense and Security, B. F. Andresen and G. F. Fulop, Eds., Orlando, Florida, USA, May 2005, p. 441. doi: 10.1117/12.602705.

[249] E. L. Dereniak and G. D. Boreman, *Infrared detectors and systems*. in Wiley series in pure and applied optics. New York: Wiley, 1996.

[250] D. Grodzińska, F. Pietra, M. A. Van Huis, D. Vanmaekelbergh, and C. De Mello Donegá, "Thermally induced atomic reconstruction of PbSe/CdSe core/shell quantum dots into PbSe/CdSe bi-hemisphere hetero-nanocrystals," *J. Mater. Chem.*, vol. 21, no. 31, p. 11556, 2011, doi: 10.1039/c0jm04458j.

[251] R. Koole, G. Allan, C. Delerue, A. Meijerink, D. Vanmaekelbergh, and A. J. Houtepen, "Optical Investigation of Quantum Confinement in PbSe Nanocrystals at Different Points in the Brillouin Zone," *Small*, vol. 4, no. 1, pp. 127–133, Jan. 2008, doi: 10.1002/smll.200700632.

[252] Q. Lin *et al.*, "Influence of selenium vapor postannealing on the electrical transport properties of PbSe–WSe_2 nanolaminates," *J. Mater. Res.*, vol. 26, no. 15, pp. 1866–1871, Aug. 2011, doi: 10.1557/jmr.2011.77.

[253] J. E. Meyer, L. Nordin, T. Nguyen, and K. Mukherjee, "Mid-wave infrared photoluminescence from low-temperature-grown PbSe epitaxial films on GaAs after rapid thermal annealing," *Applied Physics Letters*, vol. 123, no. 13, p. 131109, Sept. 2023, doi: 10.1063/5.0160802.

[254] V. Singh *et al.*, "Evanescently coupled mid-infrared photodetector for integrated sensing applications: Theory and design," *Sensors and Actuators B: Chemical*, vol. 185, pp. 195–200, Aug. 2013, doi: 10.1016/j.snb.2013.04.065.

[255] T. Yager, G. Chikvaidze, Q. Wang, and Y. Fu, "Graphene Hybrid Metasurfaces for Mid-Infrared Molecular Sensors," *Nanomaterials*, vol. 13, no. 14, p. 2113, July 2023, doi: 10.3390/nano13142113.

[256] T. L. Roellig, C. McMurtry, T. Greene, T. Matsuo, I. Sakon, and J. Staguhn, "Mid-infrared detector development for the Origins Space Telescope," *J. Astron. Telesc. Instrum. Syst.*, vol. 6, no. 04, Dec. 2020, doi: 10.1117/1.JATIS.6.4.041503.

[257] R. I. Woodward, M. R. Majewski, D. D. Hudson, and S. D. Jackson, "Swept-wavelength mid-infrared fiber laser for real-time ammonia gas sensing," *APL Photonics*, vol. 4, no. 2, p. 020801, Feb. 2019, doi: 10.1063/1.5065415.

[258] R. Müller *et al.*, "Thermoelectrically-Cooled InAs/GaSb Type-II Superlattice Detectors as an Alternative to HgCdTe in a Real-Time Mid-Infrared Backscattering Spectroscopy System," *Micromachines*, vol. 11, no. 12, p. 1124, Dec. 2020, doi: 10.3390/mi11121124.

[259] Y. Han and A. Zhang, "Cryogenic technology for infrared detection in space," *Sci Rep*, vol. 12, no. 1, p. 2349, Feb. 2022, doi: 10.1038/s41598-022-06216-5.

[260] J. Park, M. M. Al Mahfuz, R. Huebner, and D.-K. Ko, "Uncooled Mid-Wavelength Infrared Photoconductive Detectors Based on PbSe Nanocrystals," *ACS Appl. Electron. Mater.*, vol. 5, no. 4, pp. 2386–2393, Apr. 2023, doi: 10.1021/acsaelm.3c00200.

[261] A. S. Sergeeva, V. F. Markov, and L. N. Maskaeva, "Thermal sensitization of chemically deposited films based on PbSe y S1 − y solid solutions," *Glass Phys Chem*, vol. 40, no. 2, pp. 231–237, Mar. 2014, doi: 10.1134/S1087659614020199.

[262] C. Yang, X. Zhang, P. Li, S. Chen, and S. Feng, "Electrochemical synthesis of hierarchical porous PbSe film and its infrared photodetection properties," *Applied Surface Science*, vol. 663, p. 160145, Aug. 2024, doi: 10.1016/j.apsusc.2024.160145.

[263] C. Yang, S. Feng, Y. Yu, J. Shen, X. Wei, and H. Shi, "Electrochemical epitaxial (200) PbSe submicron-plates on single-layer graphene for an ultrafast infrared response," *J. Mater. Chem. C*, vol. 9, no. 20, pp. 6536–6543, 2021, doi: 10.1039/D1TC00481F.

[264] J. T. Harrison and M. C. Gupta, "Laser fabrication of lead selenide infrared focal plane array devices," *Infrared Physics & Technology*, vol. 135, p. 104977, Dec. 2023, doi: 10.1016/j.infrared.2023.104977.

[265] G. Vergara *et al.*, "Progress on uncooled PbSe detectors for low-cost applications," presented at the Defense and Security, B. F. Andresen and G. F. Fulop, Eds., Orlando, FL, Aug. 2004, p. 279. doi: 10.1117/12.542266.

[266] M. Chen *et al.*, "Mercury Telluride Quantum Dot Based Phototransistor Enabling High-Sensitivity Room-Temperature Photodetection at 2000 nm," *ACS Nano*, vol. 11, no. 6, pp. 5614–5622, June 2017, doi: 10.1021/acsnano.7b00972.

[267] A. De Iacovo, C. Venettacci, C. Giansante, and L. Colace, "Narrowband colloidal quantum dot photodetectors for wavelength measurement applications," *Nanoscale*, vol. 12, no. 18, pp. 10044–10050, 2020, doi: 10.1039/D0NR02626C.

[268] H. Zhang, J. C. Peterson, and P. Guyot-Sionnest, "Intraband Transition of HgTe Nanocrystals for Long-Wave Infrared Detection at 12 μm," *ACS Nano*, vol. 17, no. 8, pp. 7530–7538, Apr. 2023, doi: 10.1021/acsnano.2c12636.

[269] X. Tang, M. M. Ackerman, M. Chen, and P. Guyot-Sionnest, "Dual-band infrared imaging using stacked colloidal quantum dot photodiodes," *Nat. Photonics*, vol. 13, no. 4, pp. 277–282, Apr. 2019, doi: 10.1038/s41566-019-0362-1.

[270] Y. Tian *et al.*, "Mercury chalcogenide colloidal quantum dots for infrared photodetection: from synthesis to device applications," *Nanoscale*, vol. 15, no. 14, pp. 6476–6504, 2023, doi: 10.1039/D2NR07309A.

[271] S. B. Hafiz, M. R. Scimeca, P. Zhao, I. J. Paredes, A. Sahu, and D.-K. Ko, "Silver Selenide Colloidal Quantum Dots for Mid-Wavelength Infrared Photodetection," *ACS Appl. Nano Mater.*, vol. 2, no. 3, pp. 1631–1636, Mar. 2019, doi: 10.1021/acsanm.9b00069.

[272] X. Xue, H. Lv, Y. Qiu, Q. Hao, and M. Chen, "Thermally stable high carrier mobility nanocomposite infrared photodetector," *APL Photonics*, vol. 9, no. 4, p. 046101, Apr. 2024, doi: 10.1063/5.0194631.

[273] Y. Fu *et al.*, "Size-tunable and monodisperse lead sulfide quantum dots for broadband photodetectors," *APL Materials*, vol. 12, no. 3, p. 031126, Mar. 2024, doi: 10.1063/5.0190291.

[274] Q. Hao, H. Lv, H. Ma, X. Tang, and M. Chen, "Development of Self-Assembly Methods on Quantum Dots," *Materials*, vol. 16, no. 3, p. 1317, Feb. 2023, doi: 10.3390/ma16031317.

[275] J. Zhang, F. Huang, and Z. Lin, "Progress of nanocrystalline growth kinetics based on oriented attachment," *Nanoscale*, vol. 2, no. 1, pp. 18–34, 2010, doi: 10.1039/B9NR00047J.

[276] C. Fang, M. A. Van Huis, D. Vanmaekelbergh, and H. W. Zandbergen, "Energetics of Polar and Nonpolar Facets of PbSe Nanocrystals from Theory and Experiment," *ACS Nano*, vol. 4, no. 1, pp. 211–218, Jan. 2010, doi: 10.1021/nn9013406.

[277] E. Maraeva, A. Maximov, N. Permiakov, and V. Moshnikov, "Thermodynamic Analysis and Experimental Study on the Oxidation of PbX (X = S, Se) Nanostructured Layers," *Micromachines*, vol. 13, no. 8, p. 1209, July 2022, doi: 10.3390/mi13081209.

[278] W. Wu, B. Li, X. Xiang, and X. Zu, "Effect of Temperature on Visible Photoluminescence of Thermally Annealed PbSe Nanocrystalline Films," *J Appl Spectrosc*, vol. 90, no. 2, pp. 454–460, May 2023, doi: 10.1007/s10812-023-01553-3.

[279] G. Yang and B. Weng, "Reactive ion etching of PbSe thin films in CH4/H2/Ar plasma atmosphere," *Materials Science in Semiconductor Processing*, vol. 124, p. 105596, Mar. 2021, doi: 10.1016/j.mssp.2020.105596.

[280] M. R. Johnson, "Sweep-Out Effects in Hg1− *x* Cd *x* Te Photoconductors," *Journal of Applied Physics*, vol. 43, no. 7, pp. 3090–3093, July 1972, doi: 10.1063/1.1661664.

[281] Y. Dan, X. Zhao, K. Chen, and A. Mesli, "A Photoconductor Intrinsically Has No Gain," *ACS Photonics*, vol. 5, no. 10, pp. 4111–4116, Oct. 2018, doi: 10.1021/acsphotonics.8b00805.

[282] R. L. Petritz, "Theory of Photoconductivity in Semiconductor Films," *Phys. Rev.*, vol. 104, no. 6, pp. 1508–1516, Dec. 1956, doi: 10.1103/PhysRev.104.1508.

[283] J. N. Humphrey and R. L. Petritz, "Photoconductivity of Lead Selenide: Theory of the Mechanism of Sensitization," *Phys. Rev.*, vol. 105, no. 6, pp. 1736–1740, Mar. 1957, doi: 10.1103/PhysRev.105.1736.

[284] J. C. Slater, "Barrier Theory of the Photoconductivity of Lead Sulfide," *Phys. Rev.*, vol. 103, no. 6, pp. 1631–1644, Sept. 1956, doi: 10.1103/PhysRev.103.1631.

[285] J. Habinshuti *et al.*, "Phase transformation of PbSe/CdSe nanocrystals from core-shell to Janus structure studied by photoemission spectroscopy," *Phys. Rev. B*, vol. 87, no. 18, p. 184102, May 2013, doi: 10.1103/PhysRevB.87.184102.

[286] S. Yan *et al.*, "Effect of Air Atmosphere Sensitization on Formation of PbSe p–n Junctions for High-Performance Photodetectors," *Journal of Elec Materi*, vol. 49, no. 8, pp. 4929–4935, Aug. 2020, doi: 10.1007/s11664-020-08215-6.

[287] Opto Diode, "IR Detectors: BXP Series Uncooled PbSe Packages." Accessed: May 02, 2024. [Online]. Available: https://optodiode.com/ir-detectors-bxp-series.html

[288] Infrared Materials, "PbSe Detector Performance Summary." Accessed: May 02, 2024. [Online]. Available: https://infraredmaterials.com/pbse-detectors/pbse-detector-performance-summary/

[289] P. C. Findlay *et al.*, "Auger recombination dynamics of lead salts under picosecond free-electron-laser excitation," *Phys. Rev. B*, vol. 58, no. 19, pp. 12908–12915, Nov. 1998, doi: 10.1103/PhysRevB.58.12908.

[290] A. Rogalski, "Fundamental Performance Limitations of Infrared Detectors," in *Infrared Detectors*, 0 ed., CRC Press, 2010, p. 60. doi: 10.1201/b10319.

[291] C. J. Reyner, G. Ariyawansa, B. Claflin, J. M. Duran, and G. J. Grzybowski, "Approaches to low-cost infrared sensing," *Appl. Opt.*, vol. 60, no. 25, p. G162, Sept. 2021, doi: 10.1364/AO.427969.

[292] H. C. De Graaff and M. T. M. Huybers, "1/ *f* noise in polycrystalline silicon resistors," *Journal of Applied Physics*, vol. 54, no. 5, pp. 2504–2507, May 1983, doi: 10.1063/1.332369.

[293] M.-Y. Luo and G. Bosman, "An analytical model for 1/f noise in polycrystalline silicon thin films," *IEEE Trans. Electron Devices*, vol. 37, no. 3, pp. 768–774, Mar. 1990, doi: 10.1109/16.47784.

[294] S.-L. Jang, "A model of noise in polysilicon resistors," *Solid-State Electronics*, vol. 33, no. 9, pp. 1155–1162, Sept. 1990, doi: 10.1016/0038-1101(90)90094-U.

[295] A. J. Madenach and J. H. Werner, "Noise spectroscopy of silicon grain boundaries," *Phys. Rev. B*, vol. 38, no. 18, pp. 13150–13162, Dec. 1988, doi: 10.1103/PhysRevB.38.13150.

[296] A. De Iacovo, C. Venettacci, L. Colace, L. Scopa, and S. Foglia, "Noise performance of PbS colloidal quantum dot photodetectors," *Applied Physics Letters*, vol. 111, no. 21, p. 211104, Nov. 2017, doi: 10.1063/1.5005805.

[297] C. T. Lin, Y. K. Su, S. J. Chang, H. T. Huang, S. M. Chang, and T. P. Sun, "Effects of passivation and extraction surface trap density on the 1/f noise of HgCdTe photoconductive detector," *IEEE Photon. Technol. Lett.*, vol. 9, no. 2, pp. 232–234, Feb. 1997, doi: 10.1109/68.553102.

[298] F. N. Hooge, "The relation between 1/*f* noise and number of electrons," *Physica B: Condensed Matter*, vol. 162, no. 3, pp. 344–352, July 1990, doi: 10.1016/0921-4526(90)90030-X.

[299] P. Dutta and P. M. Horn, "Low-frequency fluctuations in solids: 1 f noise," *Rev. Mod. Phys.*, vol. 53, no. 3, pp. 497–516, July 1981, doi: 10.1103/RevModPhys.53.497.

[300] U. N. Nandi, C. D. Mukherjee, and K. K. Bardhan, "1/ *f* noise in nonlinear inhomogeneous systems," *Phys. Rev. B*, vol. 54, no. 18, pp. 12903–12914, Nov. 1996, doi: 10.1103/PhysRevB.54.12903.